PhD thesis

Exploring superradiance for enhanced sensors

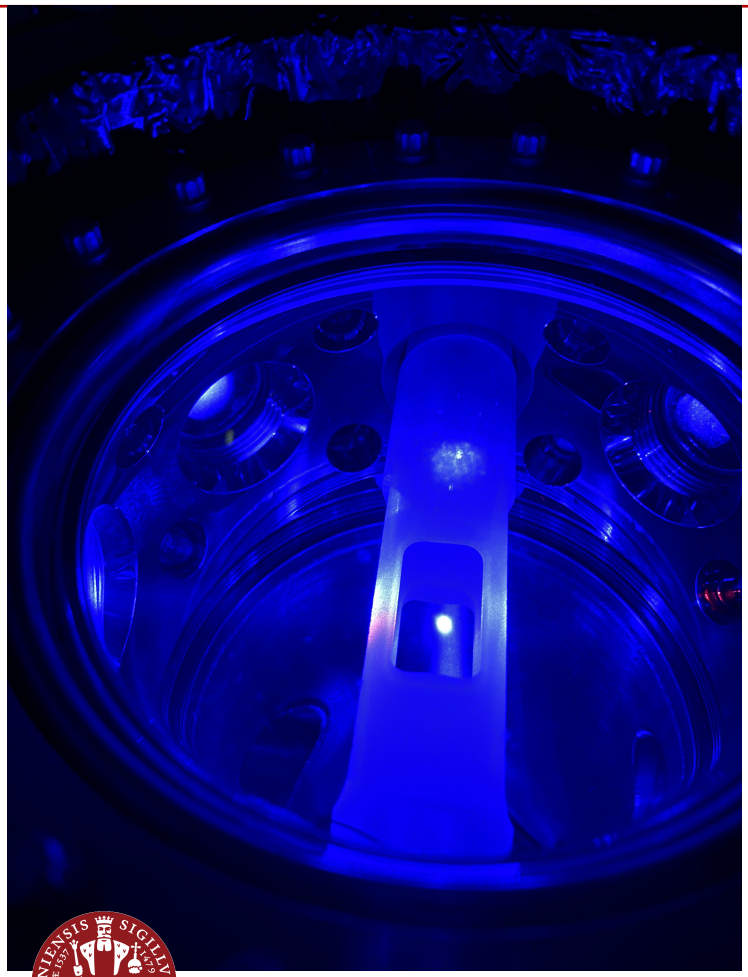

UNIVERSITY OF COPENHAGEN

Eliot Bohr

Exploring superradiance for enhanced sensors

Group of Quantum Metrology
The Niels Bohr Institute

This thesis has been submitted to the PhD School of
The Faculty of Science, University of Copenhagen
September 15th 2023

Author Eliot Bohr
Academic supervisor Prof. Jörg Helge Müller

Abstract

In this thesis, we describe experimental upgrades to the apparatus to investigate superradiance on the kHz intercombination line in ultracold 88-strontium. We present two experimental results which leverage collective effects of atoms within a cavity, applying tools of cavity quantum electrodynamics for advancing atomic clock technology.

In our first investigation, we employ superradiant pulses from the cavity mode as a fast and directed atomic population readout. This approach relies on an excitation threshold for superradiant emission, which occurs for a transversely driven atomic ensemble. We experimentally verify this threshold and map out a unique Ramsey spectroscopic lineshape. This lineshape is characterized by its near-zero photon zones where the pump laser detuning results in an excitation below the established threshold. Our technique induces significantly less heating compared to more common fluorescent state readouts. We demonstrate the potential for multiple Ramsey sequences within a single experimental cycle.

In our second investigation, we analyze the frequency spectrum of superradiant emission by extending the pulses using an incoherent repumping scheme. By tuning a repump laser's frequency, we control and sustain steady state lasing for over a millisecond. This allows us to observe a linewidth of the emitted light that is nearly an order of magnitude narrower than the transition linewidth. Our system operates in what is known as the "bad cavity" regime, where the phase coherence in the laser is predominantly stored in the atoms rather than in the intracavity light field. Therefore, the emitted light is not only narrow in frequency, but also exhibits reduced sensitivity to cavity mirror vibrations- a prevailing challenge in contemporary atomic clocks.

Resumé

I denne afhandling beskriver vi af apparatur til at undersúge superradiens på kHz-interkombinationslinjen i ultra kolde strontium 88 atomer. Vi præsenterer to eksperimentelle resultater, der udnytter kollektive effekter af atomer i en optisk kavitet, ved at anvende værktøjer fra kavitet kvanteelektrodynamik til at fremme atomurteknologi.

I den første undersøgelse anvender fotoner udsendt i en superradient puls fra kavitetstilstanden som en hurtig og præcis atompopulationsaflæsning. Denne tilgang er afhængig af en excitationstærskel for superradiant emission, som forekommer for et atomensemble drevet af en tværgående excitationspuls. Vi verificerer denne tærskelværdi eksperimentelt og kortlægger en unik Ramsey spektroskopisk. Disse interferensfrynser er kendetegnet ved zoner hvor signalet er nul, hvor pumpens frekvensafvigelse fra atomar resonans resulterer i en excitation under den etablerede tærskel. Denne sekvens inducerer væsentligt mindre opvarmning sammenlignet med mere almindelige fluorescerende tilstandsudlæsninger. Vi demonstrerer vores tekniks potentiale for gentagne Ramsey-sekvenser inden for en enkelt eksperimentel cyklus.

I vores anden undersøgelse analyserer vi frekvensspektret af superradient emission ved at forlænge pulserne ved hjælp af repumping. Ved at tune, kontrollerer og opretholder vi steady state-lasing i over et millisekund. Dette giver os mulighed for at observere en linjebredde af det udsendte lys, der er næsten en størrelsesorden smallere end overgangslinjebredden. Vores system opererer i "drig kavitet" regimet, hvor fasekohærensen i laseren overvejende er lagret i atomerne frem for feltet i kaviteten. Derfor er det udsendte lys ikke kun snævert i frekvens, men udviser reduceret følsomhed over for vibrationer i kavitetspejlene - en udfordring i nutidige atomure.

List of publications

Authors marked with * contributed equally.

Peer-reviewed:

Sofus Laguna Kristensen*, Eliot Bohr*, Julian Robinson-Tait, Tanya Zelevinsky, Jan W. Thomsen, and Jörg Helge Müller:
Subnatural Linewidth Superradiant Lasing with Cold ^{88}Sr Atoms
Physical Review Letters 130, 223402 – Published 31 May 2023

Under consideration:

Eliot Bohr*, Sofus L. Kristensen*, Christoph Hotter, Stefan Alaric Schäffer, Julian Robinson-Tait, Jan W. Thomsen, Tanya Zelevinsky, Helmut Ritsch, Jörg Helge Müller:
Collectively enhanced Ramsey readout by cavity sub- to superradiant transition
Manuscript submitted. Preprint available here: arXiv:2306.12544.

Conference contributions:

Eliot Bohr, Sofus Laguna Kristensen, Julian Robinson-Tait, Jörg Helge Müller
Exploring Cavity Superradiant-Enhanced Sensors
Danish Optical Society (DOPS) National Optics Congress 2022
(contributed talk)

Eliot Bohr, Sofus Laguna Kristensen, Stefan Alaric Schäffer, Julian Robinson-Tait, Jörg Helge Müller
Optical Ramsey Spectroscopy with Superradiance Enhanced Readout
2023 Joint Conference of the European Frequency and Time Forum and IEEE International Frequency Control Symposium (EFTF/IFCS)
(contributed talk and published conference proceeding eCF Paper Id: IFCS2023.7196)

Eliot Bohr, Sofus Laguna Kristensen, Julian Robinson-Tait, Jörg Helge Müller
Quasi-continuous superradiance on the 7.5 kHz clock transition of ^{88}Sr
The Division of Atomic, Molecular and Optical Physics (DAMOP)
(contributed poster)

Eliot Bohr, Sofus Laguna Kristensen, Julian Robinson-Tait, Jörg Helge Müller
Quasi-continuous superradiance on the 7.5 kHz clock transition of ^{88}Sr
International Conference on Atomic Physics (ICAP)
(contributed poster)

Eliot Bohr, Sofus Laguna Kristensen, Stefan Alaric Schäffer, Julian Robinson-Tait, Jörg Helge Müller
Exploring superradiance for enhanced sensors
Quantum enhanced sensing symposium (QESR)
(contributed poster)

Eliot Bohr, Sofus Laguna Kristensen, Stefan Alaric Schäffer, Julian Robinson-Tait, Jörg Helge Müller
Optical Ramsey Spectroscopy with Superradiance Enhanced Readout
The International Conference on Laser Spectroscopy (ICOLS)
(contributed poster)

Acknowledgements

I would like to start by thanking **Jörg Helge Müller**, who took on the reins as group leader just a few months into my time at the institute. Jörg's expertise in experimental and atomic physics has been inspiring. Our frequent discussions, particularly during our pursuit of the red MOT, were pivotal in steering my work. I distinctly recall a week when morale was particularly low; his words, "keep calm, and carry on," were precisely what we needed to hear, and epitomized the perseverance required in experimental physics. My gratitude extends to our many insightful coffee conversations.

I would also like to thank **Jan Thomsen** for believing in me and welcoming me into the team. Your infectious enthusiasm has been something I deeply admired and sought to emulate. As the Head of Department, the time you dedicated to our update meetings, despite your pressing responsibilities, was invaluable. These sessions not only catalyzed the progress of my PhD but also played a helpful role in refining my presentations for various conferences.

Our lab greatly benefited from the expertise of **Tanya Zelevinsky**, who joined us for an impactful half-year during a critical phase of our research. Her knack for posing the right questions during her afternoon visits proved instrumental, helping us achieve the results in this thesis. I wish to thank her for her time with us, and look forward to our continued collaboration and discussions.

Stefan Alaric Schäffer and **Martin Romme Henriksen** were the postdocs who played a key role in my integration into the lab and group. Martin's assistance, especially during the initial stages when we locked the reference laser, laid a foundation that served me well throughout my doctoral journey. Stefan, our discussions on physics have always been enlightening. Even after your move to Amsterdam, your collaboration on superradiance remained vital, and I'm grateful for the sustained connection we shared.

Asbjørn Arvad Jørgensen and **Mikkel Tang** were the established PhD students when I started. Their exceptional acumen in coding constantly left me in awe, and though I strived, their skillset remained unsurpassed. The learning I've gleaned from both of you is monumental. Thank you for the unwavering collaboration, assistance, and the camaraderie shared during our collective endeavors.

A big thanks to **Sofus Laguna Kristensen** and **Julian Robinson-Tait** who started their PhD journeys around the same time as I did. Through the highs and lows, the stressful moments and the triumphs, having you both close by made all the difference. Julian, your unwavering calm and patience have always stood out, and your exemplary leadership of the Sr2 team has never ceased to impress

me. Sofus, our close collaboration and countless hours spent together in the lab have been a joy. Whenever I find myself with four repump lasers, I will follow our tradition and name them Alice, Bob, Charlie, and Daisy. Your innovative ideas continually invigorated our projects, and our synergy over the past three years resulted in some really interesting signals in the lab.

Christoph Hotter and **Helmut Ritsch** became our close friends and theory collaborators over the past year. The discussions have always been incredibly enlightening and I am continually amazed at how much you could teach us about our own experiments.

I am also thankful for the companionship of all of my lab mates I have had the privilege of spending hours in the lab with, including Valentin, Maddalena, Jonathan, Andrea, and most recently Neven.

During the first year of my PhD, I had the pleasure of undertaking my secondment at the Danish National Metrology Institute (DFM). I extend my gratitude to my advisor, **David Barslev-Harder**, and my daily supervisors **Jürgen Appel** and **Lars Wacker**. Both are exceptional experimentalists, and one of them always seemed to have time for answering my questions and I really appreciated it.

A special thanks to my dear friends and fellow ESRs within the MoSaiQC European Innovative Training Network. Our meetings at various conferences and consortia throughout my PhD have not only been a joy but also contributed greatly to my growth in physics. I wish you all the best and hope our paths cross again in the world of atomic clocks and laser physics.

Lastly, I could not have done it without the support of my wonderful parents. Moving countries the same month that COVID struck was not easy. I have thoroughly appreciated our near daily conversations that kept me anchored. Additionally, a heartfelt thank you to my uncle Tomas, whose insights have enriched my journey in physics over these past three years.

Contents

CHAPTER 1

Introduction to stable lasers and atomic clocks

1.1 Stable lasers

The ability to generate extremely coherent, narrow-linewidth light, such as in a laser, has been at the forefront of advances in contemporary science and technology. A simple laser consists of an optical gain medium located inside a resonant optical cavity. The frequency of the laser is derived from the cavity resonance frequency where the laser gain is high. Linewidths of the most common type of laser in our field, external cavity diode lasers (ECDL), are in the range of approximately 10 kHz to 1 MHz. The output frequency of the laser is susceptible to a variety of noise processes stemming from the gain medium, optical path length changes in the cavity, other intracavity elements, and amplified spontaneous emission. Such noise processes limit the temporal coherence of the laser, typically well below the needed coherence time required for high-resolution spectroscopy of narrow transitions in atoms. In practice, a much more well-defined resonant frequency can be realized by stabilizing the laser to a carefully designed passive optical cavity, typically a simple two-mirror Fabry-Pérot interferometer. These provide very stable resonances and can be used to obtain feedback signals allowing lasers to reach sub-Hz stabilities [1–5].

Enabling the next generation of ultra-stable, narrow-linewidth lasers would impact many fields of science including communication, navigation [6, 7], geodesy [8–10], and searches for variations of fundamental constants [11–14]. In the field of atomic, molecular, and optical (AMO) physics, such lasers are used to cool, control, and manipulate atoms with unprecedented precision. Narrow-linewidth lasers are essential in the operation of optical atomic clocks and in this thesis we will focus on their application in frequency references and metrology.

1.2 Atomic clocks

For millennia, mankind has relied on the precise measurement of time, from tracking celestial bodies to coordinating agricultural endeavors and societal gatherings. Today, the significance of precisely defined and agreed-upon units remains crucial in linking human activities. Among all of the fundamental units, time is the most precisely defined. Consequently, many other units are delineated as combinations of the definition of the second and other fundamental constants of nature. For example, the definition of the meter is how far light travels in vacuum in a certain fraction of a second. This combines a measurement of time with a fundamental constant, c.

A clock's foundational principle is straightforward: harness a periodic phenomenon and monitor it. Historically, timekeeping was anchored to the positions of celestial bodies, later transitioning to mechanical pendulums. In modern times, the oscillators used for precise timekeeping have passed to electro-mechanical resonances in quartz crystals and, more recently, to lasers stabilized to narrow atomic transitions. We observe a trend in improving a clock's stability: for the same frequency uncertainty, having a higher frequency oscillator helps.

A clock operates by counting ticks, or periods, in a given time interval. The more zero-crossings or ticks, the more precisely one can measure the time interval. This advantage is analogous to having a measurement ruler with finer and finer intervals, allowing for a more precise length measurement. The ratio of the oscillation frequency f_0 to its uncertainty Δf is called the quality factor $Q \equiv f_0/\Delta f$, and is included in the equation for the stability of a clock, Eq. 1.3.

Basing a measurement of time on an atomic transition offers a universal appeal to clocks. Unlike man-made objects, which are prone to aging of the materials and manufacturing inconsistencies, all atoms of a particular isotope are identical in structure, governed only by the laws of physics of that particular atom. They neither age nor deviate in their electronic transitions, unless influenced by external perturbations like electric or magnetic fields. Thus, if a clock is based on an unperturbed atomic transition, it will be a universal clock.

In a traditional, or "passive", atomic clock, the oscillation of an electromagnetic wave from a laser serves as the pendulum. This laser, over short time scales, is finely tuned such that an integer number of half wavelengths fits the length of a high-finesse reference cavity. But these cavities, being man-made, are subject to drift. For long-term stability, we tune the oscillator to a narrow transition in a cloud of cold atoms, or single ions, as depicted in Fig. 1.1.

Clock operation relies on the principle of achieving maximal population transfer when the laser is on resonance. The rate at which the atoms move from ground to excited state depends on the coupling strength, or "Rabi frequency", between the laser and the atom. The laser with robust short-term stability from locking to the reference cavity, "interrogates", or attempts to excite a transition in the atomic ensemble. After this attempt, a detection of the atomic state population is made to determine how successful the excitation was. This information is used to correct the laser such that its frequency is maintained on the atomic resonance.

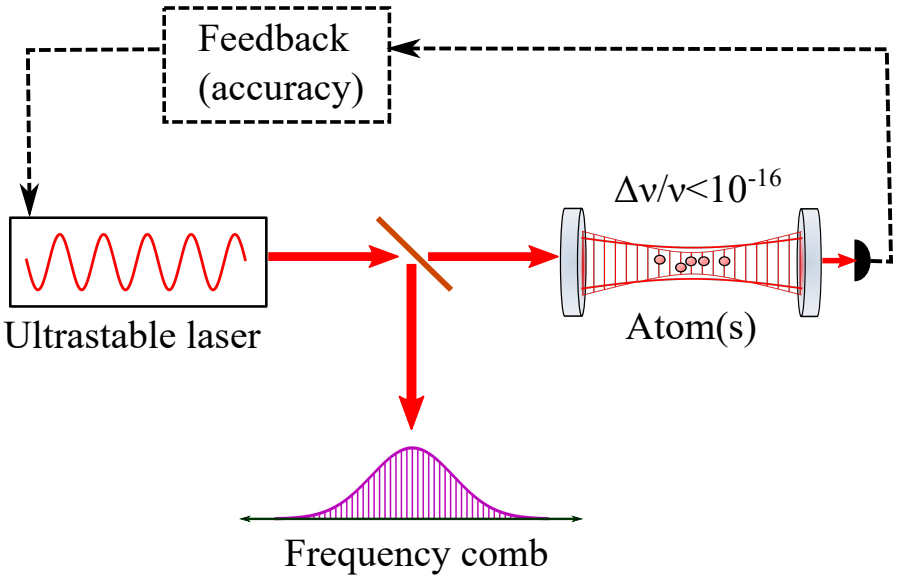

Figure 1.1: Passive atomic clock scheme. A laser's frequency is stabilized on a short time scale to an ultrastable reference cavity. This light is periodically stabilized to a narrow transition in atoms or ions (here we depict neutral atoms in a lattice) via feedback to the laser. The oscillation frequency in optical atomic clocks is much too high to count using electronics, so it is downconverted using a frequency comb.

The physical basis of this atomic timekeeping is Plank's famous equation relating frequency and energy,

$$\Delta E = h\nu, \tag{1.1}$$

where ΔE is the energy difference between the ground and excited energy levels in the clock transition, h is Planck's constant, and ν is the frequency of the photon.

If we provide the precise frequency of light corresponding to the energy difference of the two atomic levels, the atoms can be maximally excited. Because the transition frequencies of the best clocks are usually in the few 100s of THz range, their oscillations must be downconverted in order for them to be measured using electronics. This is done by using a frequency comb [15, 16], which provides equidistant narrow lines across a broad spectrum.

1.3 Fractional frequency instability

There are two primary metrics for evaluating atomic clocks - accuracy and stability. The accuracy of an atomic clock is a measure of how well the measured frequency matches the unperturbed atomic transition frequency. The energy levels of the clock transition are not fully immune to systematic effects from the environment. This requires a careful calibration and understanding of all potential shifts of the frequency, with uncertainties, in order to reliably compare the clock with another one.

The figure of merit to characterize the performance of a clock, or frequency standard, is the stability. The stability is the precision the system accrues as a function of averaging time τ and is given by,

$$\sigma_y(\tau) = \frac{\chi}{2\pi Q(SNR)}\sqrt{\frac{t_c}{\tau}}. \tag{1.2}$$

Here, Q is the quality factor as we have previously defined, SNR is the signal-to-noise-ratio achieved in the measurement cycle time, t_c, and χ is a constant of order unity that accounts for the details of the spectroscopic lineshape. For quantum projection noise (QPN) limited measurements, the SNR is limited by the number of atoms, as $1/\sqrt{N}$. As seen in the above equation, feasible ways to decrease the final clock instability are averaging for longer times τ, or increasing the SNR.

The way we measure frequency instability in the lab is to use a tool called the Allan deviation [17]. Unlike the standard deviation which diverges for certain noise spectra, the Allan deviation can be used to identify a wider range of underlying noise sources [18]. For a continuous measurement, the two-sample Allan deviation is defined by,

$$\sigma_y(\tau) = \sqrt{\frac{(\bar{y}_{i+1} - \bar{y}_i)^2}{2}} \tag{1.3}$$

Here, y is the fractional frequency ν/ν_0, with bars indicating averages over time interval τ, at the ith interval. We will use the metric of the Allan deviation when looking at the stability of our reference laser. It is crucial to distinguish between linewidth, which characterizes the spectral width of emitted light, and frequency instability, which quantifies the precision with which one can pinpoint the peak frequency.

After interrogating the atoms one must detect to what degree the atoms have been excited. This is typically done by applying a different laser on a spectrally broad transition that shares the lower state with the clock transition, a technique known as electron shelving [19]. The fluorescence from the rapid scattering events is detected and this signal can be used to provide feedback on the clock laser's frequency. The large number of photons scattered per atom yields a high SNR, causing the photon shot noise to become negligible compared to the atomic projection noise. This is a destructive measurement for the atomic ensemble because the scattering heats up the atoms beyond recapture, requiring a completely new atomic ensemble for subsequent interrogations.

Such a destructive measurement leads to stroboscopic sampling of atoms, which leads to the unwanted aliasing of high-frequency laser noise into the time domain of the experiment. This effect first pointed out by Dick [20], arises due to the introduction of a dead-time during atomic ensemble preparation. Within an experimental cycle, a dead time degrades long-term stability due to the downconversion of frequency noise on the reference laser (interrogation laser) at harmonics of the inverse of the cycle time, $1/\tau_c$. This can prevent a clock from achieving stabilities one might otherwise expect from the fundamentals of the system. Several factors influence this degradation: the fractional dead time, the interrogation method, and the clock laser noise. The Dick effect will put a limit on the flicker floor instability

of an oscillator. It is a limiting noise source in some of the best atomic clocks, particularly in neutral atom optical lattice clocks, which have not yet reached the QPN limit due to this effect.

Mitigating the Dick effect, although technically challenging, can be approached in a few ways. One could employ synchronous interrogation between two atomic samples using the same laser [21–23], or lock a laser to two atomic ensembles in an interleaved manner, ensuring a dead-time free interrogation [24, 25].

To summarize, an optimal atomic clock should have many atoms, a long coherence time, and a high duty cycle (measurement time divided by total cycle time). Among the leading platforms are trapped ions, known for their great control and high duty cycle. However, compared to neutral atom clocks, they typically have just one ion, and so these clocks are limited by QPN [26]. On the other hand, neutral atom optical lattice clocks have a high atom number, and therefore very low QPN. However these clocks, in addition to the Dick effect, are prone to shifts stemming from interactions between the atoms, and tunneling between the lattice sites.

Optical atomic clocks have achieved astonishing fractional instabilities which are now reaching down to a few parts in 10^{19} [27–32]. Due to their high precision and accuracy, optical clocks are the ideal sensors for measuring spatio-temporal variations in the laws of physics and the time invariance of the fundamental constants of nature [26].

In addition to the pursuit for the absolute best precision, there has been a lot of interest in clocks for various purposes. Each clock design prioritizes different aspects such as averaging-down time, deployability, cost, weight, size, and susceptibility to particular noises. The choice of the clock hinges upon the specific requirements of a given time measurement scenario.

A notable application of ultraprecise clocks lies in geodesy since the frequency of a clock depends on the gravitational field [33]. Their inherent sensitivity to the gravitational redshift allows them to be an extremely sensitive probe to variances in the Earth's gravitational potential. Currently, the best clocks in labs can discern gravitational redshifts with a precision on the scale of millimeters within an atomic sample at the Earth's surface [34]. Producing more deployable, high-precision clocks with fast averaging down times, could revolutionize fields like seismology, offering unprecedented tools for predicting earthquakes [35] and volcanic eruptions [36].

1.4 Atomic interrogation techniques

The spectroscopic signal achieved when shining a narrow-linewidth laser across an atomic resonance provides a sharp feature to which the laser's frequency can be stabilized. To keep the atomic resonance as narrow and as stable as possible, the atoms must be cooled and trapped to remove Doppler broadening, and shielded from any auxiliary fields that might induce a frequency shift in the reference transition.

Applying a laser beam at the frequency nearly matched to the ΔE of the

transition induces a coupling between the ground and excited states. This coupling rate is termed the generalized Rabi frequency and is related to the detuning and intensity of the laser. On resonance, the Rabi frequency Ω causes the population to oscillate between the two levels over time as $\sin^2\left(\frac{\Omega t}{2}\right)$ [37]. Thus, an on-resonance laser beam can bring the atoms to the excited state through two primary spectroscopic methods:

1. **Rabi spectroscopy:** Using a single excitation pulse with duration of $t = \frac{\pi}{\Omega}$, called a π pulse.

2. **Ramsey spectroscopy:** Utilizing two separate pulses with durations of $t = \frac{\pi}{2\Omega}$, known as $\pi/2$-pulses, separated with a dark evolution time. In this technique, cited from Ramsey's work [38], the first $\pi/2$-pulse transitions the atom into a coherent superposition of the ground and excited states. This superposition, which is maximally sensitive to atom-laser detuning, is then left to evolve freely. The subsequent $\pi/2$-pulse then projects any accumulated phase difference onto the atomic state population, which can be read out via a fluorescence measurement. Figure 1.2 illustrates the distinctions in excitation methods and their respective lineshapes.

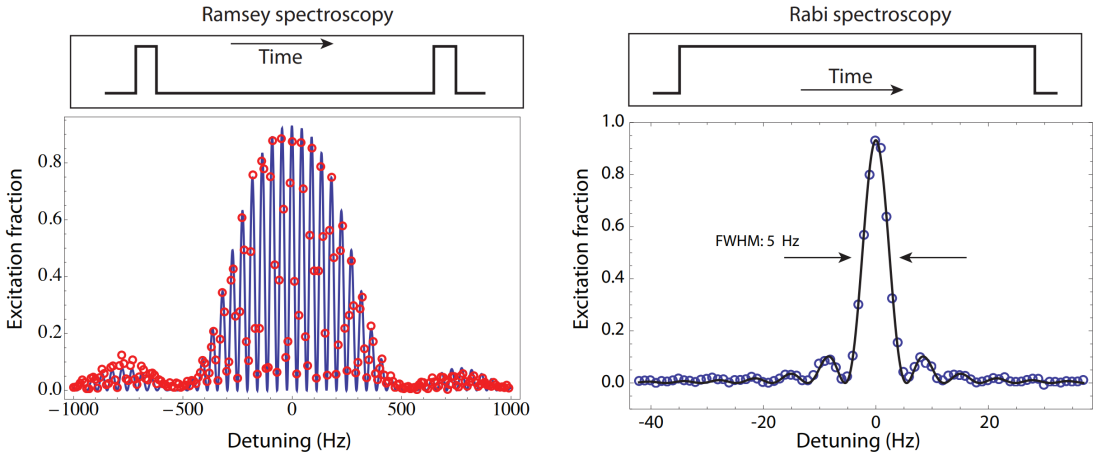

Figure 1.2: Sprectroscopic lineshapes obtained from Ramsey and Rabi spectroscopy in a ^{87}Sr lattice clock with laser excitation schemes illustrated above the lineshapes. Rabi spectroscopy (right) results in a single fringe upon scanning the laser across resonance, while Ramsey spectrsocopy results in a fringe pattern, where the narrowness of the fringes is inversely related to the free evolution time between the excitation pulses. Figure from [39].

While Rabi spectroscopy is simpler and operates at reduced light intensity, Ramsey spectroscopy optimizes the atom's sensitivity to detuning over equivalent interrogation times, resulting in narrower fringes upon measuring the resulting excited state population. Each method has its advantages, and ultimately, for a given system, one should try out both schemes to determine which provides the better clock performance.

Typically the atomic interrogation is conducted at a frequency which is halfway up a fringe where the excitation fraction versus laser detuning has the steepest slope. A steeper slope means that the excitation fraction, and feedback signal, is more sensitive to laser detuning. In a real-time clock feedback scheme, the clock laser frequency may be stepped from side to side about a fringe, and by taking the difference between subsequent measurements, a feedback signal is calculated. Gain in a feedback servo is optimized so that the feedback signal is minimized, and the laser frequency is continuously steered to resonance. More discussions on various detection schemes can be found in [26].

1.5 Superradiance for atomic clocks and stable lasers

Collective effects are manifest across diverse scientific disciplines. Such effects occur when the collective behavior of a group deviates from the mere summation of individual behaviors. These interactions lead to emergent phenomena or properties on a larger scale. Our research delves into such collective atomic states, which result in atoms emitting light both phase synchronously and at an enhanced rate. This phenomenon, known as superradiance, can be harnessed to create highly stable lasers.

As discussed previously, on a short time scale a stabilized laser frequency is kept by the flywheel of the reference cavity. One of the current limitations in the most precise lasers arises from thermal Brownian motion of particles within the mirror coatings. This motion changes the length of the cavity, and therefore its resonances, causing the frequency of the laser to drift.

One approach to overcome this limitation is to build a laser that operates in the so-called "bad cavity", or superradiant regime. Traditional lasers use a spectrally broad gain medium, and a narrow-linewidth cavity which acts as the frequency discriminator for the outgoing light. A superradiant laser flips these roles. Such a laser features a broad cavity and a narrow-spectrum gain medium, such as a cloud of laser-cooled atoms with a narrow transition, to carve out the resulting light spectrum. In this scheme, the atoms would act as the flywheel, or phase memory for the laser, rather than the light field of the cavity mode.

Since superradiance was theoretically proposed back in the 1950s, it was often viewed as a troublesome experimental feature, leading to faster decay in scenarios where atoms and molecules were spaced closely. However, under the right conditions this effect can become advantageous and provide directional emission with a linewidth dictated by an atomic transition. Furthermore, the increased emission rate makes the light more useful in certain technological applications. It is predicted that superradiant lasers which operate on very narrow optical transitions could surpass the spectral purity of existing lasers by magnitudes if continuously operated [40–42]. However, due to experimental challenges associated with realizing sufficiently high atom numbers at low enough temperatures, there are no fully continuous superradiant lasers on narrow optical transitions to date. There is an ongoing effort in the quantum metrology community to make one.

Clocks operating on light which is directly generated from the atomic cloud are termed "active" clocks, whereas clocks that operate on the laser light which is stabilized to an atomic signal are considered "passive". Superradiant lasers are a promising type of active frequency reference, which operate similarly to the active maser [43], but at optical frequencies. The active reference may prove valuable for the operation of high-precision optical frequency references outside of laboratory environments, especially in mobile applications. In scenarios where external factors, like vibrations and temperature fluctuations, cause significant perturbations in the local oscillator laser's frequency, the high bandwidth and reduced sensitivity to cavity noise could offer considerable advantages over traditional passive atomic frequency references.

1.6 Outline of thesis

The remainder of this thesis is organized as follows. In chapter 2, I will discuss the properties of strontium atoms, single-mode cavities, and introduce the physics that offers insights into the coupling between atoms and cavities. The latter part of the chapter emphasizes the collective effect of superradiance and how it emerges in an atom-cavity system.

In chapter 3, I describe the experimental setup, focusing on the aspects which I have substantially worked on, such as stabilizing the reference laser which we use to interrogate the atoms.

Chapter 4 focuses on our first experimental steps including achieving the collective strong coupling regime and producing superradiant pulses on an ultracold atomic cloud.

Chapter 5 describes novel work in collaboration with our Innsbruck collaborators, Christoph Hotter and Helmut Ritsch, on investigating a threshold excitation angle for cavity superradiance with transverse excitation. We leverage this threshold and demonstrate a fundamentally new collectively enhanced Ramsey lineshape.

In chapter 6, we extend the superradiant pulses by incoherently repumping the atomic ensemble to the upper lasing level, allowing us to investigate the frequency spectrum of the superradiant emission for durations not limited by the natural lifetime of the excited state. We demonstrate lasing output with a linewidth nearly an order of magnitude below the natural linewidth of the transition which the light is emitted from.

Chapter 7 discusses a very different experiment, which I worked on during a six-month secondment at the Institute of Danish Fundamental Metrology (DFM). Here I detail the process of setting up iodine in a hollow-core fiber and obtaining a spectroscopic signal intended for potential laser stabilization. The final measurements were postponed due to unforeseen delays in the production of locking electronics, a ripple effect of the COVID pandemic and the ensuing global chip shortage. I have plans to return to take final Allan deviation measurements and investigate the stability of the laser locking shortly after the submission of this thesis.

CHAPTER 2

Atom-cavity platform and superradiance

In atomic, molecular, and optical (AMO) experiments, the choice of an atomic species is influenced by many factors and considerations. These include the accessibility of the atomic species, the potential to efficiently cool the atoms, whether the atom's transitions align with the wavelengths of commercially available diodes, and the intrinsic atomic structure which might offer interesting possibilities for research. Strontium, for instance, has become increasingly popular in many studies in part due to its broad cooling transition and narrow clock transition at commercially available diode wavelengths.

A cavity consists of two highly reflective mirrors that allow light to bounce back and forth many times before escaping through the mirrors. Therefore, placing atoms inside the cavity amplifies the interactions between atoms and photons. This field of study, known as cavity quantum electrodynamics (cavity QED), offers a powerful platform to study the fundamental interplay between atoms and photons under very controlled settings.

2.1 Strontium transitions

Strontium is element 38, and appears as a soft silver/white/yellowish metal. There are four naturally occurring stable isotopes: one fermionic ^{87}Sr, and three bosonic variants ^{84}Sr, ^{86}Sr, ^{88}Sr. ^{88}Sr is the most abundant making up 82.58% of all natural strontium [44], making it easiest to achieve high atom numbers in an experiment. However, its low scattering length renders it less attractive for studies where atom-atom interactions are vital, such as in the production of Bose-Einstein condensates [45].

Being an alkaline-earth element, strontium possesses two valence electrons. These electrons can align their spins either in a singlet (anti-parallel electron spins) or a triplet (parallel electron spins) configuration. Although transitions between these singlet and triplet states are usually prohibited by selection rules in the dipole approximation, various factors such as spin-orbit and electron nuclear spin coupling

effects give rise to a small decay linewidth.

Alkaline-earth atoms have even number of protons. Moreover, the bosonic isotopes, possessing even numbers of neutrons, arrange their nucleonic spins in a singlet configuration. This results in all alkaline-earth bosons having a nuclear spin of $I = 0$. Contrarily, ^{87}Sr has a nuclear spin $I = 9/2$. The nuclear spin couples $^3P_0$ to $^3P_1$, causing the $^3P_0 \rightarrow ^1S_0$ transition to become weakly allowed with a linewidth of 1.35 mHz [46]. This is the transition which the leading strontium clocks operate on. The lower abundance and large nuclear spin of ^{87}Sr leading to 10 Zeeman sublevels, makes this isotope generally more technically challenging to work with. In ^{88}Sr, it is possible to open this $^3P_0 \rightarrow ^1S_0$ transition by applying a very strong magnetic field [47].

For cooling strontium down to ultracold temperatures, we use several cooling stages including a Zeeman-slowing technique, and two different magneto-optical trap (MOT) stages.

In the first cooling stages, including the Zeeman slowing and blue MOT, we take advantage of the $2\pi \times 30.5$ MHz wide $^1S_0 \rightarrow {}^1P_1$ transition which occurs at 461 nm, as illustrated in Fig. 2.1. The large linewidth allows for a high scattering rate. The Doppler temperature is 0.7 mK, and in the lab cooling on this transition typically results in the atoms reaching as low as a few mK. This transition is not fully closed, and has a loss channel from $^1P_1$ with a branching ratio of about $1 : 20000$ [48], to $^1D_2$. The $^1D_2$ state has a lifetime of approximately 350 μs [49] before decaying into $^3P_2$ or $^3P_1$ with a ratio of 2:1. An atom in $^3P_1$ returns to the system in 21 μs, but the $^3P_2$ state will not decay for about 500 s [50]. Therefore an atom which reaches this state will no longer be cooled, so repumping lasers are required. To repump atoms out of $^3P_2$, we use a 707 nm laser beam which excites atoms to $^3S_1$, from which they decay to $^3P_{0,1,2}$ in the ratio 1:3:5. For this reason, this repumping scheme always requires two lasers, at 679 nm and 707 nm. If the atoms are already cooled, the $^3P_2$ state is magnetically trappable and can be used to store laser-cooled atoms.

The second stage cooling is done on the rather narrow-linewidth transtion at 689 nm with linewidth $2\pi \times 7.5$ kHz. This transition has a Doppler limit of 0.2 μK, while still being sufficiently strong to counteract gravity. After this stage, temperatures ranging from 1 to 10 μK are typically reported.

For our lab, opting to base our research on the "kHz transition" was in order to avoid the demanding technical challenges associated with working on the mHz transition. It is also simpler and due to the shorter natural lifetime, results in signals with higher powers which are easier to detect. This decision enables us to focus on the proof of principle experiments of this thesis. In the future, leveraging the precision of the mHz transition will be essential to compete with the state-of-the-art systems.

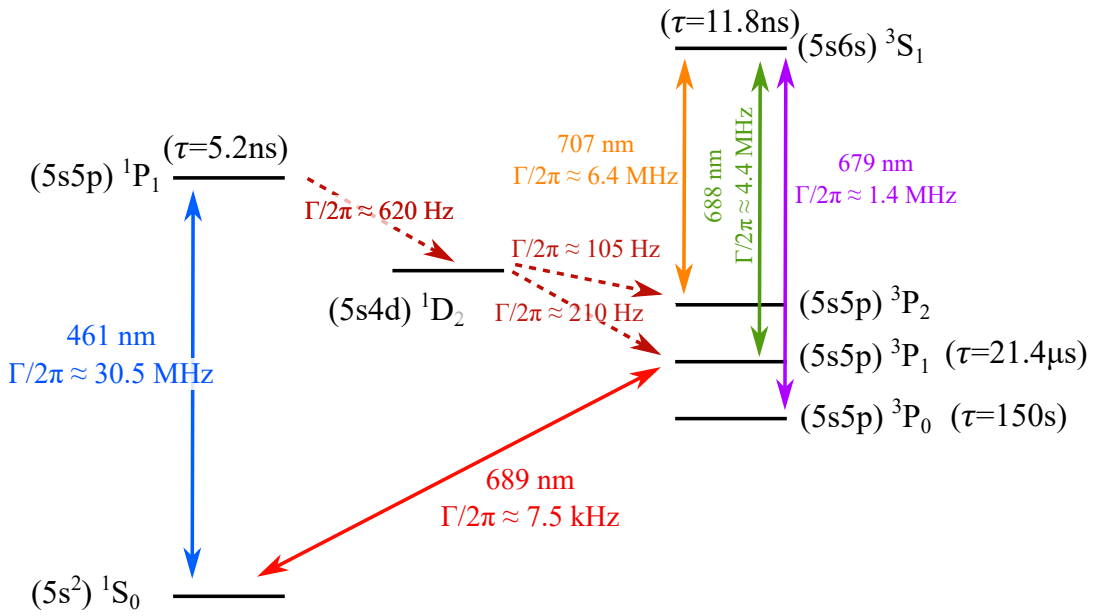

Figure 2.1: Strontium energy levels relevant for this thesis, with wavelength, decay rate, and excited state lifetimes. Cooling on the $^1S_0 \rightarrow ^1P_1$ can achieve temperatures of a few mK. However, this has a slow leak, so we apply two repump lasers at 679 nm and 707 nm. The second stage MOT operating on the $^1S_0 \rightarrow ^3P_1$ transition is capable of reaching μK temperatures. In the repumping scheme utilized in chapter 6, we repump the $m = \pm 1$ sublevels of $^3P_1$ using a 688 nm laser. Lifetimes to atomic transitions have primarily been sourced from [51, 52].

2.2 Superradiance

When considering $N \gg 1$ atoms individually excited in a lab setting, the resulting radiated power scales linearly with N. However, when these atoms are closely packed—specifically, localized within a space smaller than the wavelength of the light they emit—their indistinguishability with respect to a given emitted photon results in the ensemble emitting collectively, as depicted in Fig. 2.2. This phenomenon has a classical analog in phased array antennas. Here, electric fields are emitted in phase by the antennas, resulting in an intensity that is proportional to the square of the number of antennas.

Superradiance, originally predicted by Dicke in 1950s [53], has been extensively studied in a wide variety of systems including atoms and molecules [54], quantum dots [55, 56], nitrogen-vacancy centers [57], and photonic crystal waveguides [58].

To briefly introduce the superradiance phenomenon, consider N two level atoms, where $|e\rangle$ and $|g\rangle$ represent pseudospin up and down states, respectively. Operating under the fundamental assumption that these atoms cannot be discerned regarding photon emission or absorption, it becomes evident that they all interact with a shared radiation field. As a result, the system's evolution remains in a Hilbert subspace invariant to atomic permutations, occupying fully symmetric superposition

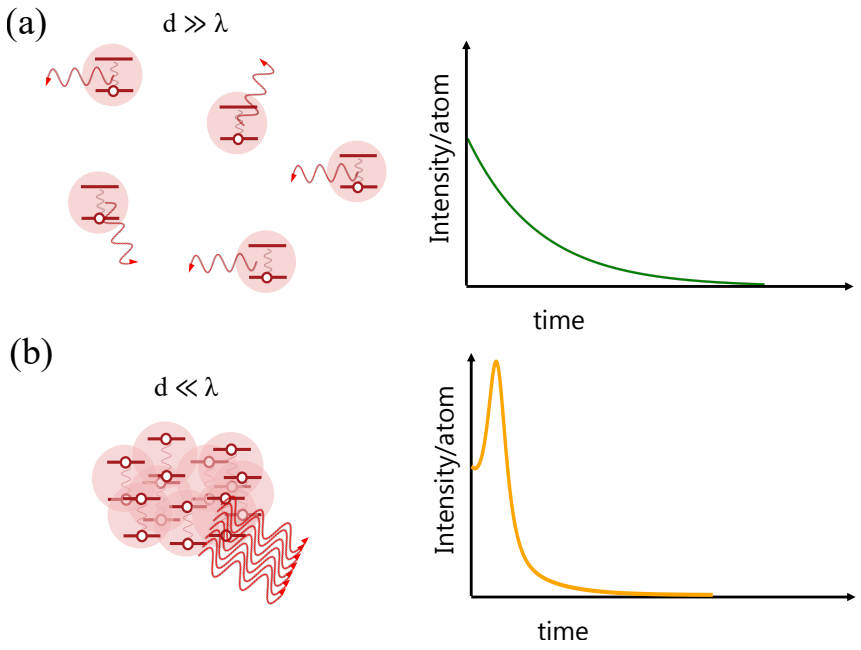

Figure 2.2: A cartoon representation of normal spontaneous emission and superradiance. (a) Depicts a set of atoms with interatomic distance, d, much greater than the emission wavelength, λ. Intensity over time is governed by the natural lifetime of the excited state and is illustrated by the plot on the right. (b) Shows an ensemble with interatomic spacing much smaller than the emission wavelength, resulting in the atoms emitting all in-phase and unidirectionally, producing a short and intense superradiant burst of light.

states. We can describe the collective eigenstates of our system with quantum numbers $J \leq N/2$, the total angular momentum, and $M = -J, -J+1, ..., J-1, J$, the z-component of J. The number of excitations in the system is given by $J + M$. We have manifolds defined by J, each encompassing a ladder of energy levels defined by M. The fully symmetric states have maximum total angular momentum and we will look at those now because those are the most superradiant.

Starting in the completely excited state $|J = N/2, M = N/2\rangle$, there are $N + 1$ states in the manifold, given by repeated action of the symmetrical collective deexcitation, or lowering, operator. The collective state raising and lowering operators describe how levels interact with the electromagnetic field and are defined as,

$$\hat{J}^{\pm}|J, M\rangle = \sqrt{(J \mp M)(J \pm M + 1)}|J, M \pm 1\rangle \tag{2.1}$$

The action of the collective decay operator, solely reduces M, but leaves J unchanged. The collective spontanteous emission rate, or intensity, into the shared radiation mode is then given by the matrix element squared of the lowering operator and written as,

$$I = |\langle J, M-1|\hat{J}^{-}|J, M\rangle|^2 = (J - M + 1)(J + M) \tag{2.2}$$

In Fig. 2.3, the fully symmetric states are depicted. Beginning with the fully excited state at the top, the first state lower represents a symmetrized summation state, with N contributions. After normalizing by $\sqrt{N}$, the resulting matrix element has a value of $\sqrt{N}$. This corresponds to the electric field of the emission. Upon squaring, the intensity becomes N. As we continue down the ladder, this intensity rises from N at $M = N/2$ (fully excited) to $\frac{1}{2}N(\frac{1}{2}N + 1)$, which is proportional to N^2, when $M = 0$ (half excited). This elucidates the increase in intensity as the system cascades down the ladder of maximally symmetric states, with peak intensity proportional to N^2, characteristic of superradiance.

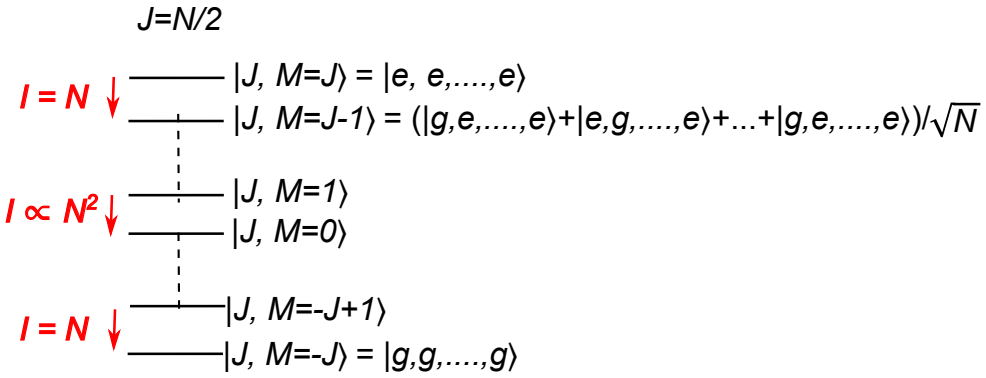

Figure 2.3: Manifold of fully symmetric states for N 2-level atoms. Beginning with the fully excited state and applying the collective lowering operator, we get to the state $|J = N/2, M = J-1\rangle$, which is a superposition of N states. The collective spontaneous emission rate (red) increases with the number of superposition states from N to $\frac{N}{2}(\frac{N}{2} + 1)$, then decreases back to N at the bottom of the ladder.

The onset of the superradiant pulse occurs when an atom spontaneously emits into the preferred mode—a stochastic event governed by the natural lifetime and the number of atoms. In this regime, the dynamics that follow give rise to hyperbolic secant-shaped pulses [54, 59], after an inherent time delay. This delay corresponds to the time necessary for the atoms to phase synchronize, enabling constructive interference. The time delay to the peak emitted intensity scales as $\ln(N)/N$ and duration of the pulse scales inversely with N.

Enhanced collective decay can also occur in extended samples, such as cigar shaped atomic ensembles, where the interatomic distance is small, but the length of the cigar is still larger than the emission wavelength. Here, the sample will have a preferential decay along the mode with the highest optical depth (OD). There is also interest in investigating the exact spacing required to achieve superradiance in ordered arrays of atoms and molecules using optical tweezers [60, 61].

In general, achieving the density required for atoms to be positioned closely compared to an optical wavelength, i.e. less than around 500 nm, is problematic. Such closeness leads to near-field interactions which cause shifts in the energy levels, which are detrimental to the precision of a clock. Alternatively, one could enhance the long-range interaction by placing two mirrors around the atoms, as in a cavity

QED system. This arrangement ensures that the atoms collectively couple to the cavity's supported mode, directing emission towards a favored decay pathway.

2.3 Atom-cavity interaction

A cavity supports discrete resonant modes, each defined by a specific frequency and spatial mode. While there are many types and designs of cavities, our focus is on the simplest: 2-mirror, single mode cavity. Precisely adjusting the distance between these two highly-reflective mirrors to match an atomic transition frequency creates an infinite range effective interaction amongst the atoms within the cavity.

The interaction of a single atom interacting with a single mode of a cavity can be described by the Jaynes-Cummings Hamiltonian in the rotating wave approximation [62],

$$\hat{H}_{JC} = \hbar\omega_a\hat{\sigma}^+\hat{\sigma}^- + \hbar\omega_c\hat{a}^\dagger\hat{a} + \hbar g(\hat{\sigma}^-\hat{a}^\dagger + \hat{\sigma}^+\hat{a}) \tag{2.3}$$

The first term represents the atom, where ω_a is the atomic transition frequency. Here, $\hat{\sigma}^+ = |e\rangle\langle g|$ and $\hat{\sigma}^- = |g\rangle\langle e|$ act as the atomic raising and lowering operators, respectively. The second term represents the cavity field, where ω_c is the cavity resonance frequency. The operators $a^\dagger$ and $\hat{a}$ represent the photon creation and annihilation functions, respectively. The third term is the coupling Hamiltonian, which either from the term $(\hat{\sigma}^- a^\dagger)$ absorbs a cavity photon and puts an atom in the excited state, or emits a photon into the cavity and lowers the atom from the excited state to the ground state with the term $(\hat{\sigma}^+\hat{a})$. The parameter g is the cavity QED coupling constant. Specifically, $2g$ is the single atom vacuum Rabi frequency describing the strength of the atom-cavity coupling, set by the atomic dipole matrix element written as,

$$\hbar g = -\hat{\epsilon}\cdot\vec{d}\frac{\omega_c}{\sqrt{2\epsilon_0\hbar V}} \tag{2.4}$$

where $\vec{d}$ is the atomic dipole matrix element of the transition, $\hat{\epsilon}$ is the polarization of the cavity field, and V is the cavity mode volume.

Rewriting the Hamiltonian in terms of a matrix,

$$\hat{H}^{(n)} = \hbar\begin{bmatrix} n\omega_c + \frac{\omega_a}{2} & g\sqrt{n+1} \\ g\sqrt{n+1} & (n+1)\omega_c - \frac{\omega_a}{2}\end{bmatrix} \tag{2.5}$$

where n is the number of radiation quanta in the cavity mode. This Hamiltonian can be diagonalized, and its two eigenvalues are associated with eigenstates $|n,\pm\rangle$, split around ω_c, with splitting,

$$\Omega_n(\delta) = \sqrt{\delta^2 + 4g^2(n+1)} \tag{2.6}$$

Ω_n is the famous vacuum Rabi splitting, where $\delta = \omega_c - \omega_a$ is the atom-cavity detuning. We observe that for $\delta = 0$ and $n = 0$, the splitting of the cavity resonances is $2g$ due to the presence of an atom in the vacuum.

Working with N ground state atoms positioned in the cavity mode, and in the regime of low saturation or weak probe ($n \ll N$), we can modify the Hamiltonian

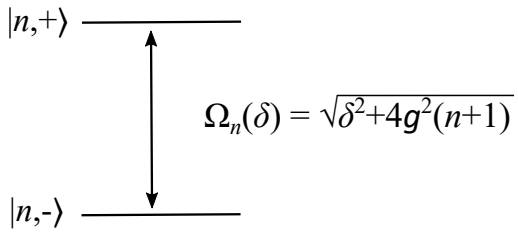

Figure 2.4: Visual of the two atom-cavity dressed modes. The cavity resonance divides, with a splitting given by the vacuum Rabi splitting.

using collective raising and lowering operators [63, 64]. This modification is known as the Tavis-Cummings model [65], and results in a collective vacuum Rabi splitting of,

$$\Omega_N(\delta) = \sqrt{\delta^2 + 4Ng^2} \tag{2.7}$$

with an on-resonance cavity, $\delta = 0$, we have $\Omega_N = \sqrt{N}2g$. This collective vacuum Rabi frequency is the rate at which photons are exchanged between the atoms and the cavity. Since this results in two distinct solutions for the atom-cavity system, it is also termed the normal mode splitting. Probing this splitting can be achieved by sweeping the frequency of a laser through the cavity across these normal modes. Rather than observing a single transmission peak corresponding to the empty cavity mode, there will be an enhanced cavity transmission observed at the normal modes, characteristic of the dressed atom-cavity system (i.e. interacting atom-cavity system).

The relevant rates in such a cavity QED system are shown in Fig. 2.5. There are two dissipative rates, the rate at which the atoms spontaneously emit into free space, Γ, and the rate at which photons are emitted from the cavity mirrors, κ. If Ω_N exceeds both κ and Γ, the system is in the collective strong coupling regime. In this regime, the two peaks are well-separated beyond the width of each peak, making the peaks highly resolved. A common objective in cavity QED systems is to ensure that this regime of resolved vacuum Rabi splitting is reached, signifying the coherent interaction rate exceeds the dissipation rates in the system.

The widths of the system's normal mode resonances in this regime are determined as weighted averages of κ and Γ. On resonance, the widths are $(\kappa + \Gamma)/2$. For large cavity detunings, one peak gets narrower (atom-like) and one gets wider (cavity-like), as demonstrated in chapter 4, Fig. 4.3.

The behavior and properties of cavity QED systems can be characterized by a single dimensionless parameter relating the absorptive, emissive, or dispersive interactions of an atom with the cavity mode. It is commonly referred to as the single-atom cooperativity or Purcell factor,

$$\mathcal{C} = \frac{24\mathcal{F}}{\pi}\frac{1}{k^2\omega_0^2} = \frac{4g^2}{\kappa\Gamma} \tag{2.8}$$

Additionally, this parameter represents the ratio of emission into the cavity versus free space, often termed cooperativity. Here, $k = \frac{2\pi}{\lambda}$, represents the wavenumber

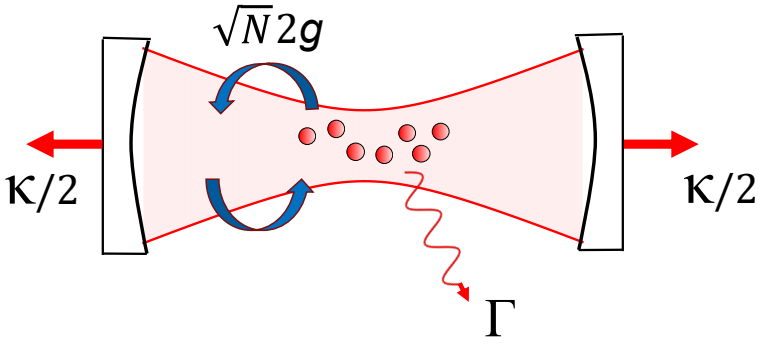

Figure 2.5: Diagram of the relevant rates in a typical cavity QED system. There is one coherent build-up rate, the collective vacuum Rabi frequency and is $\sqrt{N}2g$. There are also two decoherent rates, the cavity decay rate, κ, and spontaneous emission rate of the atoms, Γ. The particular regime of the system is defined by the hierarchy of these rates.

of the atomic transition with wavelength λ, and ω_0 denotes the cavity mode waist radius. Essentially, $\mathcal{C}$ quantifies the likelihood that an excited atom will undergo spontaneous decay into the cavity mode. When $\mathcal{C} > 1$, the system is in the "strong coupling" domain, meaning that emission into the cavity surpasses emission into free space. This dimensionless parameter is defining as it dictates the photon-atom coupling strength, and by extension, nearly all the governing physics.

Our system operates in the low single-atom cooperativity domain, with $C \approx 5 \times 10^{-4}$, but high collective cooperativity regime. The collective cooperativity, denoted as NC, represents the proportion of photons emitted by the ensemble into the cavity mode. Since we typically trap 10s of millions of atoms, we are safely placed in the collective strong coupling regime.

A few intricacies merit attention. The single-atom coupling equation assumes that the atom is in the center of the cavity mode volume and sitting perfectly at an antinode of the cavity field. In our experiment we capture atoms in a red MOT cloud and then turn off all trapping lasers. The cloud has dimensions of order 100 μm for each axis. Given that the light of the transition and inside of the cavity has a wavelength of 689 nm, the atomic ensemble spans across more than 100 wavelengths. The significant size of the MOT means the atoms are distributed randomly with respect to the sinusoidal electric field intensity of the cavity mode.

Averaging the coupling over the standing wave mode of the cavity reduces the collective cooperativity by a factor of 2, with effective quantities $N_{\text{eff}} = \frac{2}{3}N_0, g_{\text{eff}} = \frac{3}{4}g_0^2, C_{\text{eff}} = \frac{3}{4}C_0$ [66]. Taking into account the finite size of the atomic cloud compared to the cavity waist radius of 450 μm leads to a further slight reduction of the effective coupling.

2.4 Bad cavity regime

Now that we have established that we want the dominant rate in the system to be the collective vacuum Rabi frequency, Ω_N, there is still the consideration of

the ratio between atomic decay rate Γ, and the cavity decay rate κ. In the regime $\kappa \gg \Gamma$, called the "bad cavity" regime, photons are more likely to leave the system out from behind one of the cavity mirrors. Conversely, in the "good cavity" regime, $\Gamma \gg \kappa$, photons are more likely to leave the system via spontaneous emission from the atoms outside of the cavity mode. The difference between the two regimes is illustrated in Fig. 2.6.

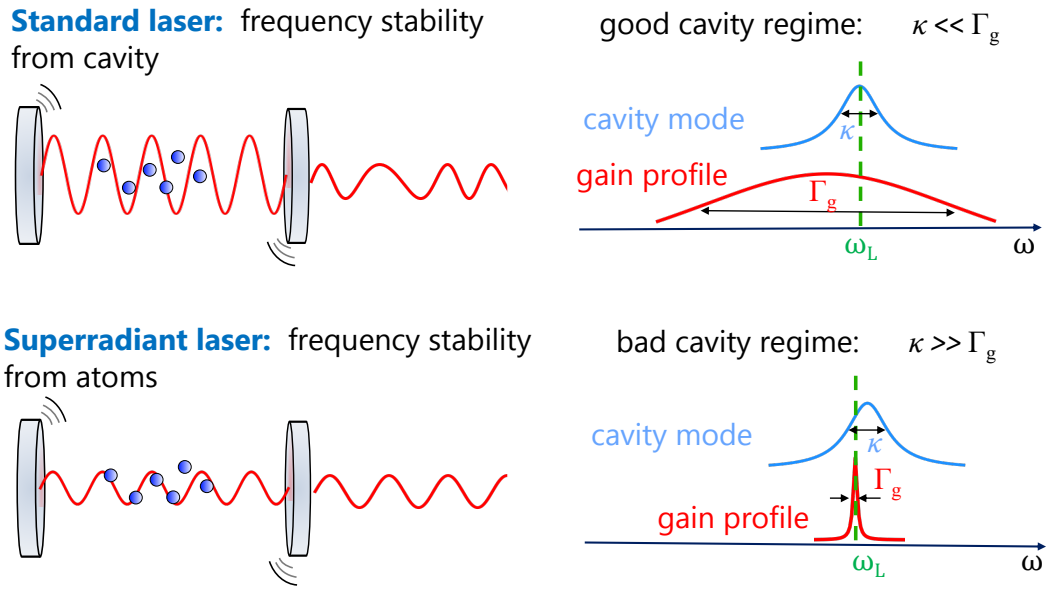

Figure 2.6: (Top) In the conventional, good cavity regime, the atomic coherence decays rapidly, and the cavity photon field acts as the phase memory in the laser. As a result, any vibrations on the mirrors, drawn as the curved lines around the mirrors, directly influence the light coming out. (Bottom) In the other extreme, the bad cavity regime, the roles of the cavity and atoms reverse. In this regime the cavity decays rapidly with the phase information kept in the atoms. Because the emission frequency is determined by the atoms, and that is the narrower spectral feature, perturbations in the cavity are highly suppressed.

In many applications, the spontaneous, non-directional loss of photons is detrimental and leads to dephasing of the atomic ensemble. Photons exiting the system via the cavity mode are much more useful as they provide collective information of the atomic ensemble and are easy to measure since they are all directed along the cavity axis rather than randomly into 4π.

Traditional lasers operate in the good cavity regime, with a broad gain medium and a narrow cavity resonance, which carves out a frequency to lase. In this system, the phase information is stored in the cavity field, and the relatively 'forgetful' atoms lock to this field, emitting light with a phase determined by the cavity. Here the quantum-limited linewidth is given by the Schawlow-Townes limit [67] as $\Delta f_{GC} \propto \frac{\kappa}{n}$, where n is the average number of intracavity photons. Since the linewidth is heavily dependent on the cavity linewidth, any noise on the cavity mirrors is written directly onto the outgoing laser frequency.

A bad cavity laser operates in the opposite regime, with a broad cavity resonance and very narrow gain medium, such as cold atoms emitting coherently on a narrow transition. Here, the atoms maintain the phase coherence over extended times, while the cavity quickly loses it. It has been proposed that in the steady-state, such a system could reach a minimum linewidth of $\Delta f_{BC} = C\gamma$, which has the potential to be exceedingly narrow [40]. In this case, the light emitted has a phase determined by the atoms and can have greatly reduced sensitivity to cavity mirror perturbations. We define the pulling coefficient $P = \Delta f_l/\Delta f_c$, where Δf_l is the change in emitted frequency due to a change Δf_c of the cavity resonance frequency. A small pulling coefficient $P \ll 1$ signifies reduced sensitivity to noise on the reference cavity, and this is desirable for a frequency reference.

The superradiant regime is going to occur in the bad cavity regime, and often in literature these terms are used interchangeably. This is because, in the bad cavity regime, the cavity decay can be much faster than the atomic decay rate. Consequently, the majority of emitted photons will leave the system along the single cavity mode, and do so superradiantly. In contrast, in the good cavity regime, the excitations are stored in the cavity photons, bouncing back and forth for a much longer time, so dissipation is more likely to occur from atomic spontaneous emission.

The system is superradiant because as the atoms interact collectively with the cavity, there arises a fundamental ambiguity of the atoms. Consider a collection of atoms in the excited state, and then one atom decays into the cavity mode and the photon is read out through a cavity mirror. We know that one atom has emitted a photon, but we fundamentally cannot determine which atom it came from. All atoms couple to the same cavity mode, contributing with the phase corresponding to their locations in the cavity mode. This makes them indistinguishable with respect to cavity emission. In other words, once the first atom spontaneously emits into the cavity, then the atoms are in a permutationally invariant, symmetric superposition of N states, which couples stronger to the next level down on the excitation ladder. This leads to an enhanced emission rate of the atomic ensemble into the cavity.

Previously in this chapter we focused on the maximally symmetric superposition states. However, we now want to consider what happens in the case of a single spontaneous emission outside of the cavity mode. This emission does not contribute to the downward cascade of states with the same J, as it is not invariant by atomic permutation. For example, by looking at the angle from which the photon came, we could determine which atom emitted it. A spontaneous emission would instigate a transition to a manifold with reduced total angular momentum $J = N/2 - 1$. This reduction continues for each spontaneous emission outside of the cavity mode.

A very useful representation for understanding this concept is the Dicke triangle picture, which can be related to a collective Bloch sphere, as shown in Fig. 2.7a. In the visualization of the Dicke triangle, collective decay corresponds to a downwards trajectory, as was the example with the perfectly symmetric state manifold in Fig. 2.3. Notably, a state on the triangle's lower-left edge ($J = -M$) lacks a vertical downward path and is therefore unable to collectively decay. These states demonstrate subradiance with respect to cavity emission.

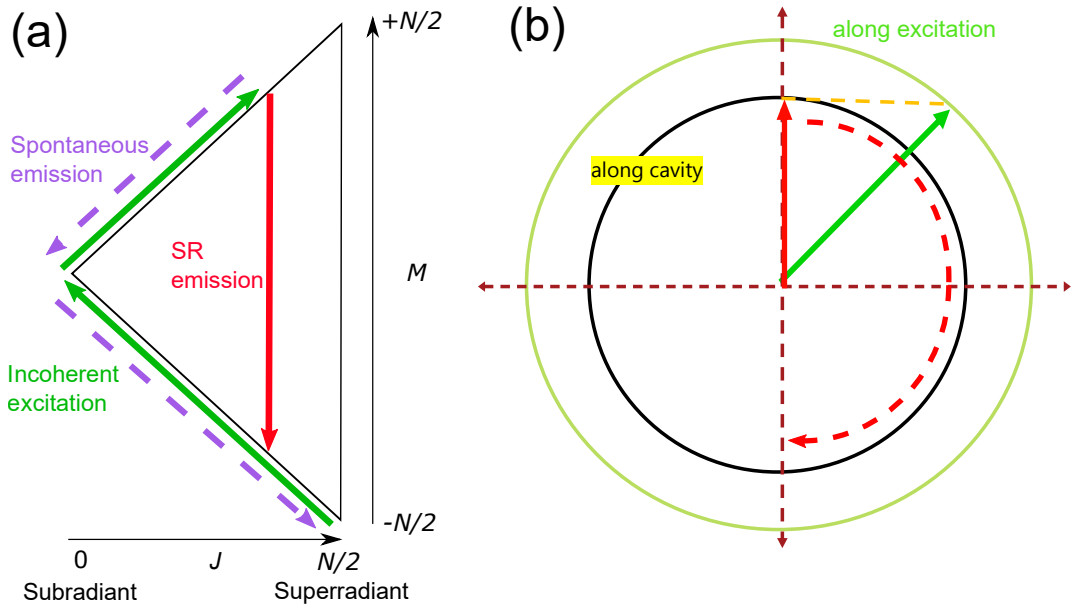

Figure 2.7: Representations of collective decay with a 80% fractional excitation as a (a) Dicke triangle and (b) collective Bloch sphere. (a) Superradiance is depicted as a vertical downward line (red arrow). If the atom would emit photons outside of the preferred (cavity) mode, the collective atomic state couples to a lower J state (purple dotted line). If we excited to 80% fractional excitation transversely to the cavity axis, this populates higher and higher states, with minimal J with regards to the cavity mode. (b) The excitation along the transverse pump direction (green arrow) projects its positive inversion onto a fully-inverted yet smaller cavity collective Bloch sphere (black). This illustrates why an 80% excitation will only emit superradiantly down to 20%, and decay spontaneously the remainder of the way.

When atoms are incoherently pumped, they populate states of increasing excitation but of lowest symmetry, or minimal J. In our experiment, such incoherent excitation is achieved by exciting the atoms transversely to the cavity axis, as depicted in Fig. 2.8. This induces random phase excitations in the atoms relative to the cavity field. Alternatively, if we chose to pump through the cavity, the atoms will be excited with the corresponding phase to their location in the cavity mode. This way the atoms will constructively interfere for any amount of excitation, and the superradiant pulses will happen much faster, since there is no time needed to synchronize the atomic dipoles. This form of excitation through the cavity mode can be represented by populating higher and higher states going directly vertically upwards on the Dicke triangle's right edge.

For an atomic ensemble to undergo collective decay when excited transversely, it is essential that positive population inversion has been achieved, denoted as $M > 0$. Then the amount of collective emission is related to how much the sample is excited beyond the 50% excitation threshold. The collective emission spans from $|J, M = +J\rangle$ to $|J, M = -J\rangle$. As depicted in Fig. 2.7, an initial excitation of 80%

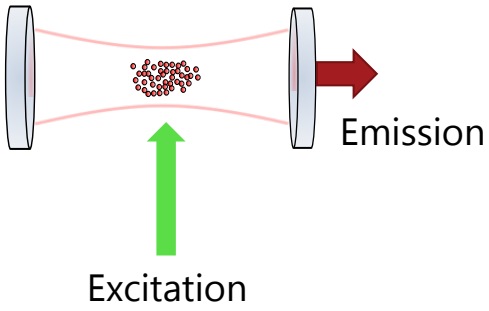

Figure 2.8: Diagram showing how we excite our atoms transversely to the cavity mode. The excitation phase is uncorrelated with the cavity mode phase.

results in collective emission down to 20%, represented by the red line.

We can relate this to a collective Bloch sphere picture, which is more familiar to atomic physicists. The green Bloch sphere in Fig. 2.7b represents the collective atomic dipole in the rotating frame of the pump pulse. After excitation, the z-component of the Bloch vector projects onto a smaller Bloch sphere, representing the collective atomic dipole in the rotating frame of the cavity mode. This vector, positioned directly on the north pole, represents a fully inverted, but smaller, atomic ensemble which can only decay to the south pole of this smaller sphere. This elucidates why the cavity decay halts at the 20% excitation level, and does not continue until all of the atoms are in the ground state. A spontaneous emission event in this collective Bloch sphere picture, brings the Bloch vector a single atom's Bloch vector length closer to the south pole.

CHAPTER 3

Experimental apparatus

In this section I will provide an overview of the experimental apparatus in the lab used for the investigations of superradiance described in chapters 4, 5, and 6. The essential components in this experiment, which are common to most cold atom experiments, are the vacuum chamber, magnetic field coils, and laser systems. Computer control facilitates and coordinates the timing of the laser systems and data aquisition is done to retrieve the experimental data in an efficient way.

The apparatus was built by several dedicated lab members, and I will mention them in the Acknowledgements section. I will focus on the experimental apparatus which I was most heavily involved with. For other parts of the experiment not explained here thoroughly, I will refer to other theses in the group.

When I joined the group in December 2019, the team had recently completed investigations of superradiant pulses from a cloud of atoms at mK temperatures, and the dynamics observed were heavily influenced by Doppler broadening. We decided to implement further cooling on the kHz transition with a red MOT stage to reduce the Doppler broadening and investigate the spectral characteristics of quasicontinous superradiance. This required the construction of a brand new set of MOT coils, as well as a stable reference laser, which are detailed below. For those interested in more details of cooling and trapping of strontium atoms or how a MOT operates, I recommend Metcalf's classic work [68], as well as Barker's comprehensive thesis [69].

3.1 Magnetic field coils

3.1.1 New MOT coils

The previous design of the MOT coils were problematic in that they were wound around a full circular copper holder. This limited how fast we could switch the magnetic fields during the blue to red MOT transfer. The mutual induction between the coils and the holder created eddy currents in the copper holder, slowing down the possible switching time of the magnetic field. This limitation reduced the number of atoms we could trap in the red MOT.

Our initial redesign involved a coil holder featuring a slit. This holder had water-cooling channels, was sealed by a lid, and used epoxy both to secure the lid and as a thermally conductive (but non-electrically conductive) agent for heat dispersion between the coil layers. However, after winding, this design presented a series of issues. The sharp bends around the slit may have cut the insulation, causing sparking between coil layers during switching. Additionally, the water cooling system persistently dislodged the lid, necessitating numerous epoxy fixes. The constant repairs led to a messy setup, prompting us to abandon the design and opt for hand-wound coils.

We purchased annealed hollow copper tubing and wound it ourselves on a lathe at our machine shop. This tubing, which has part number CW024A, was purchased from Alumeco – and proved to be an efficient and cost-effective solution. After winding these, the machine shop attached water tubing adapters to the ends. The copper tubing, with a 3 mm inner and 5 mm outer radius, was coiled into a ring as depicted in the top left of Figure 3.1.

We found that conveniently a fiber holder from Thorlabs had a radius very close to our Kimball vacuum chamber radius. Using a lathe, we wound the coils around this holder. Each coil, both top and bottom, consisted of three sections: these were water-cooled in parallel but wired in series. A single section contained three layers with nine windings each, summing up to approximately 81 windings per coil. During the winding process, kapton tape was employed as insulation around the tubing. While enameled wire was an option, we found kapton tape to be less susceptible to shorting and it was cost-effective.

Swapping out the bottom coil required removing the primary vacuum chamber. Thus, before finalizing the change, it was crucial to ensure that the new MOT coil could produce the magnetic field necessary and that the water cooling would adequately counteract the heat produced. For an in-depth discussion on the pre-implementation coil tests, along with details on coil resistances, I direct readers to Mikkel Tang's thesis [70]. Under our standard operating conditions, we maintain a water cooling pressure of about 1 bar for each coil, as this limited the temperature increase to a couple of degrees maximally.

3.1.2 Construction of switching circuitry

The rapid control and switching of magnetic fields are necessary for the transitions between blue and red MOTs in our sequence. A schematic of the control circuitry for a single coil is depicted in Fig. 3.2, a design largely influenced by [71]. Given the large size of our science chamber, achieving the required magnetic fields demands powerful currents, approximately 75 A for the blue MOT. Switching such hefty currents so quickly results in substantial power dissipation in a short time.

For this reason all of the control circuit wiring was made out of copper bars or very thick gauge wires, and the components were generally all rated for extremely high powers. To mitigate overheating, all components were mounted on copper plates equipped with water cooling. This ensured a stable operating temperature, crucial for the system's efficiency and longevity.

We control the current through the MOT coils by applying a control voltage

Figure 3.1: Winding of the hollow tubing MOT coils. Top row shows how it looked when it was newly purchased and us winding it on a lathe, coating it in kapton tape as we went along. The second row is a finished coil, which we then tested the water cooling and magnetic field before removing the vacuum chamber and placing it on the experiment in the bottom picture.

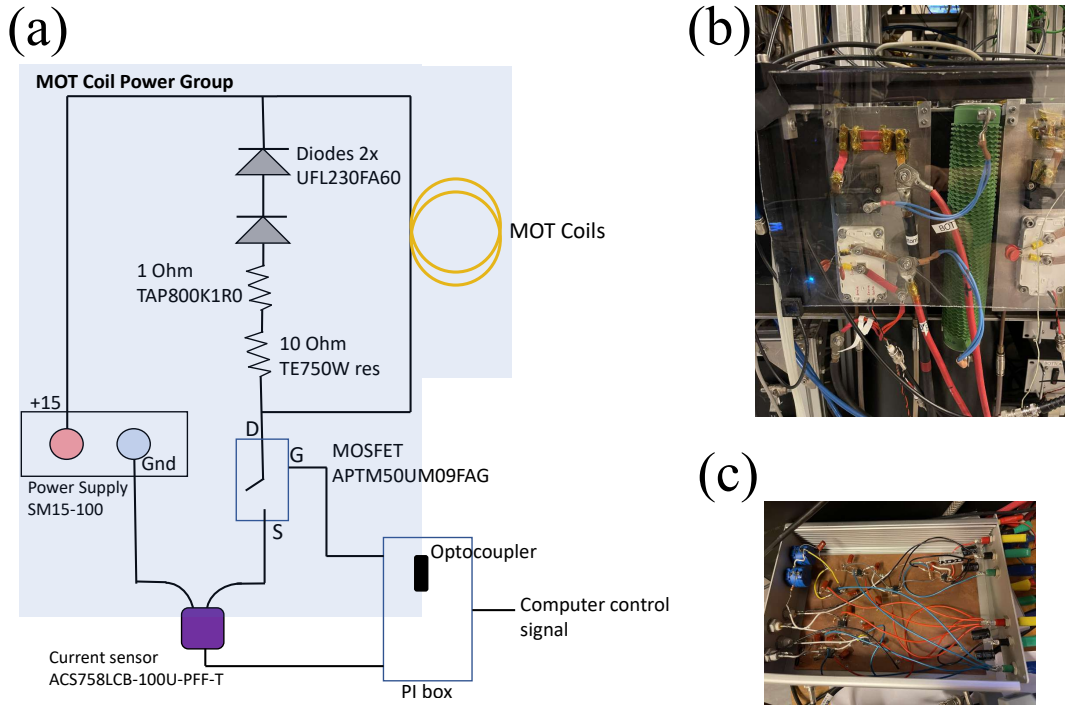

Figure 3.2: MOT coil switching circuitry. (a) Diagram of all of the components in the MOT current pathway. (b) Image of the control circuitry for one of the coils. (c) Home-built PI box based on a design from [70].

between the gate and the source of the MOSFET (APTM50UM09FAG). When we switch the fields quickly, there is a lot of energy stored in the magnetic field, and we therefore need a way to dissipate this energy. This is the job of the high power resistors and two diode section, which gets activated when the MOSFET opens and current can no longer flow through it. When this happens, the current will dissipate over the resistance repeatedly until it is at zero. After experimenting with various resistance values, we settled on a flyback circuit with 11 Ohms, allowing us to switch off the coils within 4 ms, safely and without any voltage spikes between different optical tables in the lab. Higher resistances would lead to faster switching, with occasional spiking during the switch off. The significance of controlling these spikes cannot be understated. Voltage spikes might endanger sensitive lab equipment like diodes, computers, and other devices. This concern also led us to establish a distinct power group for the MOT coils, shown with the blue background, to minimize dangerous voltage spikes in the lab.

We measure the current through the MOT coils by a Hall probe, ACS758LCB-100B-PFF-T. This probe has very small resistance and provides a voltage proportional to the current going through the device.

For a period of time, one of the connections to the Hall probe had a larger resistance than the Hall probe itself, and became very hot. We only noticed this by investigating a slight smell of burning kapton/rubber as we ran the experiment, which at the time we could not explain. By searching with an infrared camera, we quickly identified the lousy connection. Ultimately we designed a beefier copper

connector, which could be tightened with screws to make a solid fitting to the ends of the Hall probe, and this fixed the issue. Then we could leave the experimental cycle with switching uninterrupted for many hours with no issues of heating. Clamped connections are important for achieving low resistance in this circuit.

To effectively control the current passing through the MOT coils, we utilized a feedback system where the voltage from the Hall probe was fed into a PI (Proportional-Integral) control circuit. This circuitry was designed by Tang and presented in [70].

The circuits were assembled using a "dead-bug" style of circuit assembly, a method that involves mounting the components upside-down on a copper ground plate, with their legs in the air, mimicking the appearance of upturned insects. This allowed for rapid prototyping and adjustments.

This PI circuitry functions by comparing the Hall probe signal to a computer-generated reference signal. The reference signal provides the desired temporal-profile of the magnetic field strength, transitioning smoothly between high and low levels. Once the comparison is made, the PI circuit fine-tunes its output to the MOSFET, regulating the coil's current to closely follow the reference.

During our initial tests, we began with slower switching times. As we incrementally increased the switching speed, we noticed minor oscillations in the feedback path. If left unchecked, these oscillations could escalate to voltage spikes during the switching. Addressing this required iterative fine-tuning of the PI parameters. Whenever we observed improvements in damping out the oscillations by adjusting either the proportional (P) or integral (I) components but hit the limitation of the current setup, we soldered in a new resistor or capacitor to achieve the desired damping.

To maintain separation of the power groups, an optocoupler was integrated, ensuring no direct electronic connection existed between the two grounds. This optically-isolated setup provided an extra layer of security to protect the PI box and other electronics from any voltage spikes.

3.1.3 Compensation coils

We introduced three sets of bias coils wound in a near-Helmholtz configuration to achieve precise positioning of the red MOT and to ensure a homogeneous bias field during the experiments. While our existing MOT coils could provide a bias along the z-axis, they lacked the spatial uniformity in the anti-Helmholtz configuration. Each coil was wound with approximately 10 - 15 turns. Due to the spatial constraints surrounding our chamber, we positioned these coils closely around the chamber and existing coils, as imaged in Fig. 3.3. Although placing them farther from the setup might have yielded better field uniformity, our approach allowed for rapid installation within a day. These coils draw power from DC voltage supplies, with each corresponding set connected in series. With the capability to carry several amps of current, they can generate magnetic fields up to a few Gauss, corresponding to moving the red MOT by centimeters.

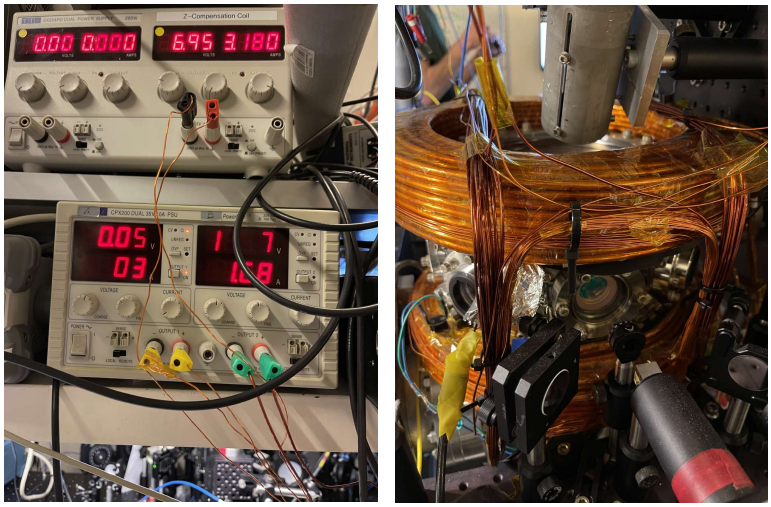

Figure 3.3: Images showing the compensation coils and the DC power supplies which control their currents.

3.2 689 nm reference laser

3.2.1 Installation of commercial cavity

Our Ultra-Low Expansion (ULE) cavity, a commercial product sourced from Stable Laser Systems as shown in Fig. 3.4, resides inside a vacuum chamber maintained at a stable pressure of approximately 1×10^{-7} Torr. This limits drifts of the cavity resonance due to pressure fluctuations.

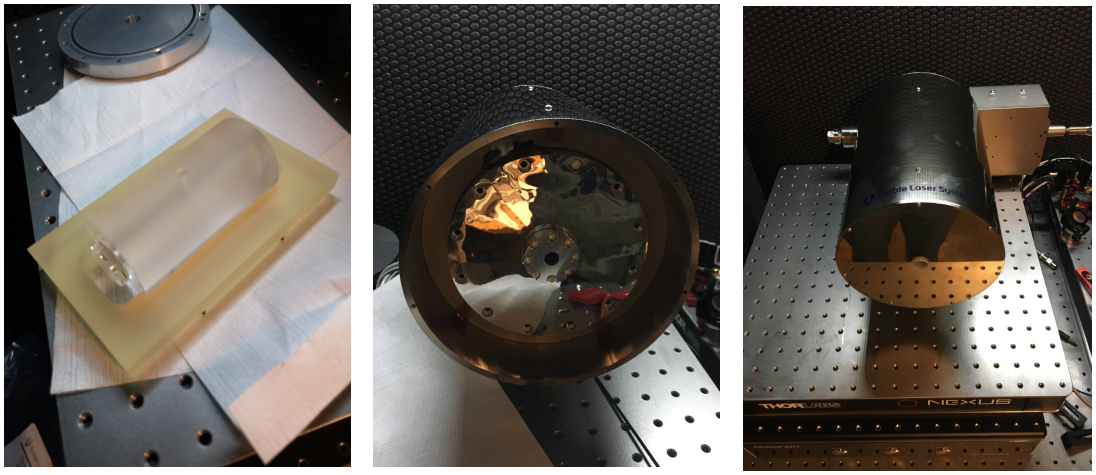

Figure 3.4: Images of the Stable laser systems reference cavity as it was setup in the experiment. In the image on the left we see the cavity holder and small black viton balls for acoustic isolation. On the right is the complete and vacuum sealed enclosure.

Critical to our setup's performance are the viton balls placed at two interfaces: four between the cavity and its holder, and another four between the holder and the vacuum chamber's inner edge. These viton balls acoustically isolate the cavity by decoupling it from external vibrations.

During the installation process, we centered the ULE cavity within the vacuum chamber using calipers. After positioning, we removed a protective tape that covered an opening on top the cavity, allowing this region to be evacuated during the pump down. The cavity holder was then seated securely inside the vacuum chamber, aligning with the designated grooves. We intentionally positioned the planar mirror towards the chamber side offering the most optical access.

3.2.2 Optics

The reference laser system operates at 689 nm and is composed of a MOGLabs CEL002 ECDL. The reference laser and cavity were installed in a quiet room, we called the "Mausoleum", which was converted from an old storage room next door to the main lab.

The beam path schematic is depicted in Fig. 3.5, with the pictures from the actual setup in Fig. 3.6. Typically we have 22 mW after the isolator out of the laser head, which we split on a polarizing beam splitter cube (PBS) with one branch of the light fiber coupled to the adjacent breadboard for Pound-Drever-Hall (PDH) locking to the reference cavity and the other being sent to the lab for experiments. To frequency shift the light accordingly, for the cavity and atomic resonances, acousto-optical modulators (AOMs) were used. With all of these components, typical working powers were 1.6 mW in the main lab, and 15 μW measured directly in front of the reference cavity.

One issue was that the internal diode lens tube and output coupler (OC) would drift, causing the threshold current to increase by itself over time. This required realignment on average every 1-1.5 months. The wavelength filter inside the ECDL is very narrow, and tiny drifts in the angle can lead to dramatic changes in transmission for a specific laser frequency. Once it drifted significantly enough, there would not be enough power for both locking well to the reference cavity and the experiments, and realignment was required. We fix up the alignment by adjusting the pressure on the lens tube and OC assembly. We increase the tension on the lens tube and output coupler adjustment screws very slightly to try and increase output power for a diode current slightly below threshold. After a successful realignment process, the threshold was about 105 mA. Over time, without opening the laserhead, this threshold will increase to around 120 mA in about a month. We operate the diode at around 185 mA.

Each time we did this realignment, it would cause further misalignment throughout the beam path. To minimize the work needed to get this back, we added irises and two mirrors directly after the isolator, which could usually recover the alignment pretty close to where it was prior to adjustment.

After an exchange with MOGLabs in October of 2020, they agreed to fix it at no cost. While I was at DFM, and my group was working on switching the MOT coils, we sent it back. They reported that the diode installed has a large

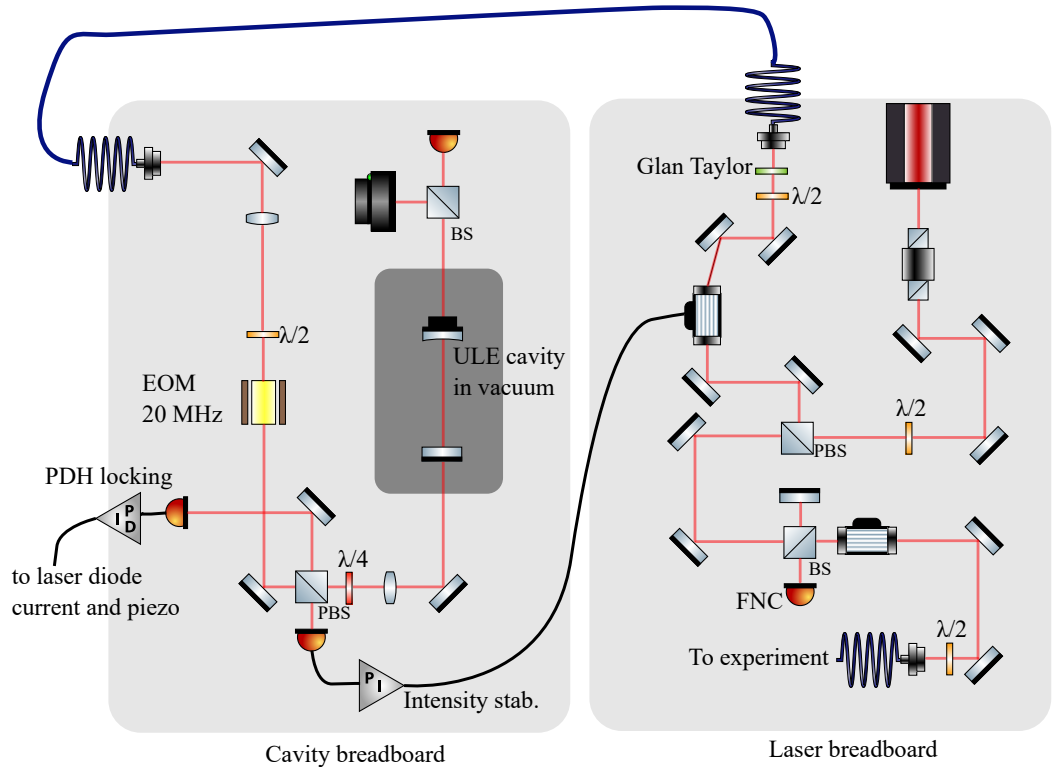

Figure 3.5: Reference laser beam path, including branches going to the reference cavity and to the experiment.

astigmatism, making it very sensitive to alignment. So they did a recollimation of the bare diode. Further the set screws have nylon tips, which get damaged over time. They said the set screws were worn out a bit, and they replaced those. As far as they could tell nothing was loose or broken. The laser was tested over a few weeks and appeared to be stable. The whole process from when we sent it off until we got it back took about five weeks.

Although it required realignment less often after we got the laser back, it was still every two months. Throughout my PhD, I would check that the laser was locking well and had enough powers each morning, to let my colleagues know if a 'realignment' was soon needed. Even though we had this continuous issue, the laser system worked well enough that we just considered it a regular maintenance job in the experiment.

Now at the end of my thesis, I spoke with MOGLabs representatives at the ICOLS conference and they said they would upgrade the system for free. Since we have been experiencing a continual rising of the minimal threshold we could achieve from realignment, we decided to take them up on this generous offer, as we had some down time from experiments.

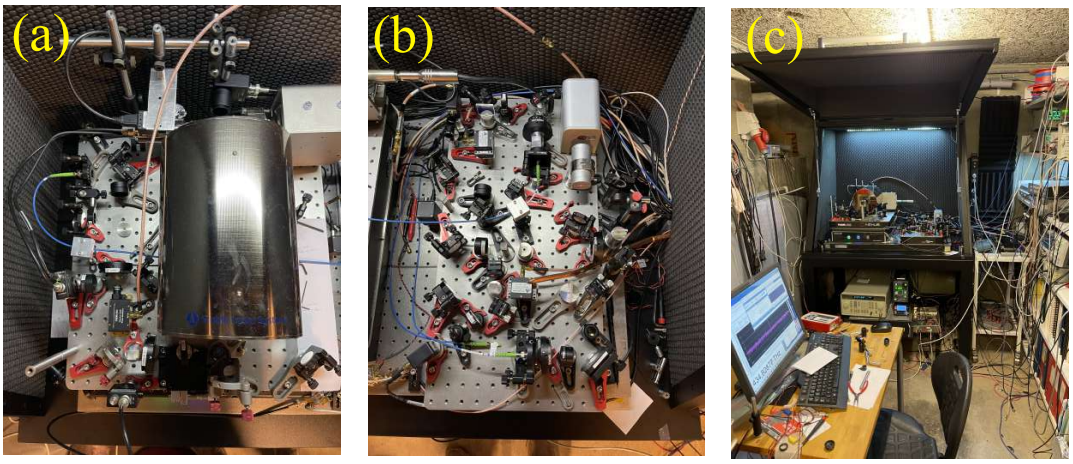

Figure 3.6: Reference laser setup (a) Cavity breadboard (b) Laser breadboard (c) "Mausoleum" showing the acoustic enclosure and computer control.

3.2.3 Alignment into cavity

The initial phase of my PhD revolved around setting up the cavity and achieving a stable lock on the laser. Central to this process is the efficient coupling of the laser to the cavity's fundamental mode. To accomplish this, we followed the protocol detailed in section 2.9 of Nagourney's work [72].

The primary task was to determine the beam waist radius corresponding to the fundamental mode of our hemispherical cavity geometry at the positions of the two cavity mirrors. Employing Gaussian beam propagation principles, the beam waist radii at the mirror locations were calculated to be 209.4 μm and 234.2 μm, respectively.

To establish these beam radii, a beam profiler was set up at approximately distances equal to where the cavity mirrors are located. By testing a few lens combinations, and mounting one of the lenses on a translation stage for fine adjustments, we were able to approximately achieve these beams sizes. Next, we placed a Charge Coupled Device (CCD) camera in the beam path of the transmitted light to identify which modes we were coupling into as we scanned the frequency of the laser across a cavity free spectral range (FSR). Using the two final mirrors before the cavity, we could walk the beam until lower-order TEM modes were displayed on the camera, as can be seen in Fig. 3.7.

After reaching a first TEM_{00} mode, we initiated locking using the PDH method. We monitored the transmitted intensity with a photodiode while locked, and could make minor adjustments to beam alignment to increase the transmitted intensity and thereby improve the coupling.

The optimal power for stable locking, characterized by the servo bumps being pushed out from the carrier frequency, was found to be 18.6 μW before entering the cavity. The intensity of the outgoing light of the cavity is 0.50 μW, allowing us to determine the intracavity power to be 45 mW.

MOGLabs reports our laser model to have a fast linewidth of <150 kHz, while the linewidth of the cavity is about 6 kHz. The coupling efficiency can be determined

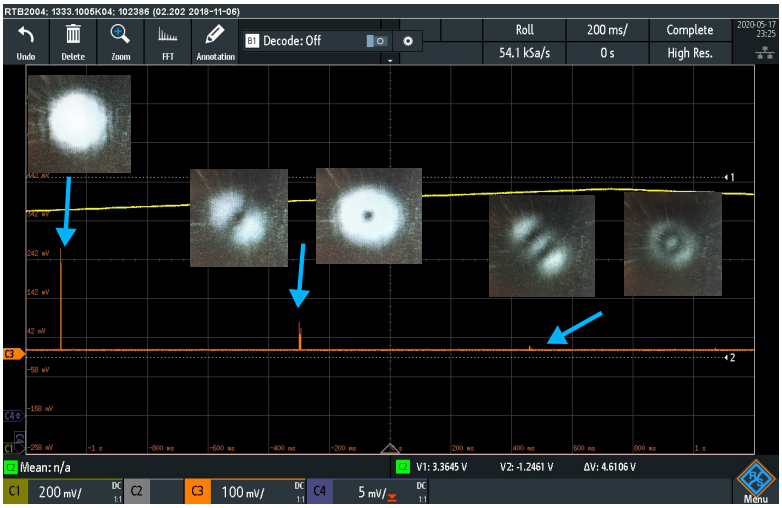

Figure 3.7: By scanning the frequency across the cavity's lowest order modes and monitoring the transmitted intensity via a photodiode, we identify distinct transverse electromagnetic modes. These include the TEM_{00} and TEM_{01} modes. Based on the alignment, we either observe the Hermite-Gaussian (rectangular) or Laguerre-Gaussian (circular) modes.

by dividing the transmitted power at the carrier frequency by the power of the resonant light before the cavity. Given that our modulation depth ensures roughly 50% of the power resides in the sidebands, this translates to a coupling efficiency of about 5%. Given our fast laser linewidth this may be close to the optimal coupling efficiency we can achieve, as was confirmed in an email correspondence with Matt Notcutt from Stable Laser Systems.

3.2.4 Pound-Drever-Hall locking

Optical cavities define a series of narrow resonances in the frequency domain. A common way to stabilize a laser to such a resonance is through frequency modulation, of which the most commonly used is the PDH stabilization scheme [73], where frequency modulation is performed at a much higher frequency than the cavity linewidth.

Experimentally, this technique introduces phase modulation to the laser frequency using an electro-optic modulator (EOM), as shown in Fig. 3.8. The error signal is generated by mixing (demodulating) the phase-modulated reflected beam with the modulation frequency. To separate the reflected beam, a combination of a PBS and a $\lambda/4$-waveplate is used. The reflected beam is then detected using a high-bandwidth photodiode, and this signal is amplified and mixed with the RF modulation frequency, with a phase adjustment. This phase adjustment is necessary due to differing phase delays in the two signal paths at the input of the mixer.

There are several reasons PDH locking is advantageous and widespread. Firstly, there are no restrictions on the modulation frequency employed. A higher modulation frequency reduces $1/f$ noise, common in most electronics. Also, lock bandwidth

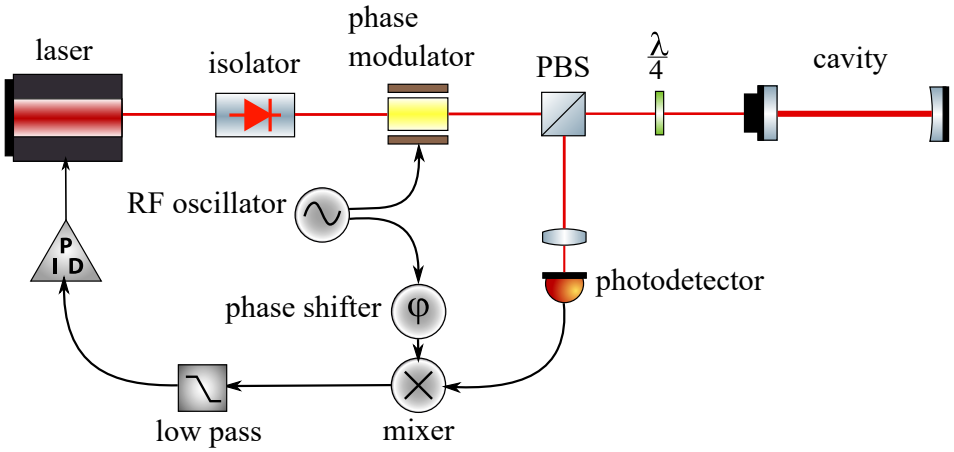

Figure 3.8: Diagram of PDH locking scheme. The laser light is phase modulated and the reflected beam from a reference cavity is picked up on a photodector. This signal is demodulated with a phase shift, yielding an error signal which can be used to continuously tune the laser onto resonance.

is not restricted by cavity linewidth.

The reflected light comprises two components: one originating from the immediate reflection off the initial mirror without entering the cavity, and the other being a small leakage beam that comes from within the cavity and exits through the front mirror. When the laser is precisely on resonance, these two beams exhibit a phase difference of exactly π, leading to a vanishing reflected beam. However, even a slight deviation of the laser from resonance introduces a phase mismatch with the cavity-emitted light. This mismatch yields a reflected intensity characterized by phase asymmetry around the resonance point.

The theory of this technique is extensively discussed in various sources, such as by Black [74]. As this forms the basis for the stability of our reference laser, we briefly discuss the important results of the PDH locking technique.

After a beam passes through an EOM, its electric field is phase modulated and becomes,

$$E_{inc} = E_0 e^{i(\omega t + \beta \sin \Omega t)}. \tag{3.1}$$

which can be expanded using Bessel functions,

$$\begin{aligned} E_{inc} &\approx E_0[J_0(\beta) + 2iJ_1(\beta)\sin\Omega t]e^{i(\omega t)} \\ &= E_0[J_0(\beta)e^{i(\omega t)} + J_1(\beta)e^{i(\omega+\Omega)t} - J_1(\beta)e^{i(\omega-\Omega)t}] \end{aligned} \tag{3.2}$$

Here, β denotes the depth of phase modulation, and Ω represents the frequency of phase modulation. For simplicity, we disregard higher-order terms at harmonics of the modulation frequency. This representation makes it evident that three distinct beams impinge on the cavity: one at the frequency ω and two sidebands at $\omega \pm \Omega$.

In the regime where the modulation index is small ($\beta < 1$), the majority of the power resides in the carrier and the first-order sidebands. If we denote P_0 as $|E_0|^2$,

the power at the carrier frequency is defined as $P_c = J_0^2(\beta)P_0$, while the power in the phase-modulated sidebands is defined as $P_s = J_1^2(\beta)P_0$.

The reflected intensity results from multiplying each component of the electric field by the reflection coefficient corresponding to that frequency. For a lossless symmetric cavity, the reflection coefficient is given by,

$$F(\omega) = \frac{E_{ref}}{E_{inc}} = \frac{r(\exp i\frac{\omega}{\Delta\nu_{FSR}} - 1)}{1 - r^2(\exp i\frac{\omega}{\Delta\nu_{FSR}})}. \tag{3.3}$$

where $\Delta\nu_{FSR}$ is the FSR. This yields a reflected electric field of,

$$E_{ref} = E_0\left[F(\omega)J_0(\beta)e^{i\omega t} + F(\omega+\Omega)J_1(\beta)e^{i(\omega+\Omega)t} - F(\omega-\Omega)J_1(\beta)e^{i(\omega-\Omega)t}\right] \tag{3.4}$$

The power of the reflected beam will exhibit interference terms at Ω, resulting from the interaction between the carrier and the sidebands, as well as terms at 2Ω arising from the interaction between the sidebands. The components oscillating at frequency Ω possess both real and imaginary constituents.

The key feature is that if we use a high modulation frequency, $\Omega \gg \delta\nu_c$, where $\delta\nu_c$ is the cavity linewidth, and the carrier is near resonance, the sidebands are completely reflected, indicating $F(\omega \pm \Omega) \approx -1$. The interference terms will then have a zero real part, but there will be an imaginary part, which yields a phase shift. Setting $E_0^2 J_0(\beta)J_1(\beta) = \sqrt{P_c P_s}$ for carrier power P_c and sideband power P_s, and following the derivation provided by Black, the resulting expression for the reflected power becomes,

$$P_{ref} = P_{c,ref} + 2P_s - 4\sqrt{P_c P_s}Im\{F(\omega)\}\sin\Omega t + (2\Omega \text{ terms}) \tag{3.5}$$

The reflected power on resonance vanishes. By mixing the output of the photodiode with modulation frequency, we can extract terms at Ω, which are the ones of interest as those sample the reflected carrier. Near resonance, considering a small deviation $\delta\omega$ compared to cavity linewidth, and employing the approximation for a high finesse cavity ($\mathcal{F} \approx \pi/(1-r^2)$), results in the following error signal,

$$\epsilon \approx -8\sqrt{P_c P_s}\frac{\Delta\nu}{\delta\nu_c} \tag{3.6}$$

Therefore, the discriminator slope around resonance is linear, with slope,

$$D = -8\frac{\sqrt{P_c P_s}}{\delta\nu_c}) \tag{3.7}$$

The slope demonstrates an inverse relationship with the cavity linewidth and is directly proportional to the product of the power in both the carrier and sideband. The optimal modulation depth is achieved at $\beta \approx 1$, which maximizes the product of $J_0(\beta)J_1(\beta)$.

This equation retains linearity in the proximity of resonance, thereby enabling the application of conventional control theory techniques. One significant advantage of PDH locking lies in its ability to maintain a lock on the zero-point intensity of the reflection. This characteristic effectively decouples frequency noise from

intensity noise. Additionally, the utilization of reflection as the locking mechanism eliminates any constraints posed by the cavity's bandwidth.

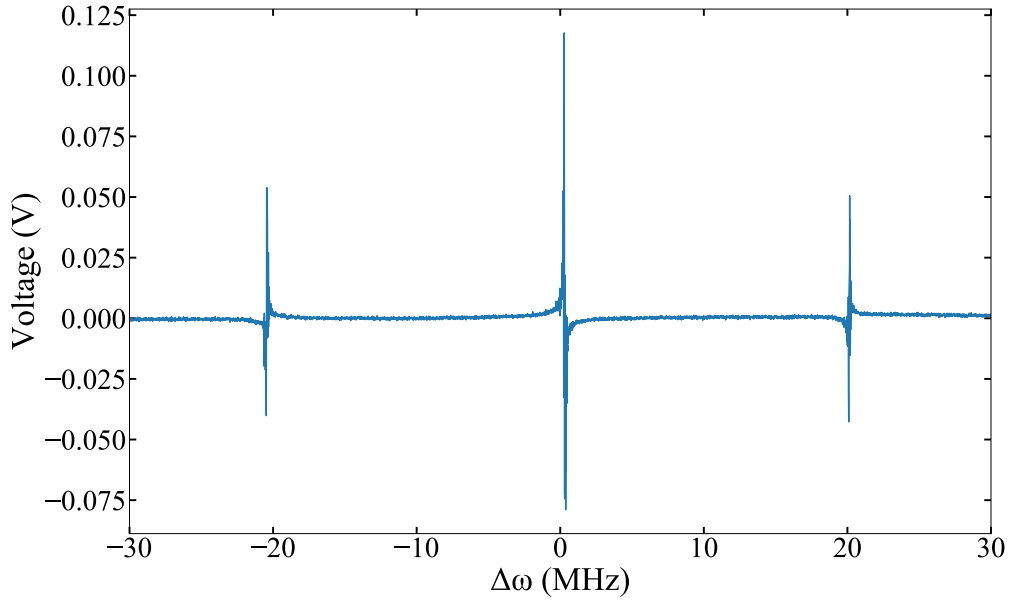

Figure 3.9: PDH error signal oscilloscope trace taken from an output coupler. Careful steps were taken to remove parasitic etalons which appeared on the demodulated error signal.

We employed the MOGLabs FSC100 Fast servo controller for implementing feedback based on the PDH error signal. Our approach closely adhered to the instructions outlined in the manual [75].

The locking procedure comprised the following steps. Initially, the error signal was adjusted using FREQ OFFSET until the primary carrier in the PDH signal was positioned on the left-hand side of the scan. Subsequently, the FAST lock was activated by switching from "scan" to "lock". Once the fast lock was on, the slow lock was engaged. Lastly, if a 20 MHz component was detected on the spectrum analyzer, fine-tuning of the ERR OFFSET was performed.

The optimization of locking parameters was done by analyzing the spectrum of the error signal as well as Allan deviation measurements. The parameter settings we settled on, listed from left to right, are as follows: SLOW INT = 75 Hz, FAST INT = 200k, FAST DIFF/FILTER = 250 kHz, DIFF GAIN = 12, and GAIN LIMIT = MAX. We monitor the in-loop error signal using a 20 dB directional coupler, which yielded the spectrum depicted in Fig. 3.10. The main servo bumps are round and pushed out to about 1 MHz, signifying the bandwidth of the lock. Above this frequency, the circuit can not feedback on the signal sufficiently fast.

The presence of inner peaks in the spectrum, possibly attributed to the rapid piezo resonances around 30 kHz inherent in the cateye laser, prompted us to investigate further. Through extensive dialogue with MOGLabs, the 30 kHz resonance remains a consistent observation in many of their systems, even with

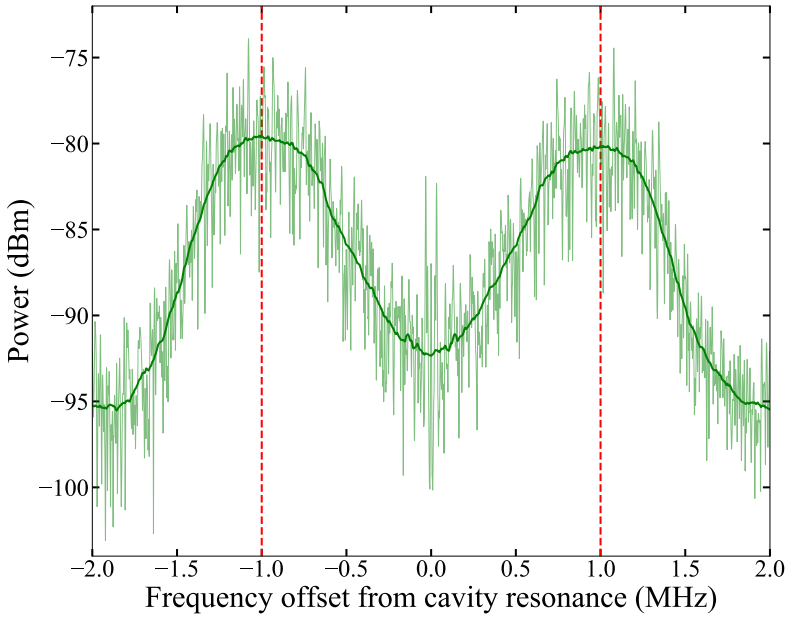

Figure 3.10: Spectrum of the error signal when the lock is engaged. Main servo bump resonances occur at 1 MHz. There are inner peaks around 30 kHz, but these did not seem to impede our ability to reach low frequency instabilities. The signal is reduced by 20 dB since we measure through a coupler, and measured with a resolution bandwidth of 5.2 kHz.

piezos of differing dimensions and capacitances. We decided to ignore these peaks as they did not limit us from reaching a frequency instability of below 20 Hz. MOGLabs mentioned that Menlo Systems could achieve sub-Hz with their cateye lasers, however, using their own custom-built electronics.

3.2.5 Finesse measurement

We can measure cavity photon storage time, τ, by stabilizing the laser to the optical cavity, then using an RF switch to quickly extinguish the laser power. This is called a cavity ringdown measurement, and results in an exponential decay of the cavity transmission, as depicted in Fig. 3.11. Our reference cavity is characterized by a length of $L = 10$ cm. Through the fitting of the ringdown time, we obtained a value of $\tau = 45.3(1)\mu$s. Utilizing this value, we can calculate the finesse to be $\mathcal{F} = 284,400$ by using the equation,

$$\mathcal{F} = \frac{c\pi\tau}{L} \tag{3.8}$$

Further, from the relation $\mathcal{F} = FSR/\delta\nu$, this results in a cavity linewidth of $\delta\nu = 5.28$ kHz.

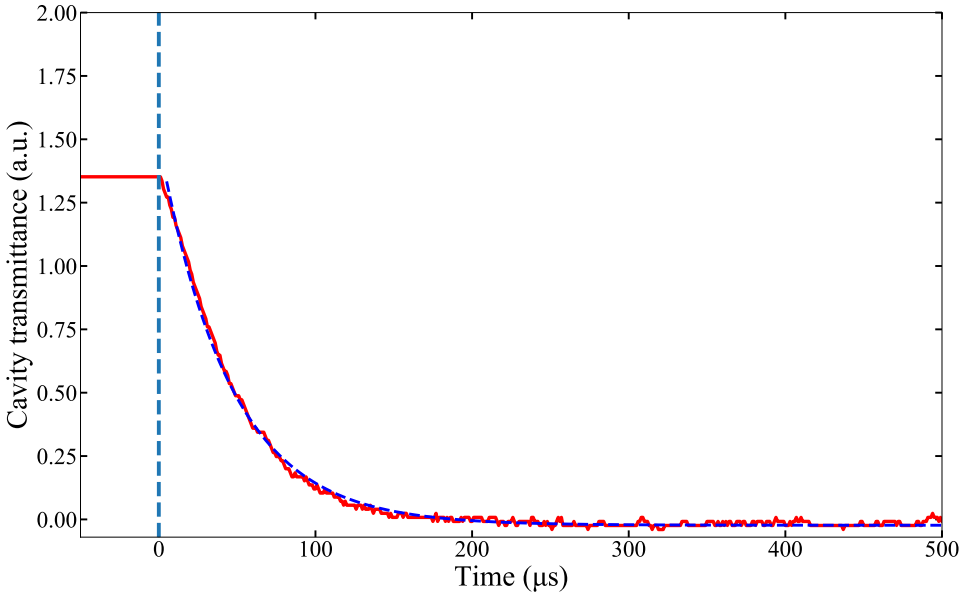

Figure 3.11: Measurement of the cavity photon storage lifetime. The laser was actively stabilized to the optical cavity and its power was abruptly extinguished by the switch off of an AOM. The resulting intensity data, represented by the solid red trace, exhibited an exponential decay. An exponential fit, depicted by the dashed line, yields a ringdown time of $\tau = 45.3(1)$ μs and a finesse of $\mathcal{F} = 284,400$.

3.2.6 Beat detection and frequency stability measurement

Our investigations of the 689 nm laser systems, and data on the collective atomic emission which we report later on in the thesis, relies on beat measurements against the reference laser. We send in light from the Mausoleum in a fiber-noise cancelled fiber, as depicted in Fig. 3.12. To conduct the beat measurement, we achieve an overlap between the reference laser and the "clock laser", another cavity-stabilized laser at 689 nm in our lab, by using a BS. We direct the combined beams onto a photodetector. This setup produces a signal at the frequency difference between the two lasers, a technique known as heterodyne beatnote detection. These measurements were centered around 42 MHz, a frequency comfortably within the operating range of the photodetector and associated electronics.

We optimize the beat signal between the reference laser and the science cavity output by applying sidebands one FSR away, producing light near atomic resonance. We then overlap this light from the cavity with the reference laser on the APD. After tweaking the overlap of the beams while looking on a spectrum analyzer, we were able to get a beat signal which was about 30 dBm above the background noise level.

For a stability measurement, we use a frequency counter, which counts a frequency over a given time interval. By analyzing the frequency counts using the Allan deviation, we can observe how the beat frequency instability averages

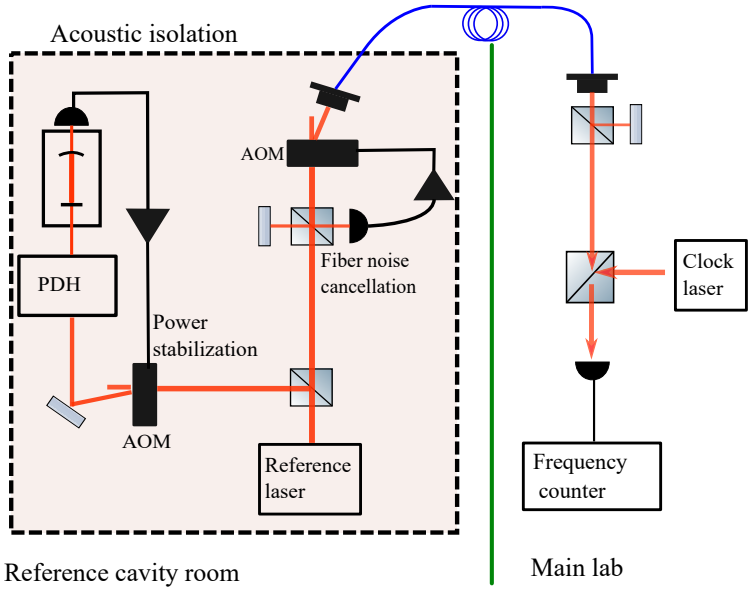

Figure 3.12: Reference laser and beat measurement schematic. Light is sent over from the Mausoleum, where the light is stabilized using PDH to the high finesse reference cavity. A portion of the light in the main lab is picked off for fiber noise cancellation. The remaining light is overlapped with a beam from the clock laser and detected on an APD connected to a frequency counter.

down over time. With all of the locks engaged, we were able to reach a frequency instability of 20 Hz, corresponding to a minimum fractional frequency instability of 4.6×10^{-14}, at approximately 500 ms. The beat averages down as $1/\sqrt{\tau}$, as does white frequency noise, before a drift in the system occurs, causing the Allan deviation to increase. We believe the measurement is limited by the clock laser and not the reference laser. This is because adjustments to the locking parameters on the clock laser continued to decrease the ultimately achievable instability, while adjustments to the reference laser had no effect on decreasing the resulting Allan deviation.

In the investigations of superradiance, the pulses are so short that we do not analyze the beat signals using the Allan deviation. To extract the intensity over time, we used a Hilbert transformation of the APD beat signal trace. To monitor the frequency over time as in the quasicontinous investigations, we divide the pulse into time windows and construct a spectrogram, or moving Fourier transformation.

3.2.7 Fiber noise cancellation

Adopting a concept introduced by Jun Ye's group [76], we established a fiber noise cancellation (FNC) system. This setup entailed the transfer of light originating from the Mausoleum to the primary laboratory space via a 50 m fiber. The fiber was routed through openings in the ceiling connecting the lab and the workshop. While efforts were made to mitigate acoustic noise through the use of a cylindrical styrofoam holder, complete coverage was not feasible for the entire length of the

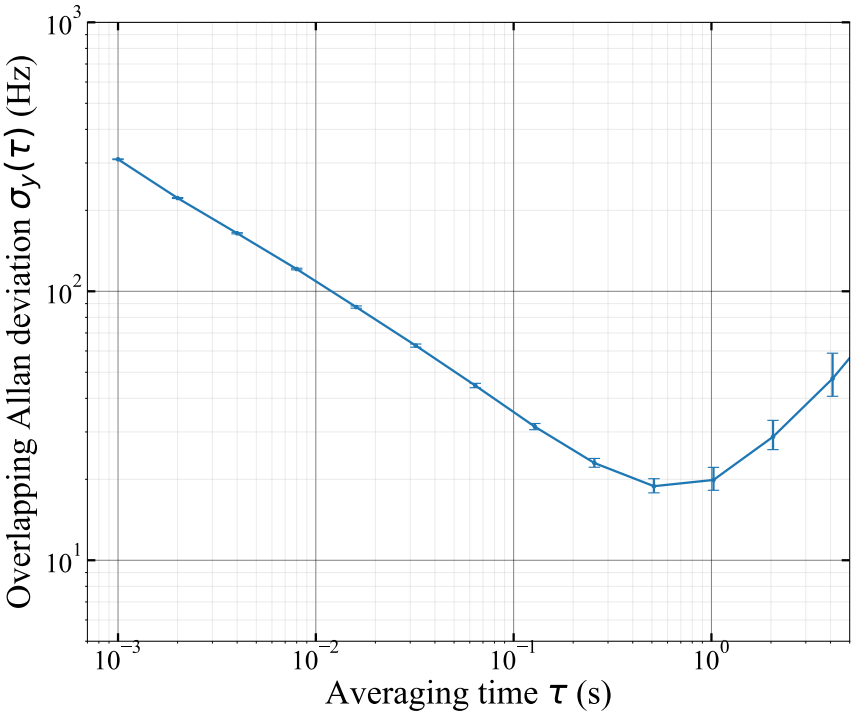

Figure 3.13: Overlapping Allan deviation of a beat signal between the reference laser and clock laser. The beat frequency instability averages down with a slope of $1/\sqrt{\tau}$, limited by white frequency noise, until reaching a minimum at 20 Hz and 500 ms. We believe this frequency instability is limited by the clock laser.

fiber. Notably, the fiber is susceptible to heat fluctuations, acoustical noise, and vibrations. Compensating for these phase fluctuations is necessary for achieving exceptionally low fractional frequency instabilities.

While we demonstrated the effectiveness of FNC in achieving Allan deviations below 100 Hz, as depicted in Fig. 3.14, during the main experiments we did not consistently employ it. There is significant power loss when setting up the reflection and fiber coupling going back to the Mausoleum from the main lab. Given that frequency instabilities below 100 Hz were not necessary for our experiments, we prioritized utilizing the extra power.

3.2.8 Other sources of noise and drift

As cavities are not universal references, each one is manufactured slightly different and are susceptible to instabilities. An instability is any effect that causes the length of the cavity, or distance between the mirrors to change. This causes a shift in the cavity resonance by $\delta f/f = -\delta L/L$. Here we briefly mention a few of them.

We implemented a power stabilization of light entering the cavity. We use the rejected port of the PBS used in the PDH locking and monitor this power on a photodiode. We then use the PyRPL program on a RedPitaya device as a PI,

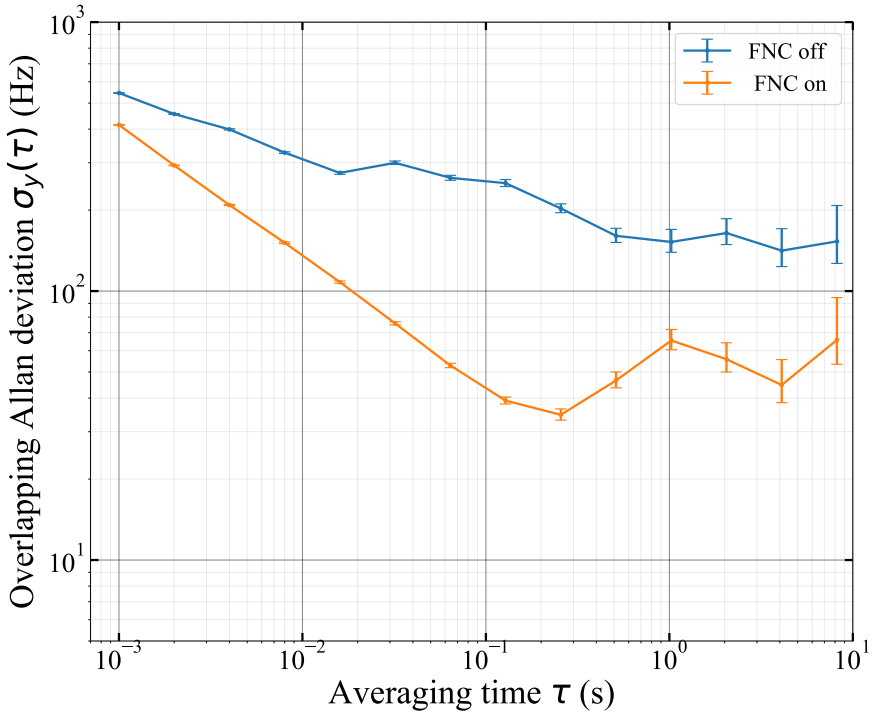

Figure 3.14: Overlapping Allan deviations of the beat between the reference laser and clock laser with (orange) and without (blue) the fiber noise cancellation engaged. We observe without the fiber noise cancellation, Allan deviations will not average down below 100 Hz.

which feedbacks to an attenuator on the AOM driver. In Fig. 3.15, we analyze the error spectrum of the PDH signal for various stabilized intensities before the cavity. We see that as we increase the power before the cavity, this corresponds to increasing gain in the servo loop, as it pushes out the servo bump peaks to higher frequencies. For our experiments we have selected 18.5 μW to use before the cavity, as we determined this as a good balance without too sharp servo bumps.

Ideally the DC value of the error signal should be zero. Residual amplitude modulation (RAM), is a term referring to amplitude noise the EOM generates at the phase modulation frequency. For example, temperature-dependent stress induced birefringence could cause this. This would result in a non-zero baseline and lead to a drifting lock point frequency. The RAM is reduced in our experiment by using a Glan-Taylor polarizer in front of the fiber before the EOM. For the experiments in this thesis, we were not limited in stability by this issue. For a more in depth discussion and feedback technique to compensate for this effect, I guide the reader to [39].

We notice a steady drift in the reference laser frequency over time. This is due to the material creep of the ULE cavity. We need to adjust the driving frequency of the AOM between the reference laser and the experiment every few weeks. We

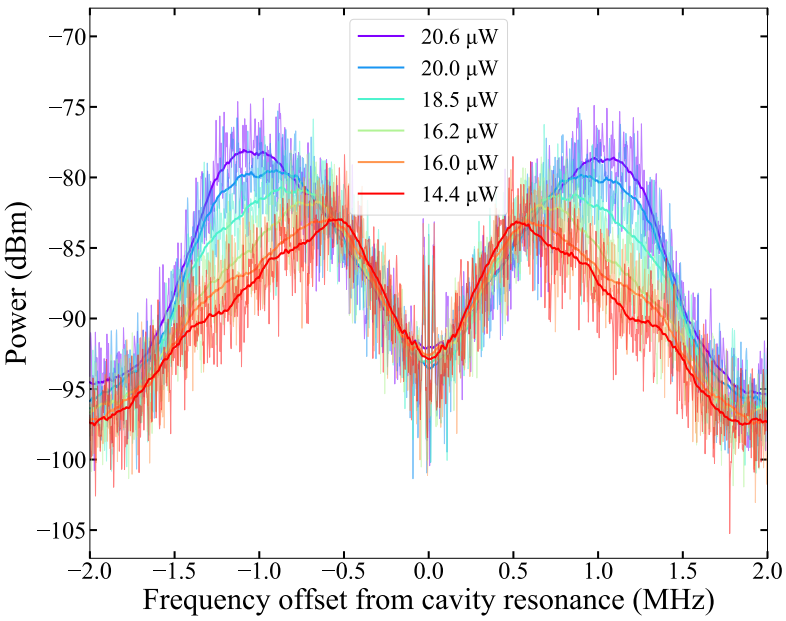

Figure 3.15: The PDH error signal spectrum for varying pre-cavity intensities, with slow feedback to the ECDL piezo, fast feedback to the laser diode current, and power stabilization. This spectrum is measured through a directional coupler before demodulation. The different colors represent various intensities before the cavity, as labeled in the legend. We see that for higher intensities, the servo bump peaks get pushed out resulting in a higher feedback bandwidths. Solid lines are error spectrums with kernel smoothening to better locate the peaks.

optimize for atom number in the red MOT, without changing any other frequencies induced on the 689 nm cooling light. Plotting these adjustments over time, as shown in Fig. 3.16, we calculate an average drift of 6.2(7) kHz/day, or 72(8) mHz/s. This corresponds to a cavity length drift of about 1.4 pm over the course of a day. For comparison, cryogenic single-crystal optical cavities which are the state-of-the-art, report a constant drift of as little as 8 Hz/day [77].

The ULE cavity exhibited a zero crossing between thermal expansion and contraction at a reported temperature of 31.8°C from Stable Laser Systems. To stabilize the cavity at this specific temperature, we employed an LFI-3751 temperature controller. Given that we successfully achieved the required linewidths for our experiment, we deemed it unnecessary to further investigate this particular effect.

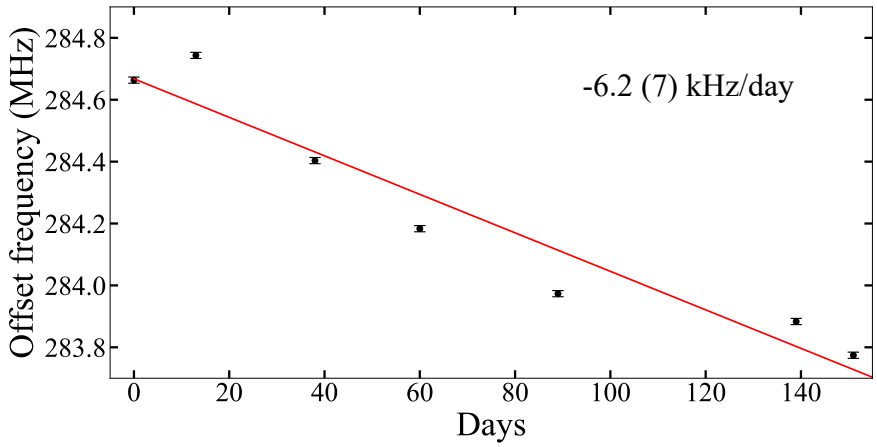

Figure 3.16: Drift of the reference laser frequency noted by each time we adjusted the AOM, shifting the frequency of the light from the Mausoleum to the main lab. A best fit line shows a drift in the cavity resonance of 6.2 (7) kHz per day. Error bars were determined based on the precision to which we could locate the optimal frequency offset during an adjustment.

3.3 Other laser systems

Conducting experiments with strontium requires multiple lasers. I briefly describe the laser systems besides the reference laser in this section, with a summary in Table 3.1. I give the powers of the lasers before hitting the windows of our vacuum chamber in Table 3.2, with approximate saturation parameters.

Transition	λ **(nm)**	**Functions**	**Stabilization method**
$^1S_0$ to $^1P_1$	461	Zeeman slower, 1st stage MOT, imaging	Modulation transfer spectroscopy in hollow-cathode lamp
$^1S_0$ to $^3P_1$	689	2nd stage MOT, pump pulse, repump, cavity probe, heterodyne frequency reference	PDH using a reference cavity
$^3P_0$ to $^3S_1$	679	Depopulate $^3P_0$	transfer cavity or free-running
$^3P_2$ to $^3S_1$	707	Depopulate $^3P_2$, tune steady-state lasing	transfer cavity or free-running
$^3P_1$ to $^3S_1$	688	Repump for steady-state lasing	transfer cavity or free-running

Table 3.1: Overview of laser systems

The 461 nm laser system is based on a Toptica DLC. It is locked to the $^1S_0 \rightarrow ^1P_1$ transition in ^{88}Sr using modulation transfer spectroscopy on a Hamamatsu hollow cathode tube. The locked light is used to inject a high power Nichia diode NDB4916,

Function	λ **(nm)**	**Power (mW)**	**Beam diameter (mm)**	$\approx I/I_{sat}$
blue MOT	461	11.4 (in x, y)	20	.1
Zeeman slower	461	18.8	20	.2
red MOT	689	4 (in x, y)	20	300
$^3P_0$ repump	679	5.8	10	1.3
$^3P_2$ repump	707	8.3	10	2
$^3P_1$ repump	688	5	10	1

Table 3.2: Key laser beam parameters. For the blue and red MOT powers, I present the power in each axis parallel to the optical table surface (x, y). We use approximately half of this intensity in the z-direction.

wavelength selected at 461 nm, and placed in a custom laser diode housing. This provides up to around 500 mW of 461 nm light which we distribute across the experiment.

Cooling strontium to μK temperatures requires a laser adressing the $^1S_0 \rightarrow ^3P_1$ intercombination line. To achieve enough power of the narrow-linewidth light required to cool on this transition we inject a set of slave lasers and a tapered amplifier (TA) using light from the stabilized reference laser. This chain provides approximately 150 mW of light out of the TA. The schematic of the beam path of the 689 nm light is illustrated in Fig. 3.17, with a photograph of the actual setup below in Fig. 3.18.

Lastly, we have repump lasers at 679 nm, 688 nm, 707 nm, which are Toptica DL-pro lasers. Each has its own breadboard with optical elements and shutters. The 679 nm and 707 nm lasers were stabilized using a transfer cavity. The 688 nm laser was typically stable enough to be left free-running.

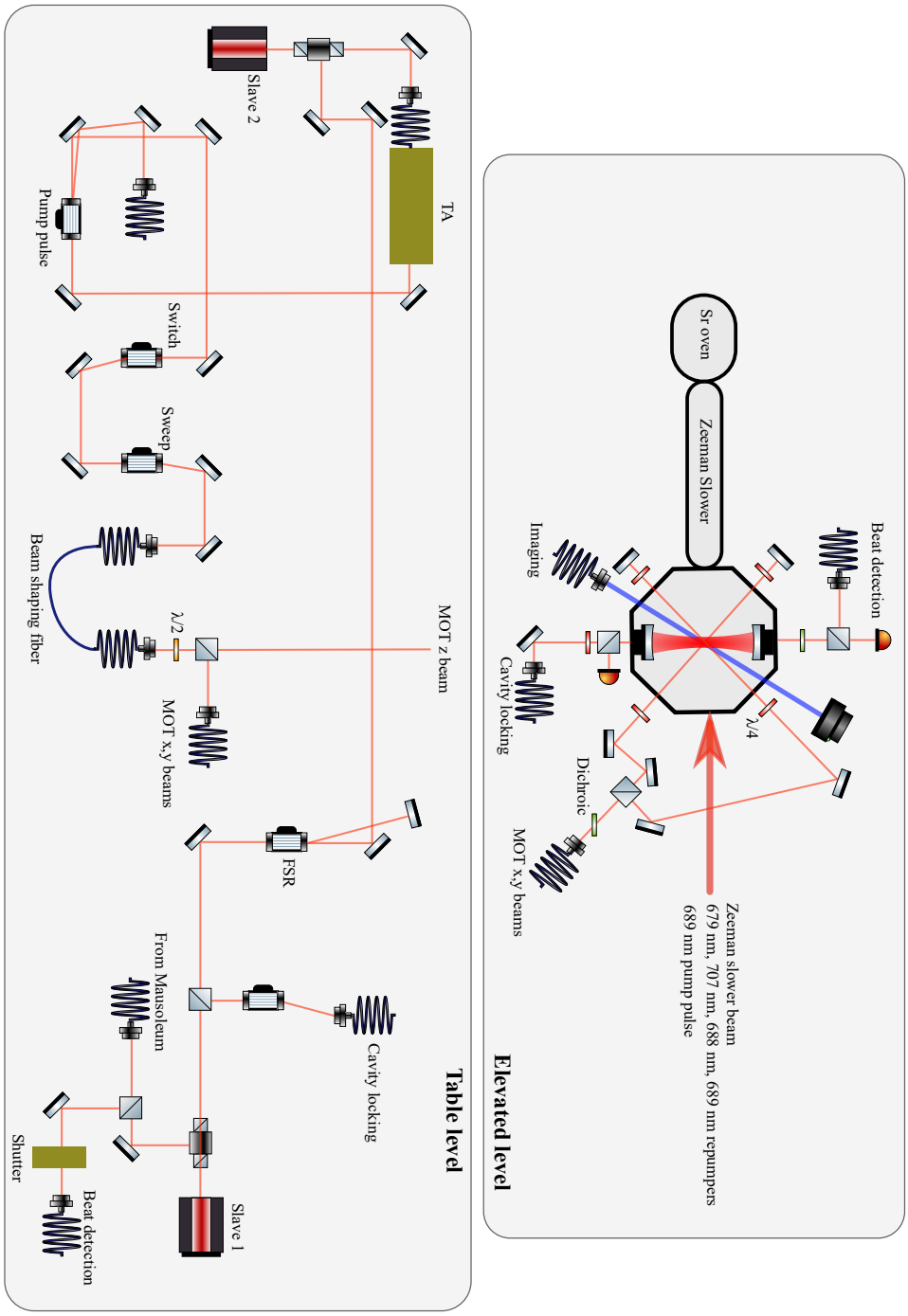

Figure 3.17: Beam path of the 689 nm light. We use the reference laser to inject two slave diodes and a TA to get sufficient power. This light is then fiber coupled to the elevated level on the optical table, where it reaches the atoms. To shift and modulate the light for the relevant spectra needed throughout the cooling, AOMs were placed in the beam path.

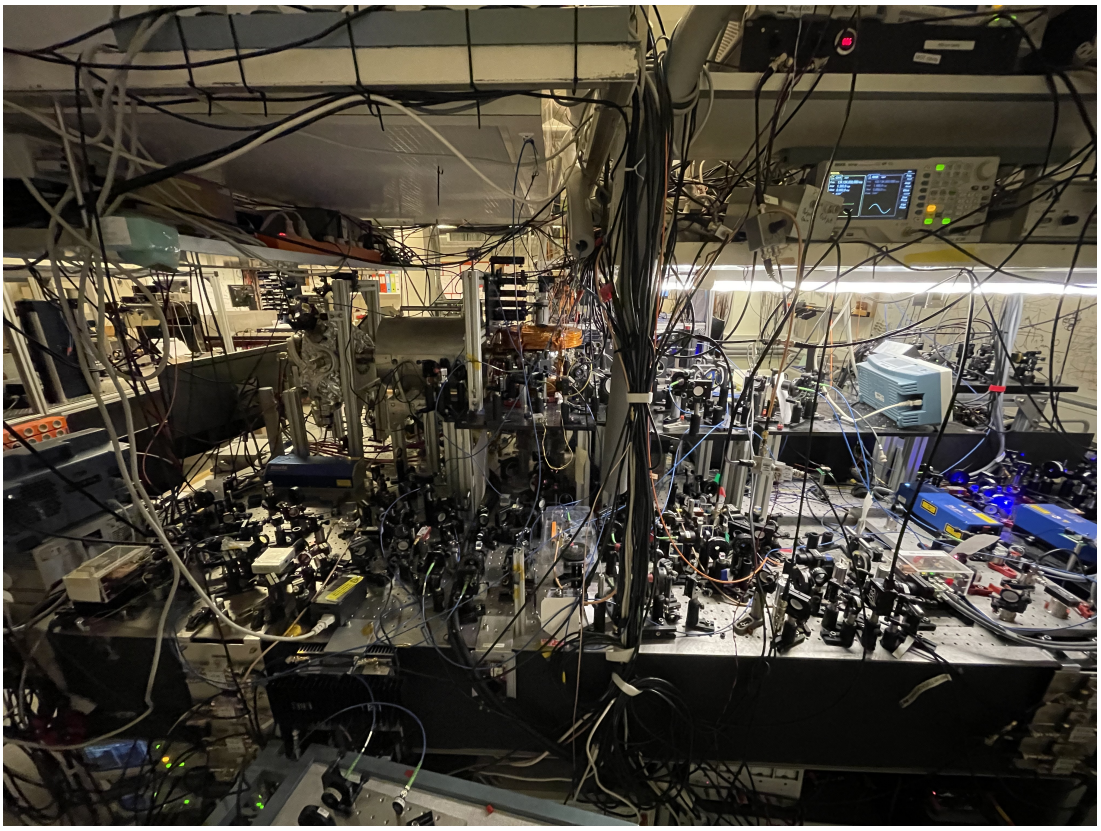

Figure 3.18: The optical table as seen from the side. The table level includes mostly 689 nm optics. Elevated level at the height of the science chamber includes optics for MOTs and repumping.

3.4 Narrow-line cooling and red MOT

Too anyone struggling to get a red MOT, I wanted to share some of our journey and insights to achieve it, because this experimental challenge took a significant amount of time to overcome.

Originally, we utilized the clock laser, the other 689 nm laser, to inject all of our 689 nm lasers in the experiment. This was implemented using a home-built cavity system with a finesse roughly an order of magnitude lower than that of the reference cavity. After the coil switching worked, we began searching for the red MOT, following methodologies found in other literature [46, 69, 78–81]. After the blue MOT, we switched to the red MOT parameters, and then quickly turned back on the blue MOT beams to look at fluorescence. We optimized the red MOT parameters such that the blue fluorescence would not start from zero, but start at a step, signifying the atoms were captured and remained in place due to the red MOT light. With this method, we only ever observed a diffuse red MOT, as seen in Fig. 3.20a.

This led us to investigate the spectral quality of the 689 nm lasers. We noticed that while scanning the 689 nm laser across the science cavity resonance, we observed shoulders as shown in the oscilloscope trace in Fig. 3.19, instead of an anticipated plain Lorentzian. This discrepancy was due to the significant servo bumps on the clock laser. Consequently, we conducted beat tests between the reference laser and the 689 nm at various stages to assess the spectral quality of the beams, specifically the broad-band (BB) and single-frequency (SF) cooling stage light. It was the discovery of these cavity transmission bumps that ultimately led us to inject all of the 689 nm lasers with the reference laser instead of the clock laser.

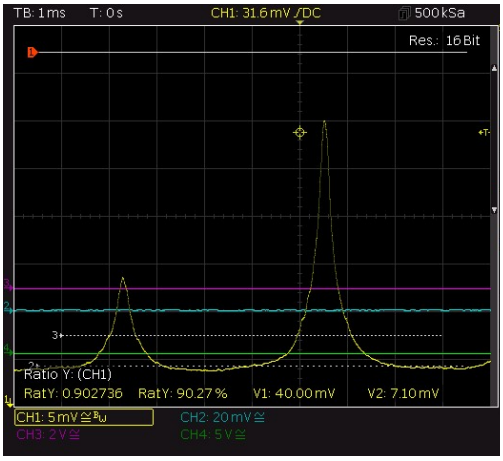

Figure 3.19: Cavity transmission as we scanned the red cooling laser across resonance. There is a sideband because this is the cavity locking light. The shoulders on both these transmission peaks was a telltale sign there was excessive noise on our clock laser.

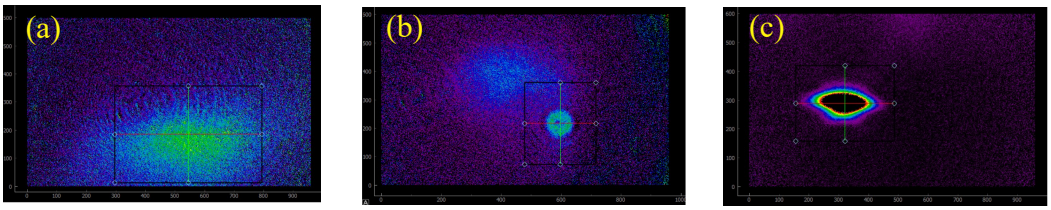

Figure 3.20: Shadow imaging of a red MOT cloud. (a) February 2022: Seeding the 689 nm light with the clock laser resulted in a diffuse red MOT due to noise on the clock laser. (b) March 2022: switching to injection with the reference laser, adjustments to the bias fields yielded a discernible tight circular shape darting across the display—marking the first observation of a proper red MOT. (c) May 2022: After weeks of refining sequences and frequencies, we successfully captured a compact and dense red MOT, trapping tens of millions of atoms at temperatures around 2 μK.

On the first day we implemented this change, as we adjusted the compensation coils, a dense cloud flew across the imaging, which is described in Sec. 3.6.2, as shown in Fig. 3.20b. Once we had this signal, then it was about optimization. The characteristics of our red MOT began to align with descriptions in the literature. For example, the final detuning of the SF MOT resulted in a progressively larger elliptical cloud with increased detunings to the red, revealing a distinct gravitational sag. Moreover, as our SF was tuned to the blue side of atomic resonance, we observed a crystal formation in line with the findings of [81].

The basic sequence we ended up using can be seen below in Fig. 3.21. First we load on the blue MOT, requiring high currents. Once the loading is complete, we step the intensity to about half, lowering the final temperature of the blue MOT and maximizing transfer to the red MOT. Within a couple ms, we have changed the magnetic field, and turned on the BB red cooling light, which is achieved by frequency modulating the light through an AOM. This allows us to simultaneously cool atoms in many overlapping phase-space shells, or velocity classes. We frequency modulate the cooling light at 30 kHz, with a modulation depth of 4 MHz. After operating this for 70 ms, we switch to SF red light and ramp down the intensity, to compress and cool further. We capture about 10% of the blue MOT atoms with the red MOT. Finally we turned off all of the cooling light and had a few ms while the atoms were in free fall and expansion to run the experiments. At a designated time later we sent in imaging pulses for atom number estimation.

We typically capture around 40 million atoms in a shape reminiscent of a pancake, corresponding to a few hundred kHz red detuning, as shown in Fig. 3.22. This atomic cloud distributed across $100 \times 200 \times 200$ μm corresponds to an atomic density of around 1×10^{13} atoms per cm^3.

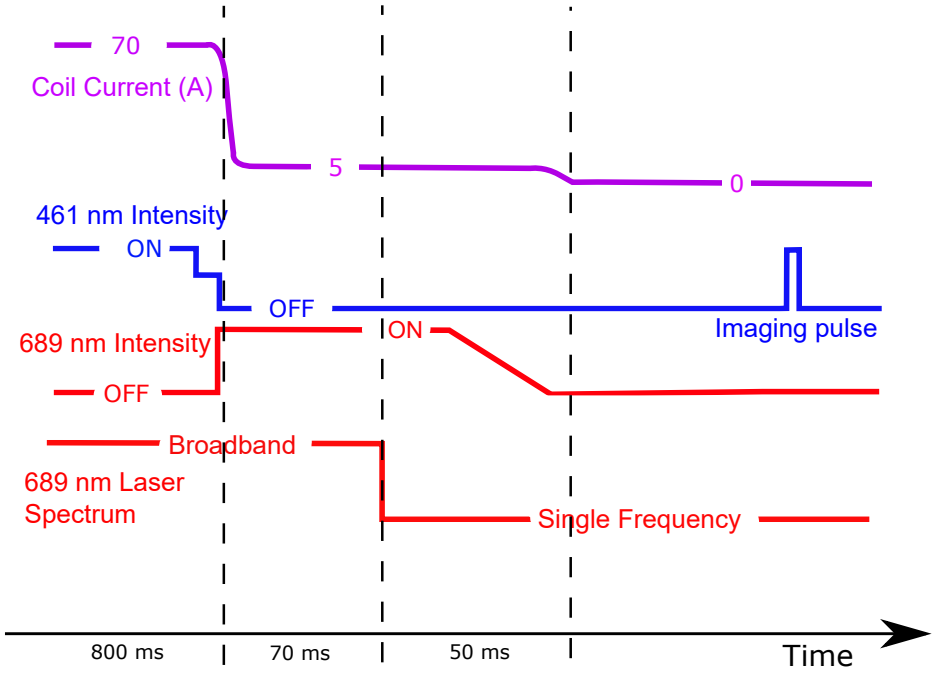

Figure 3.21: The experimental sequence for preparing the atoms with the two-stage MOT. The experiments are conducted after the final black dotted line, once the single frequency red MOT and coils are shut off.

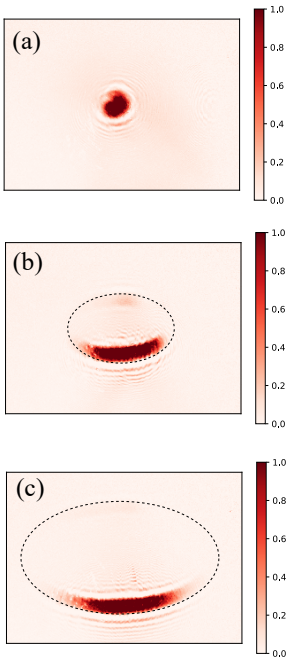

Figure 3.22: Red MOT of 12 million atoms shadow imaged with varying detunings of the single frequency red MOT, $\delta = f_{\text{single frequency}} - f_{\text{atomic resonance}}$. (a) $\delta \approx 0$ kHz. (b) $\delta = -500$ kHz. (c) $\delta = -1$ MHz. Note at this time we had an imaging issue which was causing interference fringes around the MOT.

3.5 Science cavity

The science cavity serves the function of providing a single electromagnetic mode to which the atoms can interact with. Essential parameters related to the cavity are outlined in Table 3.3.

A degradation in finesse was observed since the previous noted values in the group, where the cavity decay rate was reported to be around 620 kHz. We employed a method of scanning a near-resonant laser beam across the cavity resonance in the absence of atoms. This yielded a measured cavity decay rate of 797(2) kHz.

For our experiments, the science cavity was locked using PDH with light detuned by an FSR (781.14 MHz) from the atomic transition. The custom electronics responsible for the locking process were enclosed within a home-built box. The cavity would typically stay locked for hours to days. When the lock disengaged the cavity transmission would decrease to zero. It was beneficial for our data collection to lock the cavity with as little light as possible, so we did not always notice immediately when the lock fell off. Another hint that the lock had fallen off was if the superradiant pulses suddenly became much less consistent.

The lock light an FSR away does not significantly interact with the atoms. We use approximately 3 μW before the science cavity, translating to an intracavity intensity of 1 mW at the cavity mode's waist radius of 450 μm. Assuming this entire 1 mW is incident upon our atomic cloud, which has a conservative size estimate of 100$\times$ 100 μm, the result is an average scattering rate of 0.14 photons per second per atom. Given that our experiments last up to a few milliseconds, this scattering rate from the light an FSR away is negligible and does not impact the superradiant processes compared to other scattering processes in the experiments.

Description	Symbol	Value
linewidth (FWHM)	$\kappa/2\pi$	797(2) kHz
finesse	$\mathcal{F}$	980(2)
length	L	192 mm
free spectral range	FSR/π	781.14 MHz
Mode waist	ω_0	450 μm
Single atom cooperativity	$\mathcal{C}$	4.45×10^{-4}

Table 3.3: Key parameters of the science cavity in our experiment. Single atom cooperativity is assuming maximal coupling.

3.6 Computer control

3.6.1 GUI sequence control

The experimental sequence is orchestrated by a custom-built control system named "QWeather." This system, implemented in Python, comprises both server and client scripts that communicate via a designated broker. At the heart of the experimental setup is an NI6259 card, interfaced with a BNC-2110 terminal block. This has direct

BNC connections to both analog and digital output channels. Specifically, digital output channels manage TTL signals for various AOMs, shutters, and switches. The two analog output channels are responsible for the reference voltages directing the MOT coil currents. Due to a shortage of adequate digital output channels, and for expedited setup, additional actions and timings within the experimental sequence are executed through an elaborate network of RIGOL devices. The GUI is presented in Fig. 3.23.

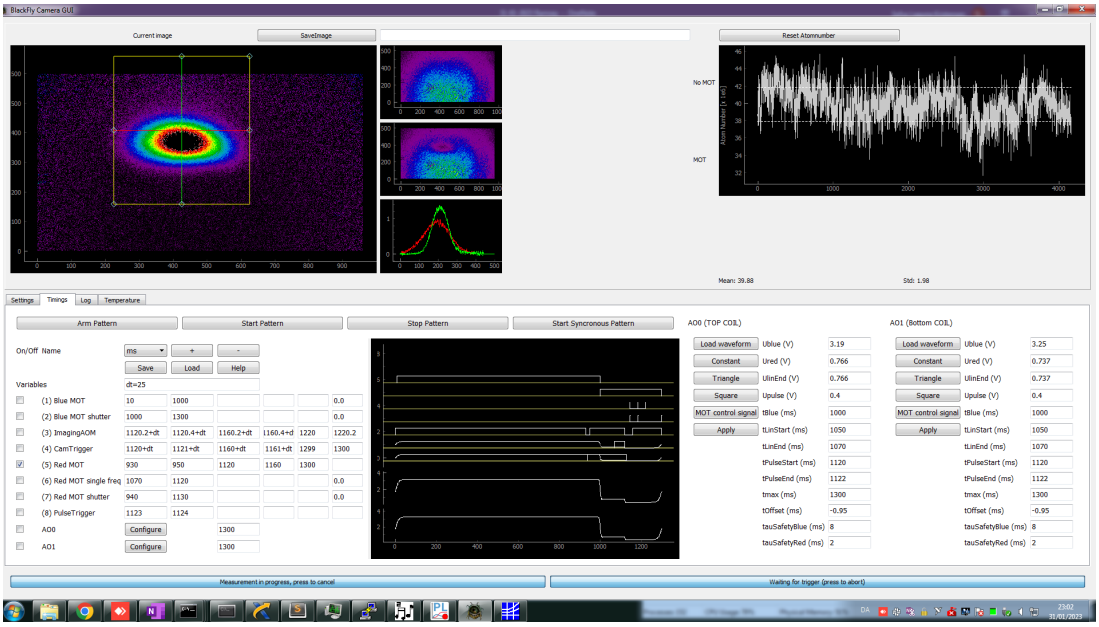

Figure 3.23: CameraGUI used to control the experimental cycle. Top left: OD image of the MOT. Top right: calculated atom number over repeated cycles. Bottom left: timings for the switching of specific signals defining the experimental cycle, with a visual representation in the bottom center. Bottom right: timings and values used for controlling the MOT coil currents.

The control voltage for the MOT coils necessitated several parameters to ensure its smooth operation. Sharp transitions, or 'kinks', in the control voltages frequently induced voltage spikes within the setup. By integrating logistic functions, as exemplified by parameters like "tauSafetyRed", we could mitigate these abrupt transitions. This was crucial in preventing voltage spikes. A detailed account of the control voltage signal design can be found in [70].

3.6.2 Imaging

To image the atoms, estimate atom number, and measure temperature of our MOT, we used a method called absorption, or shadow, imaging. A comprehensive understanding of this method can be found in references [82, 83]. In brief, this approach involves the utilization of a resonant 461 nm imaging beam at low saturation levels. This beam is momentarily flashed to cast a shadow of the atomic cloud onto a CCD array. We take two additional pictures for normalization

purposes. The three images we take are: one with the atom cloud and probe beam on, I_{atoms}, one without atoms and probe beam on, I_{light} and one without atoms and with probe beam off I_{dark}. We calculate the measured optical density (OD) using the equation,

$$\mathrm{OD}_{\mathrm{meas}} = \ln\left(\frac{I_{\mathrm{light}} - I_{\mathrm{dark}}}{I_{\mathrm{atoms}} - I_{\mathrm{dark}}}\right) \tag{3.9}$$

We employ a 2f imaging setup, with a 20 cm focal length lens. The distance from the lens to the atomic cloud and from the lens to the CCD Backfly camera (BFLY-U3-23S6M-C) were both 40 cm. The resulting image is inverted with magnification of 1. The GUI also includes triggers for the imaging.

By integrating the column densities across all of the pixels, we can estimate the atom number in the MOT. If the OD of the atomic cloud is too high, then no photons will reach the CCD camera in this area. When this happens, the center of the cloud no longer resembles a Guassian, but a flat top, leading to an underestimation of our atom number. For our high red MOT atom numbers we typically employ a time of flight (TOF) of at least 20 ms before imaging for a more precise atom number estimation.

By fitting Gaussian functions to absorption images separated by a TOF, t_F, we can calculate temperature, T, of the cloud,

$$T = \frac{m}{4k_B t_F^2}(R_F^2 - r^2) \tag{3.10}$$

where $R_F(r)$ is the original $1/e^2$ radius of the cloud. Typical TOF times are 20 - 35 ms.

3.6.3 Data acquisition

Data acquisition was executed using the R&S RTB2004 oscilloscope. We developed an experimental script that acquired single traces, storing them in the 'f' bit format and then transferring them to a harddrive via ethernet. This method proved substantially faster than saving via CSV files.

Choosing the resolution of the scope was also important if we wanted to capture data at a high rate. When measuring with the heterodyne beat note, our results centered around 42 MHz. This frequency corresponds to the detuning of the reference laser from the $^1\mathrm{S}_0 \rightarrow {}^3\mathrm{P}_1$ atomic transition. According to the Nyquist theorem, identifying frequencies up to 42 MHz necessitates a sampling rate of at least twice the frequency, or 84 MHz. To play it safe, we ensured our data was acquired at a rate exceeding 90 MHz, equivalent to a data point approximately every 10 ns in the time domain. Depending on the length of the saved traces, which ranged from 100 μs to several ms, and how many channels we were saving, the duration required to retrieve these data sets varied. Given that our experimental sequence lasted about 1.4 s, if data retrieval exceeded this duration, we would not be able to capture the measurement every experimental cycle.

CHAPTER 4

Collective strong coupling regime and superradiant pulses

The results presented in this section are in support of previous literature and provide vital insight into our system, setting the foundation for the work published in chapters 5 and 6. Among the key steps was confirming that our system lies in the collective strong coupling regime. We do this by measuring the normal mode splitting. Later in the chapter we discuss superradiant pulses on a red MOT and look at characteristics of these pulses.

4.1 Collective strong coupling regime

To verify that the system is in the collective strong coupling regime, and also gauge the number of atoms effectively coupled to the cavity mode, we measure the size of the normal mode splitting, which is equal to the collective vacuum Rabi frequency Ω_N. The collective strong coupling regime is achieved if $\Omega_N \gg \kappa, \gamma$.

To measure the dressed atom-cavity mode frequencies, we apply a phase modulation to the cavity locking light at the FSR frequency of 781.14 MHz, producing a frequency component close to atomic resonance. To avoid potentially light shifting the transition from having a singly detuned frequency, we form dual probes at frequencies $\omega_{p\pm}$ by amplitude modulating the cavity light. We ramp the amplitude modulation frequency ω_m from 0 to 5 MHz, crossing over both resonances simultaneously in a few hundred μs, ensuring that the atom-cavity coupling remains largely the same in this short interval.

We measure the transmitted power at the dressed cavity modes via a heterodyne beatnote detection with a stable reference laser approximately 40 MHz away. In Fig. 4.1a we plot a spectrogram of the beat signal as we scan across the two normal modes simultaneously. Figure 4.1b displays the power spectral density (PSD) of the beat data, and by fitting two Lorentzians, we derive the separation between them as $\Omega_N = 6.32(1)$ MHz. Clearly we are in the collective strong coupling regime. We note the difference in amplitudes of the normal mode resonances is due to a mixer which was operating near its edge of its frequency range.

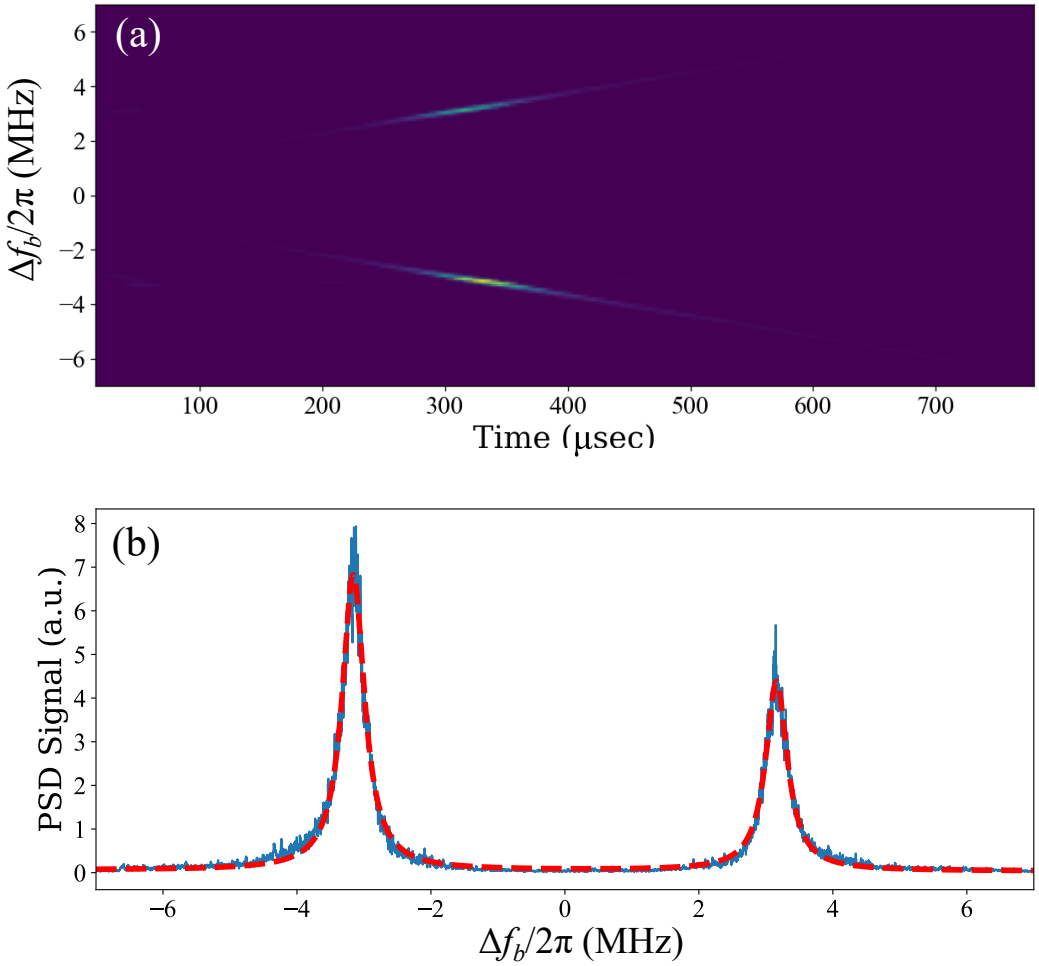

Figure 4.1: (a) Spectrogram of a heterodyne beatnote measurement as we scan two probe frequencies across the normal modes and overlap the transmitted light with a reference laser. The spectrogram is using overlapping windows of 30 μs. (b) PSD of the entire beat data. We fit two Lorentzians to find the distance between them, which is $\Omega_N = 6.32(1)$ MHz. The height difference is attributed to a mixer operating near the edge of its frequency range.

Since our atoms are not held against gravity by any forces during the experiments, the atoms fall through the cavity mode. To estimate how much time we have to do experiments while still in the collective strong coupling regime, we left the probe frequencies sweeping and recorded the normal mode splitting throughout the time after we released the atoms. A spectrogram of an example trace which measures the normal mode resonances eight times is shown in Fig. 4.2a. In Fig. 4.2b we extracted all of the normal mode splittings and plotted them over time. Data points of the same color were taken within one experimental cycle. The dotted lines serve as time references for orientation within the cycle. This shows that we release the atoms slightly above the cavity mode, leading to the slight increase in

the normal mode splitting after we stop cooling on the red MOT. This gives us time to shut off the light and magnetic field. Then we excite the atoms with pump light (or repump light) at time $T = 0$ s on the x-axis. This measurement indicates that we have approximately 5 ms available for conducting experiments.

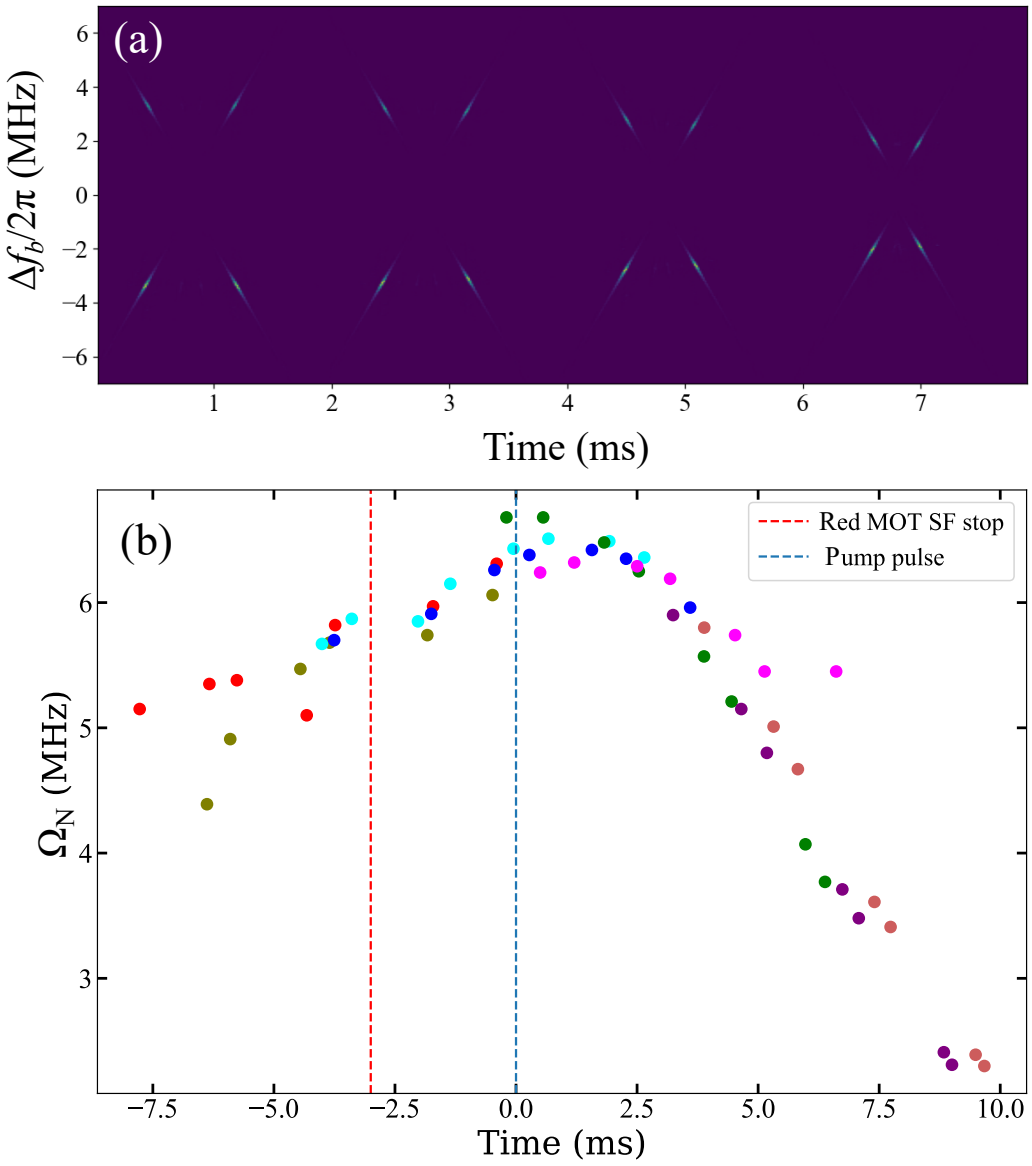

Figure 4.2: (a) Spectrogram of a beatnote measurement with a reference laser as we scan two probe frequencies across the normal modes over the course of time which we run the experiments. The spectrogram is constructed using overlapping windows of 30 μs. We observe the normal mode splitting decrease as the atoms are falling out of the cavity mode. (b) After fitting each pair of Lorentzians, we have numerous normal mode splitting measurements. Plotting these points over time we can gauge how our atomic cloud couples to the cavity after the red MOT light shuts off.

When the cavity is on resonance, the atomic absorption deteriorates the cavity finesse, leading to diminished intracavity power [84]. As the laser's detuning from resonance increases, the atomic influence shifts from eroding the cavity finesse to solely shifting its resonance frequency. This behavior arises from the atomic dispersion, where the real component of atomic polarizability diminishes at a slower rate than its imaginary counterpart for further detunings. Measuring these shifts in cavity resonance offer potential applications in atom and atomic-state detection, and also in the generation of squeezed states [85].

When detuning the empty cavity resonant frequency, the two transmission peaks display the expected avoided-crossing behavior, $\omega_{\pm} = \left(\delta_c \pm \sqrt{\delta_c^2 + \Omega^2}\right)/2$ [63], as shown in Fig. 4.3. Furthermore, the widths seem to follow the weighted average of the atomic and bare-cavity linewidths [86]. The mode closer to atomic resonance exhibits a linewidth closer to Γ, while the mode further away from atomic resonance is more cavity-like, and has a resonance closer in width to κ. The latter is most useful for non-destructive atom counting. While both modes are affected dispersively by atom number, the mode further away from atomic resonance scatters fewer atoms during the probing.

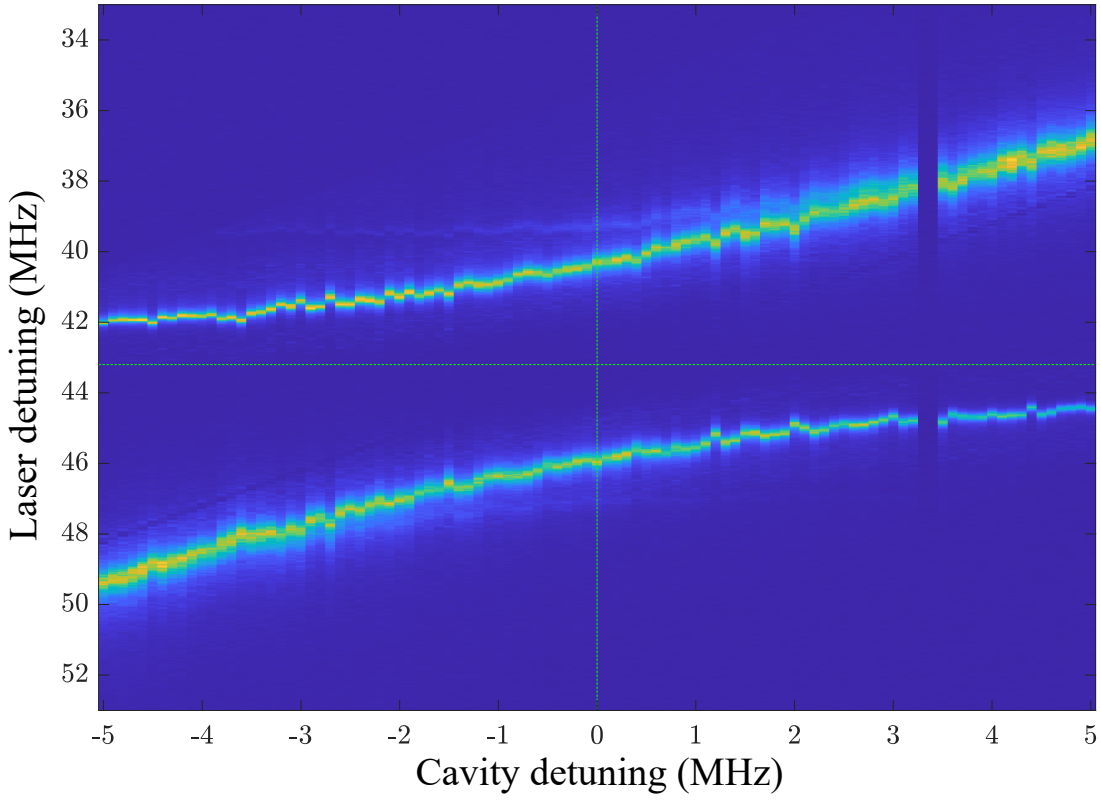

Figure 4.3: Measured normal-modes via beat detection for varying cavity detunings. We see the expected avoided-crossing behavior. The vertical dotted green line indicates the cavity resonance, while the horizontal indicates when the laser is on resonance with the atomic transition.

4.2 Superradiant pulses

Next, we apply transverse excitation pulses to invert the atomic ensemble and observe the cavity output power as we vary the cavity detuning. We calibrated the pump pulse duration to maximize the superradiant pulses when the cavity was on-resonance, given our specific power and beam profile. The optimal duration was determined to be 1030 ns with a power of 18(2) mW and a Gaussian beam waist of 3.0(1) mm. In Fig. 4.4a, we plot the time evolution of the output power. Each time trace is aligned so the peak is at $t = 0$ μs, and is the average of 20 trials. To minimize systematic errors during data collection, the sequence of cavity detunings was randomized. The detunings with darker backgrounds, at for example 0.3, -0.8, -1.2, -3.3 MHz, were sets taken while the cavity had fallen off lock. Since we recorded the pulses using the same DC detector that measured the transmission of the cavity locking light (FSR away), this resulted in a reduced background for these specific detunings. Figure 4.4b represents the mean and standard deviations of the time delay to the peak emissions.

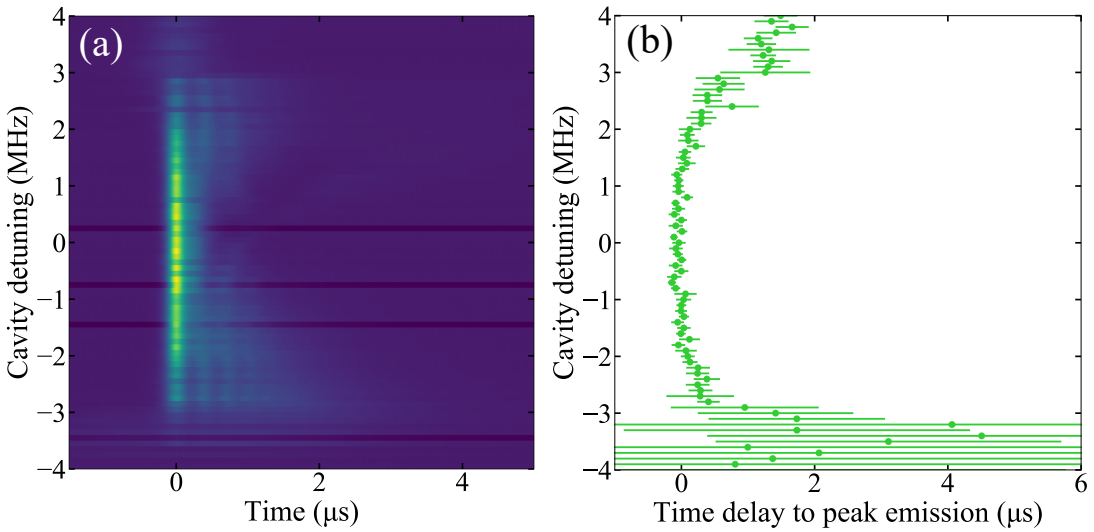

Figure 4.4: (a) Cavity output power over time for various cavity detunings. Each time trace is aligned such that the peak emission is at $t = 0$ μs. Each horizontal color line is an average of 20 trials. Detunings were chosen in random order to reduce systematics while datataking. The few darker lines are sets taken while the cavity had fallen off lock. (b) Mean and standard deviations of the time delays to the peak emissions. (Data taken: 04-05-2022)

The emitted pulses in a detuned cavity exhibit peak intensities reaching up to 5 μW, followed by rapid oscillations at a frequency of about 2 MHz. These oscillations are more evident for larger cavity detunings and can be attributed to a phenomenon similar to off-resonant Rabi oscillations. Unlike the resonant case, where a fully inverted sample rapidly decays to the ground state, pulses emitted in a detuned cavity have lower peak intensities and sustained emission, lasting several microseconds. The population starts inverted, however, because of the detuned

drive frequency, the atomic population oscillates at a higher rate, never reaching full excitation again. This leads to oscillations and a slower decay of emitted intensity compared to the resonant drive case.

Figure 4.5 presents single-shot traces of pulses within both a resonant (blue trace) and a 2.5 MHz detuned cavity (red trace). The onset of the pulse with the cavity on resonance closely resembles the hyperbolic secant shape as anticipated [59]. However, the latter half of the pulse does not maintain this shape, resembling more of an exponential decay that aligns with the cavity's decay rate, superimposed with slight oscillations. This suggests that once the cavity's intensity has built up, emission decay cannot exceed the inherent cavity decay rate.

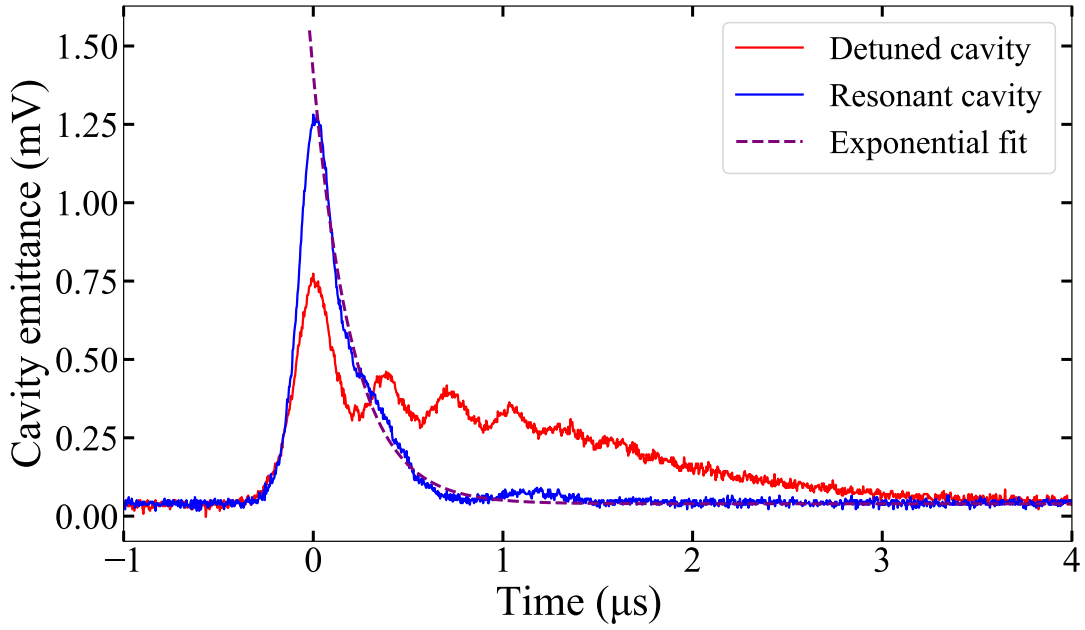

Figure 4.5: Superradiant pulses for a resonant cavity (blue) and cavity with a detuning of 2.5 MHz (red). We see that both are not hyperbolic secant pulses but have some intricate dynamics, with the detuned case having much more prominent and long lasting oscillations. The purple dotted line represents a best-fit exponential decay from the peak of the resonant case, yielding a lifetime of 208 ns, corresponding to a κ of 765 kHz.

Additionally, several factors could contribute to the dephasing of the atoms throughout the pulse, causing the intensity to deviate from the expected pulse shape. Temperature is not expected to have significant influence on this time scale. With atoms at only a few recoils in temperature, we estimate an average displacement of an atom during a microsecond pulse to be in the tens of nanometers. This is considerably smaller than the 689/2 nm node spacing of the lattice.

Another possible contribution to the latter part of the pulse shape comes from the atoms having variable couplings g within the cavity. As the cavity field builds up, atoms positioned differently with respect to the cavity's nodes and antinodes experience different Rabi frequency drives. This spatial variability can lead to a

spread of emission rates across atoms — some emitting more rapidly than others. Such disparities can introduce decoherence as the pulse progresses. For a more comprehensive comparison with simulation, I refer to the work by Tang [70].

4.3 Investigation of pulse attributes

In chapter 5, we use superradiant pulses as a direct readout of the excited state population. Shot-to-shot fluctuations of the pulses for the same atomic inversion would lead to noise in our measurements, ultimately degrading the feedback signal for potential use in a clock or sensor. For this reason we investigate correlations between attributes, such as the peak amplitude, delay to peak, and atom number. To enhance the data acquisition rate, we consider conducting a sequence of ten excitations with superradiant readout within a single MOT cycle. Each excitation is interspaced by a 100 μs interval—corresponding to five natural lifetimes—ensuring ample time for any lingering atoms in the excited state to undergo decay.

In Fig. 4.6, we analyze the peak and delay times across 30 repeated trials executed on the same MOT cloud to look for any discernible patterns or systematic behaviors. An example trace is provided in Fig. 4.6a for reference. Figure 4.6b is a scatter plot of peak amplitude versus delay for all 300 sequences (comprising ten pulses per MOT cycle over 30 cycles), with colors indicating a specific pulse index out of the set of ten. No obvious systematic trends are observed from this data. Figures 4.6c and d show that peak amplitude and delay time are consistent within error bars throughout the ten pulses.

We know that with each sequence, the atoms experience a recoil from one photon in the pump direction and one from the cavity emission. By the tenth sequence, the atoms will have accelerated to approximately 65 mm/s in a direction transverse to the cavity axis. The resultant displacement of the atoms is roughly 32 μm in this time, assuming a constant acceleration up to 65 mm/s. Given that this is significantly smaller than the cavity mode waist radius, which is 450 μm, there would not be an appreciable change in the cavity coupling during these ten pulses.

Next we investigate superradiant pulses after two different excitation angles on the Bloch sphere. In particular we look for correlations between peak amplitude, pulse area, delay to peak, and delay to 50% area emitted. At the time these were the most obvious attributes to characterize the pulses by.

In Fig. 4.7 we conducted 200 pulses after π-pulse excitations, while in Fig. 4.8 we did the same for $2\pi/3$-pulse excitations. In both, we find strong correlations between peak amplitudes and pulse areas, as well as between delay to peak and delay to 50% area emitted. In chapter 5, for simplicity, we choose to use peak amplitude as a measure of excited state population. Given more time, we would work towards using a combination of peak emission and delay to peak which could give us a more precise reading of the excited state population.

The differences in fluctuations observed between the $2\pi/3$-pulse and the π-pulse excitations we primarily attribute to two factors. The first factor involves the mode competition between the pump direction and the cavity emission direction. As evident in a collective Bloch sphere representation, when the Bloch vector is closer

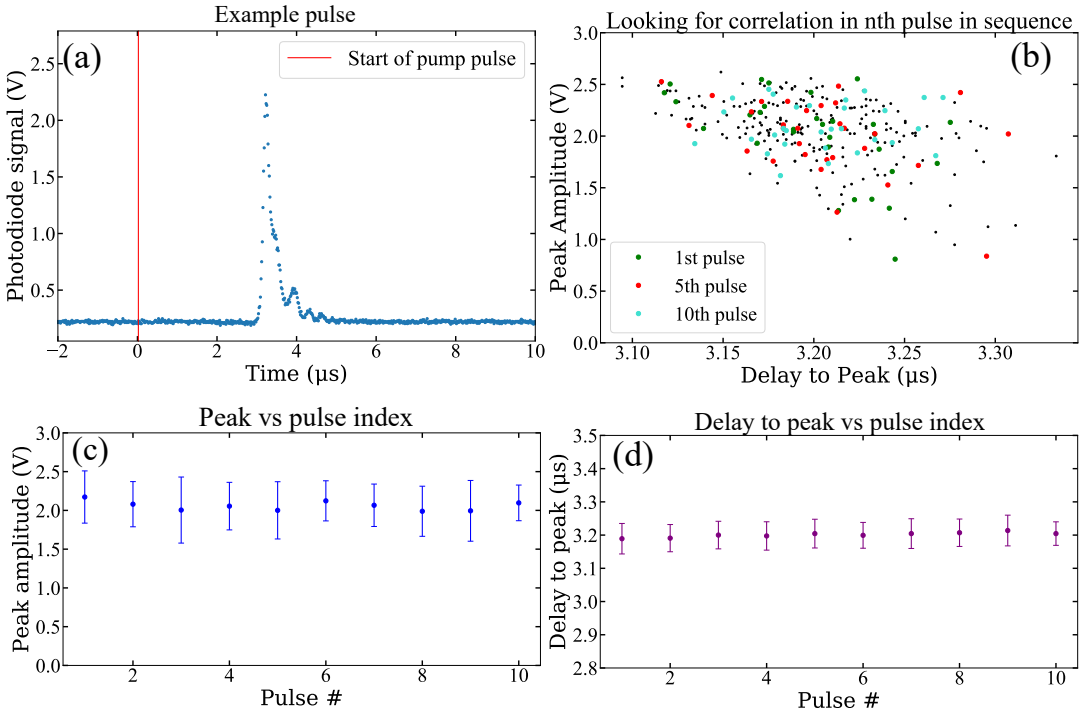

Figure 4.6: Ten $\pi-$pulse excitations followed by superradiant readouts within a single MOT cycle. (a) A representative trace indicating the time of the pump pulse (marked by the red line) followed by the superradiant emission. (b) Scatter plot of the peak amplitude and delay to peak over 30 distinct MOT loading cycles, encompassing a total of 300 sequences. We use color and slightly bigger markers to identify the 1st, 5th, and 10th pulses to look for systematic trends. (c) and (d) Mean values for the peak and delay to peak of each pulse index, respectively, with error bars signifying the standard deviation across the 30 MOT cycles. (Data captured with 40 million atoms on 16-09-2022)

to the equator, the atomic dipoles have a more correlated phase pattern. The atoms will preferably emit along the direction with this phase pattern than in a direction without one. This leads to faster emission compared to a collective Bloch vector starting at the north pole, with no defined phase. Rapid decay occurs until the cavity emission builds up and out-competes the emission along the pump direction. This mode competition can lead to some of the observed weaker cavity-emitted pulses in Fig. 4.6b.

The second factor can be attributed to fluctuations in the excitation. Peak emissions appear to be especially sensitive to fluctuations in excitation closer to the equator of the collective Bloch sphere. This can be observed by the significantly larger spread of data points in the scatter plots in Fig. 4.8 compared to the corresponding ones in Fig. 4.7. When the collective Bloch vector is positioned near the north pole, these fluctuations tend to be more subdued, leading to smaller variations in the emitted pulse strength. This difference in sensitivity depending on the position of the collective Bloch vector is illustrated in Fig. 4.9, with blue dashed lines representing possible variations of pulse sizes for a variation in

excitation of ±5%. Together, these two factors—mode competition and excitation fluctuations—play a significant role in the differences we observe in the pulse attributes between the two types of excitation pulses.

If we had more time it could be fruitful to investigate the effects from seeding the pulses, sending some resonant light through the cavity immediately after the excitation to initiate the emission along the cavity. Perhaps this forced, rapid start to the cavity emission would leave less time for the mode competition described above. However, our exploration was constrained by time.

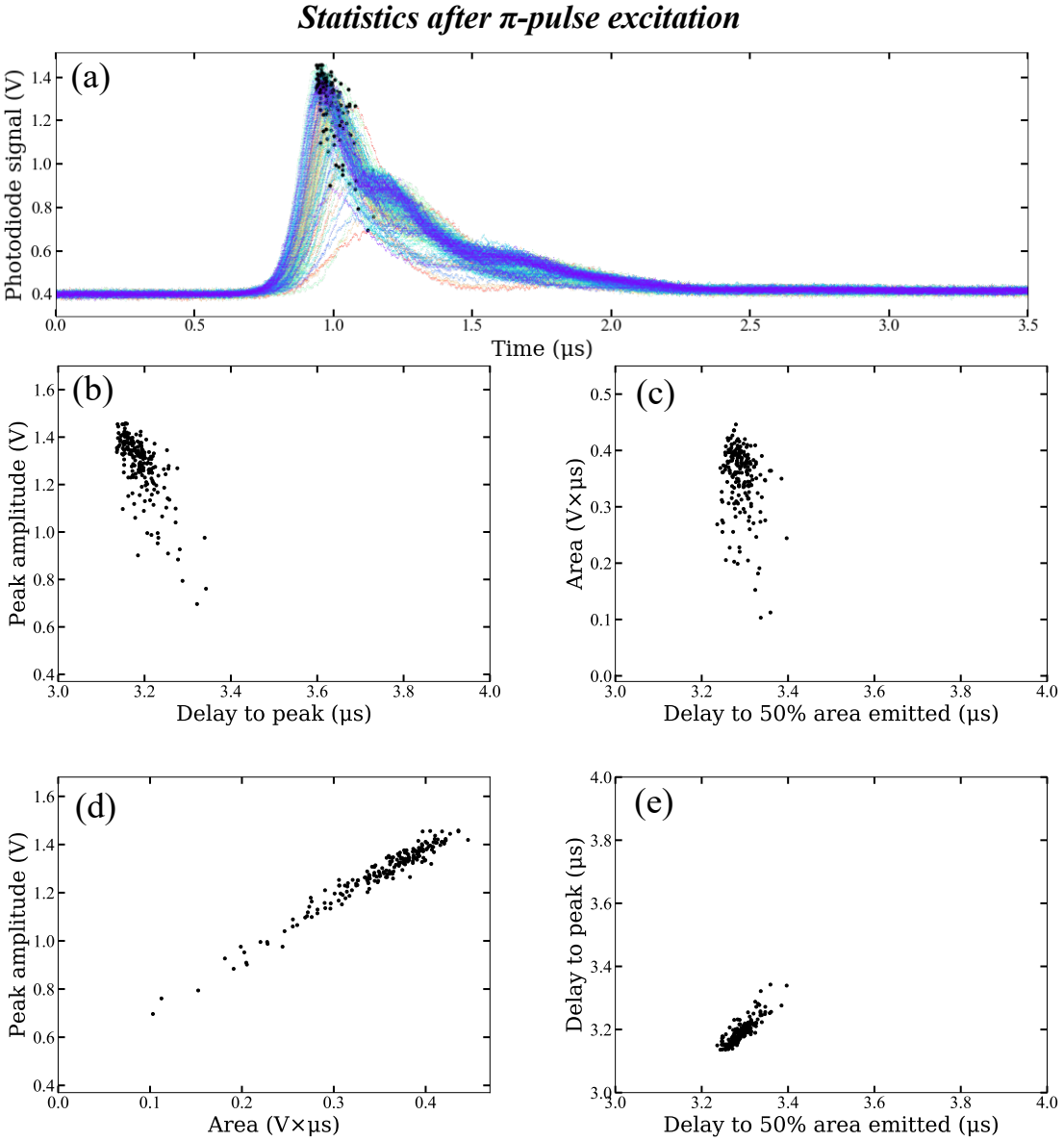

Figure 4.7: Investigating superradiant pulse attributes and statistics when the atoms are excited with a π-pulse. (a) 200 superradiant pulses superimposed with black markers at peak emissions. The four plots below (b) - (e) are comparisons of pulse attributes: peak emission, area, delay to peak, and delay to 50% of the area emitted. We note strong correlation $\approx .97$ for peak emission and area, and a similarly strong correlation for time delays. Peak emission vs. delay to peak scatter plot had a correlation of about 0.6. (Data taken 08-09-2022)

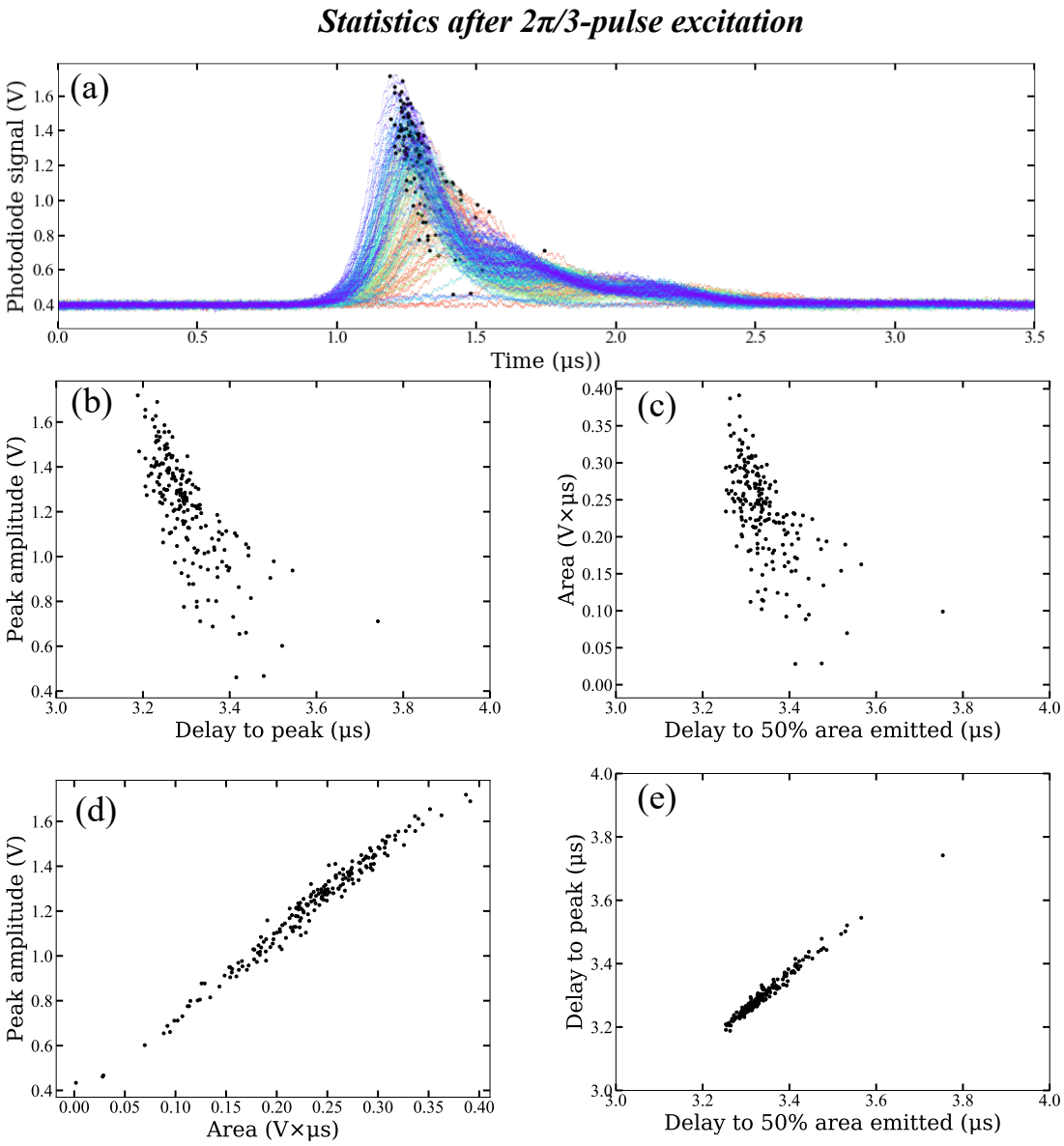

Figure 4.8: Investigating superradiant pulse attributes and statistics when the atoms are excited with a $2\pi/3$-pulse, with similar comparisons as in Fig. 4.7. We note overall wider spread and variation of the pulses compared to those after a π-pulse excitation in Fig. 4.7a. (Data taken 08-09-2022)

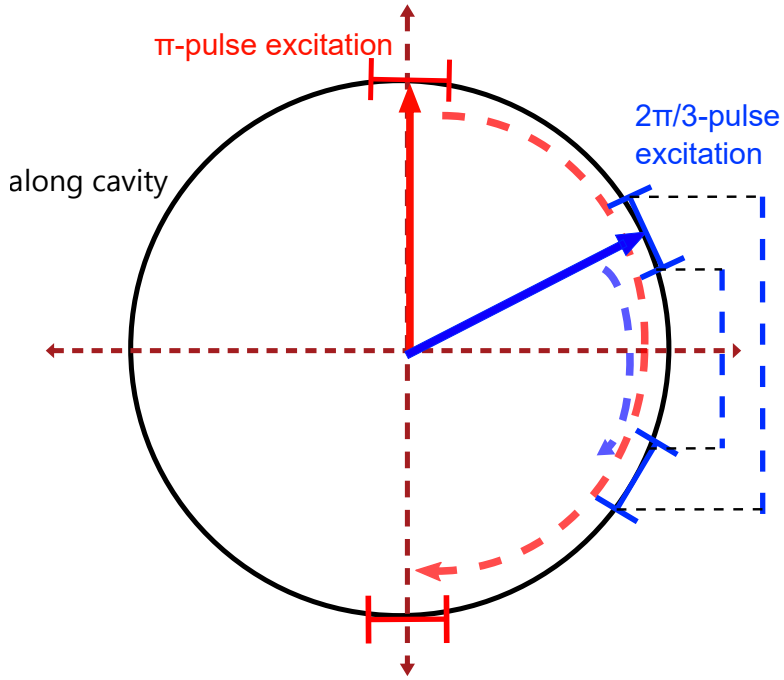

Figure 4.9: Collective Bloch sphere along cavity mode post-transverse excitation. The diagram highlights how a variation in excitation can lead to greater differences in pulse attributes for a $2\pi/3$-pulse than for a π-pulse. Error bars indicate an approximate $\pm 5\%$ uncertainty in excitation. Blue dotted lines on the right demonstrate possible variation in pulse height from the uncertainties in the $2\pi/3$-pulse excitation.

CHAPTER 5

Collectively enhanced Ramsey readout

5.1 Introduction

In a usual atomic clock scheme atoms must be cooled and trapped to prepare them for interrogation. During the interrogation phase, radiation from the reference laser is applied to the atoms, either in a Rabi excitation with a single laser pulse, or a Ramsey excitation with two pulses separated by a dark interval.

Traditionally, the atomic population is determined after an excitation attempt by applying a different laser on a spectrally broad transition that shares the lower state with the clock transition. This allows many photons to be scattered per atom, which fluoresce into 4π. These population measurements can be converted into an error signal to tune the reference laser frequency to atomic resonance. However, this detection method heats up the atoms beyond recapture and a completely new atomic ensemble must be cooled and trapped before another interrogation attempt can be made.

Since the loading and cooling phase takes a significant fraction of the total cycle time, reusing the same cold atoms would permit a faster sequence of interrogations, thereby reducing the averaging time to acquire a given frequency stability. One possibility is to implement a dispersive measurement of the atomic population in order to detect the atomic state not via absorption but via dispersion as a phase shift induced on a weak off-resonant laser beam [87].

The method introduced in this section is even simpler. We use the photons directly from the long-lived states of the clock interrogation by harnessing superradiance, making emission fast and directed.

Here we explore the theoretically predicted threshold for superradiant emission on the kHz transition when exciting atoms transversely to the cavity axis as theoretically predicted in [88]. This feature can be leveraged in a Ramsey sequence with a superradiant readout in which the first $\pi/2$-pulse places the atoms into a state which is subradiant and protected from collective cavity decay. The second $\pi/2$ pulse projects the phase accumulated during the dark evolution time onto the z-axis of the collective Bloch sphere, as illustrated in Fig. 5.1. This results in a fast

and directed emission into the cavity mode related to the amount of population inversion.

When this theoretical proposal was published by the group of Helmut Ritsch, it seemed perfectly in line with what our experimental system was capable of. We could quickly see a resemblance to the superradiant-enhanced Ramsey spectrum as predicted in their paper [88]. This led to a close collaboration on a manuscript with Christoph Hotter and Helmut Ritsch. This chapter presents work from our joint manuscript [89], which is currently under consideration.

5.2 Experimental system

The experimental setup is very similar to the one used for generating the pulses mentioned in the previous chapter. Up to $N = 4 \times 10^7$ ^{88}Sr atoms are cooled down to 2 μK and centered within the fundamental mode of the science cavity, as depicted in Fig. 5.1a. This cavity is tuned to atomic resonance using light which is detuned an FSR away. We optimize the bias fields and sequence for the largest π-pulses achievable with our transverse excitation. This corresponded for us to a magnetic field $B = 0.2$ mT such that each of the $m_j = \pm 1$ Zeeman sublevels of $^3P_1$ were split by $\Delta = 2\pi \times 4.2$ MHz. The polarization of the pump was chosen to be vertical to align with the bias field. A CODIXX polarizer plate was used to clean the polarization and a $\lambda/2$ plate to tune it.

The atoms are driven by a laser operating at frequency ω_l, detuning $\delta_a = \omega_l - \omega_a$, and Rabi frequency denoted by $\Omega = 2\pi \times (833 \pm 30)$ kHz. Given the pump laser's waist size exceeding greatly the size of the atomic cloud, and inverse pump duration exceeding the Doppler width of the cooled sample, we assume a uniform Rabi frequency across the sample. The emitted power of the pulses are detected on an APD via a heterodyne beat measurement with a stable local oscillator (LO) to reject the cavity locking signal.

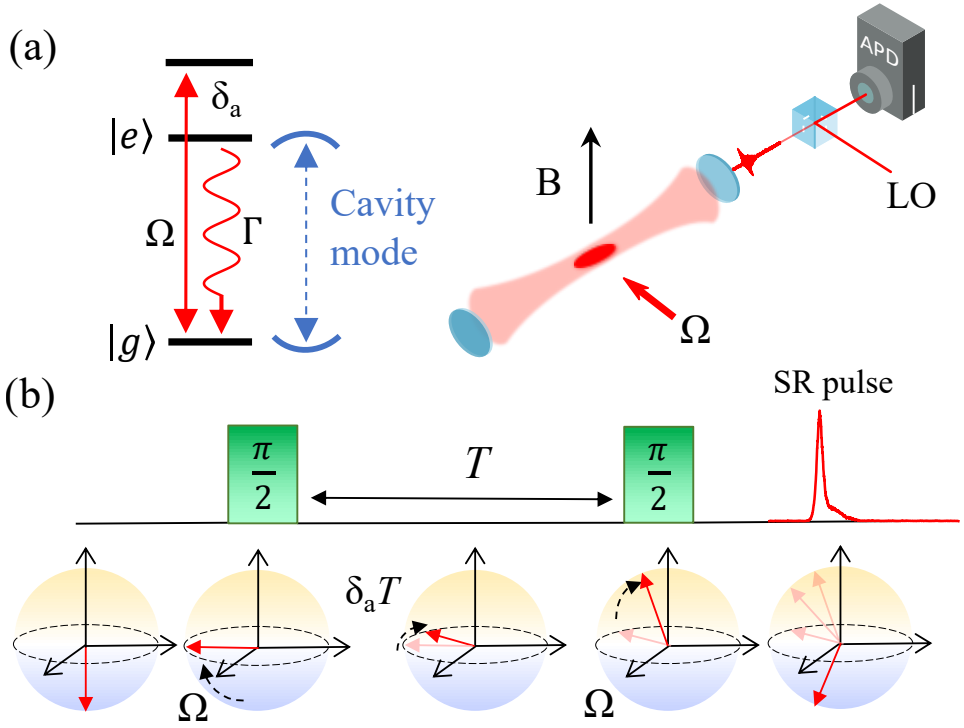

Figure 5.1: (a) Level structure and experimental system. Strontium atoms are cooled in the center of the cavity and pumped at detuning, δ_a, from the $^1S_0 \rightarrow {}^3P_1$, $m_j = 0$, 689 nm transition transversely to the cavity axis. We observe the emitted pulse via a beat detection with a local oscillator. (b) Ramsey interrogation sequence diagram. The atoms are pumped by two $\pi/2$-pulses separated by a free evolution time T. Below the sequence we represent the collective Bloch vectors at corresponding times. When positive inversion is achieved, a superradiant pulse is emitted. This is represented by a collective Bloch vector that accelerates downward on the rightmost Bloch sphere. Both its peak intensity and photon count are indicative of the magnitude of the (initial) positive inversion. This figure is adapted from [89].

5.3 Cavity sub- to superradiant threshold

To verify the theory of [88] we examined the emitted intensity and photon number after exciting the atomic cloud for varying durations of single pulses, corresponding to varying angular excitation on the Bloch sphere. For this investigation we lowered the atom number to $N = 2 \times 10^7$. This way the superradiant pulses started after the excitation pulse was complete and made the dynamics simpler. Figure 5.2a shows a sample trace of an excitation pulse recorded on an oscilloscope (and also superradiant pulse). Here, t_{peak} designates the time delay from the end of the pump pulse to the peak of the superradiantly emitted intensity, circled in blue.

In Fig. 5.2b we plot normalized peak intensity (blue) and normalized area under the pulse (red) for varying excitation pulse duration. We plot on the x-axis

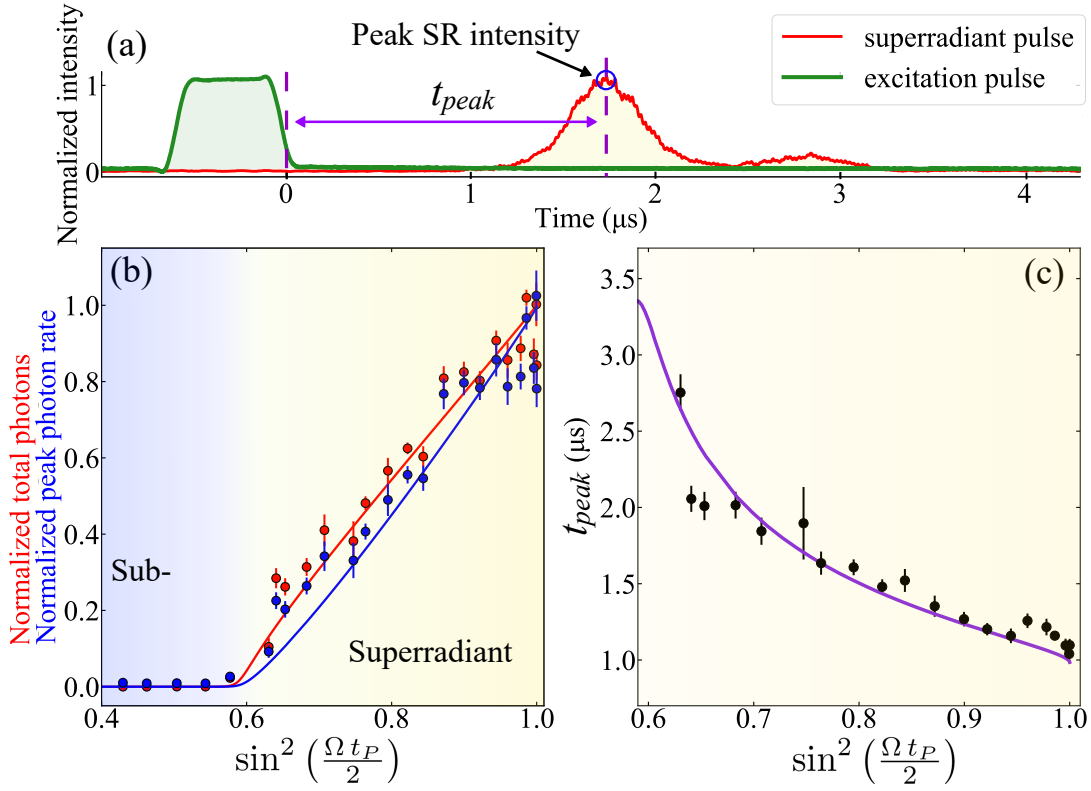

Figure 5.2: (a) Example data trace showing the excitation pulse (green), pulse delay time (purple), and detected superradiant light pulse (red). Peak emitted intensity is circled in blue. (b) Normalized emitted pulse area (red) and peak amplitude (blue) for varying excitation pulse duration. We observe a threshold at $\Omega\, t_P = 0.57\pi$ for superradiant pulses to occur. Solid lines are simulations based on the experimental parameters. (c) Delay time data for varying excitation angles. The solid purple line is a simulation treating g as a free parameter. Data points in (b) and (c) are averages of ten measurements with error bars represented by the standard deviation of the mean. Figure adapted from [89] (Data taken 22-11-2023)

$\sin^2\left(\frac{\Omega t_P}{2}\right)$ as a proxy for the excitation right after a pump pulse, $\langle\sigma^{22}\rangle_{t=0}$. While the two should theoretically be equal, the population never reaches 100% excitation due to decoherence in the system during the pump pulse. This could be due to spontaneous emission, Doppler dephasing, and potentially noise on the pump laser. A π-pulse is determined as the pump pulse duration resulting in the largest peak superradiant emission. Near the π-pulse, which are the points on the far right, we see slight deviations from the theory. These deviations are due to variations in the pumping efficiency and are skewed towards lower pulse peaks and areas. Any deviations in the π-pulse excitation would lead to a slightly lower inversion.

Solid lines are simulations by Christoph Hotter for our experimental parameters. As explained in chapter 4, the reason why this curve is linear with excited state population above threshold, and not the N^2 as is characteristic in traditional superradiance, is due to the particular regime we are in. Our collective interaction is greater than the cavity decay rate, $2g\sqrt{N} > \kappa$, where g is the single atom-cavity

coupling. This can be seen as there is more than one oscillation in the example pulse in Fig. 5.2a.

We see that the threshold for superradiant emission appears to lie around $\Omega\, t_P = 0.57\pi$, and not exactly at the theoretically predicted value of 0.5π, corresponding to a 50% fractional excitation. This is a consequence of decoherence in between the end of the pump pulse and the superradiant emission. For superradiance to occur, there needs to be sufficient population inversion, such that even with spontaneous emission and potentially coherent emission into competing unobserved modes, there is still positive inversion by the time of the superradiant pulse. Below this threshold, the atoms cannot synchronize and are left in a state that is protected from collective cavity decay.

In Fig. 5.2c, we plot the time delay, t_{peak}, for the varying angular excitations. This curve is consistent with prior research on time delays, in that larger inversions lead to faster emissions [59]. For the simulation (purple solid line) we treated g as a free parameter. Otherwise, there would have been a constant time offset between theory and data. The theory fits when $g = 2\pi \times 450$ Hz. A normal-mode splitting measurement suggests a value of $g = 2\pi \times 635$ Hz. We attribute this disparity to oversimplification in the model.

It is important to note that these results rely on transverse excitation. If the atoms were excited through the cavity, then the atomic dipoles would be excited with the precise phase corresponding to their position in the cavity mode. This would result in a constructive (superradiant) emission for any excitation fraction. Furthermore, there would be no threshold and much shorter delay times for the synchronization of the atomic dipoles.

5.4 Collectively enhanced Ramsey lineshape

We harness the unique feature that a transverse $\pi/2$-pulse excitation places the sample into a subradiant state, shielding it from collective decay into the cavity mode. After a free evolution time T, a second $\pi/2$-pulse and superradiant pulse readout results in a collectively enhanced Ramsey lineshape.

In Fig. 5.3 the excitation detuning, δ_a, is varied and we plot peak emitted intensity for these detunings. In traditional Ramsey spectroscopy, the lineshape exhibits full sinusoidal fringes. However, in the collectively enhanced lineshape there are near-zero photon emission zones for regions of detuning which do not result in positive inversions of the sample. This is a fundamentally new lineshape which, to our knowledge, we are the first to demonstrate experimentally.

The data (black points) and simulation (blue curve) agree strongly. The width of the envelope of the fringe pattern is $\Delta f = 1/\tau_P = 3.33$ MHz, where $\tau_P = 300$ ns is the duration of each $\pi/2$-pulse. The frequency between adjacent fringe peaks is given by $1/T = 200$ kHz. We have chosen the dark evolution time $T = 5$ μs such that is significantly shorter than the natural lifetime of 21 μs so we still have a strong signal, but it is long enough that we can scan over numerous fringes. We note a slight asymmetry in the data which can be attributed to residual detuning-dependent pumping intensity.

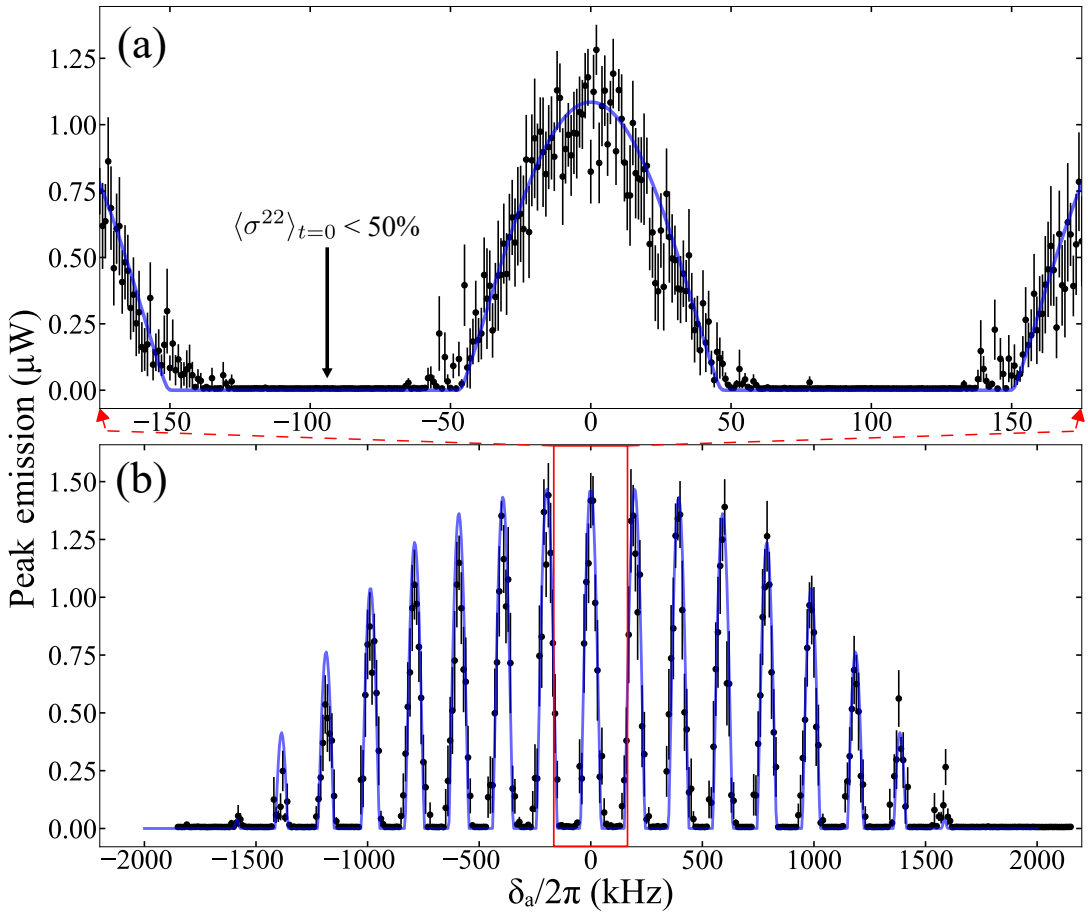

Figure 5.3: Collectively enhanced Ramsey lineshape when plotting peak emitted intensity for varying pump detuning, δ_a. (a) Zoomed-in scan around the center fringe, boxed in red in (b), taken with higher frequency resolution. (b) Data taken over the complete spectroscopic lineshape. The blue solid lines are simulations with an overall rescaled amplitude. Each data point in black is a mean of ten measurements, each from a separate MOT loading cycle. Figure adapted from [89]

The atomic ensemble is susceptible to spontaneous decay outside of the cavity mode as well as Doppler dephasing throughout the sequence including during the excitation pulses, dark evolution time, and time delay. To see the effect of the 5 μs dark evolution time we take a dataset (grey) for a 0 μs dark evolution time, which is equivalent to a Rabi interrogation sequence with the same Rabi frequency (intensity) as the Ramsey measurement, shown in Fig. 5.4. We see that as expected there is one fringe, of width approximately $\Delta f = 1/(600\text{ ns}) = 1.67$ MHz. The peak of this fringe exhibits a little over twice the power over the compared Ramsey fringe, reaching peak intensities of over 3 μW. This highlights the effect of the decoherence mechanisms taking place during the 5 μs dark evolution interval.

Typically with clocks and sensors, it is customary to attempt Rabi and Ramsey with equal interrogation times before deciding which is more suitable for the particular application. In this cavity enhanced readout, it is not feasible to have long Rabi interrogation times relative to the 21 μs natural lifetime, because superradiant

emission commences as soon as positive inversion is reached. Relatively longer interrogation times are only possible in the Ramsey scheme because atoms are protected against cavity decay after the first $\pi/2$ excitation pulse.

For the best laser stabilization, we must create an optimal discriminator for a laser to feedback on. One of the key parameters to consider in this context is maximizing the signal-to-noise ratio (SNR). Both Ramsey and Rabi methods present distinct advantages and drawbacks. Although our experimental setup does not allow us to conduct single excitation pulses with longer durations, it is possible that the relative SNR is more favorable for ensembles with maximal inversion, i.e. near the peak of a fringe. This suggests that an in-depth examination of the possible SNR is imperative, especially if the goal is to incorporate this data into a real-time feedback loop for laser stabilization.

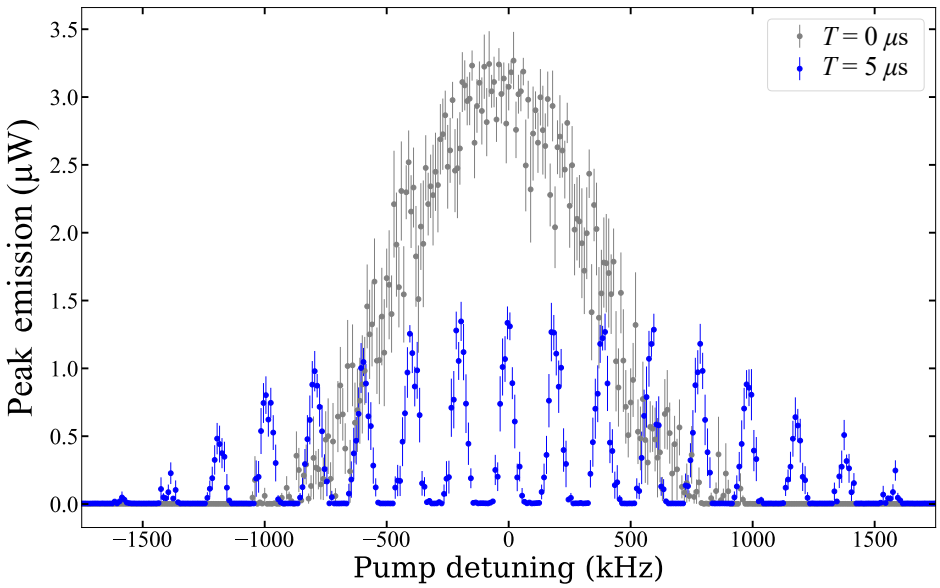

Figure 5.4: Collectively enhanced Ramsey fringes for zero dark evolution time (grey) and $T = 5\ \mu s$ (blue). We see a higher SNR in the peak zero dark time fringe, however, the slope of the fringe is less steep. The peak emitted powers are detected from one side of the cavity.

The superradiantly enhanced spectroscopic signal is characterized by its unique flat, almost zero-photon emission regions. Particularly intriguing are the distinct kinks observed at the transition between these flat regions and the fringe areas. Theoretically, these kinks could provide a highly sensitive discriminator for frequency locking, given their sharp transition. However, based on our current experimental results, the SNR around these kinks is suboptimal compared to the peaks of the fringes, making them currently unsuitable for real-time laser stabilization.

The collectively enhanced Ramsey spectrum has already proven to be a useful and efficient tool in tuning the interrogation laser to atomic resonance before starting a day of experiments. We scan the laser frequency and quickly map out a fringe pattern covering multiple fringes. Then we vary the dark evolution time, T. If

the center fringe at $\delta_a = 0$ remains stationary, then our pump laser is on resonance. Otherwise, we adjust the pump detuning to center ourselves on the fringe which does not shift for varying T. Within about 20 minutes, the interrogation laser can be calibrated to an impressive accuracy of tens of kHz.

5.5 Recycling of the atomic ensemble and preliminary discriminator slope

Each Ramsey interrogation imparts maximally two recoils per atom, one from the excitation $\pi/2$-pulses, and one from the emission along the cavity axis. This is minimal heating compared to traditional electron shelving methods, which heat up the sample beyond recapture. The ability to consistently repeat an experimental cycle is essential in mitigating the Dick effect. This makes it advantageous to subject the atoms to multiple Ramsey interrogations, enabling their reuse for numerous cycles before necessitating a fresh round of cooling and trapping.

Our preliminary approach was straightforward: we executed the Ramsey interrogation on the atoms, pausing for 100 μs between each sequence. This time of about five natural lifetimes ensured spontaneous decay of atoms that had not undergone superradiant decay.

In Fig. 5.5 we conducted ten Ramsey sequences per MOT cycle for varied detunings. The results, which plot peak amplitude against detuning for three free evolution times, showed that longer times result in decreased pulse amplitudes. When focusing on the center fringe, as seen in Fig. 5.5b and d, there's a noticeable chirp of the fringe peak. This is attributed to the recoils from each sequence inducing a Doppler shift in the atomic resonance. As the atoms accelerate away from the pump beam, an increasingly higher frequency is needed to excite them. This phenomenon explains why, by the tenth pulse (indicated in red), the center of the fringes has shifted in comparison to the initial pulses (indicated in purple). Moreover, each fringe's shape skews due to the Doppler-affected distribution, and the contrast is reduced, likely a consequence of the heating.

The Doppler effects are also evident by looking at absorption images taken with and without ten resonant Ramsey readouts, as depicted in Fig. 5.6. In the absence of Ramsey interrogations, the atomic spread appears isotropic, reflecting a uniform temperature-related dispersion in all directions. In contrast, panel (b) distinctly demonstrates the atoms are considerably hotter along the horizontal axis. This can be attributed to the atoms' repeated emissions along the cavity axis. The wider atomic sample was also a quick sign telling us whether our cavity was still locked.

To counteract the heating from the two recoils per sequence, we cool for 1.7 ms on the single-frequency red MOT. Then we turn cooling off for 300 μs while we perform a Ramsey interrogation and readout resulting in a 2 ms cooling cycle, as depicted in the top left inset in Fig. 5.7a. This procedure can be repeated for hundreds of repetitions within a MOT cycle, producing detectable pulses, until atom losses due to background gas collisions in our vacuum chamber become too significant. Shadow images of the atomic cloud enabled us to estimate the atom number after increasing numbers of repetitions within a single MOT loading cycle.

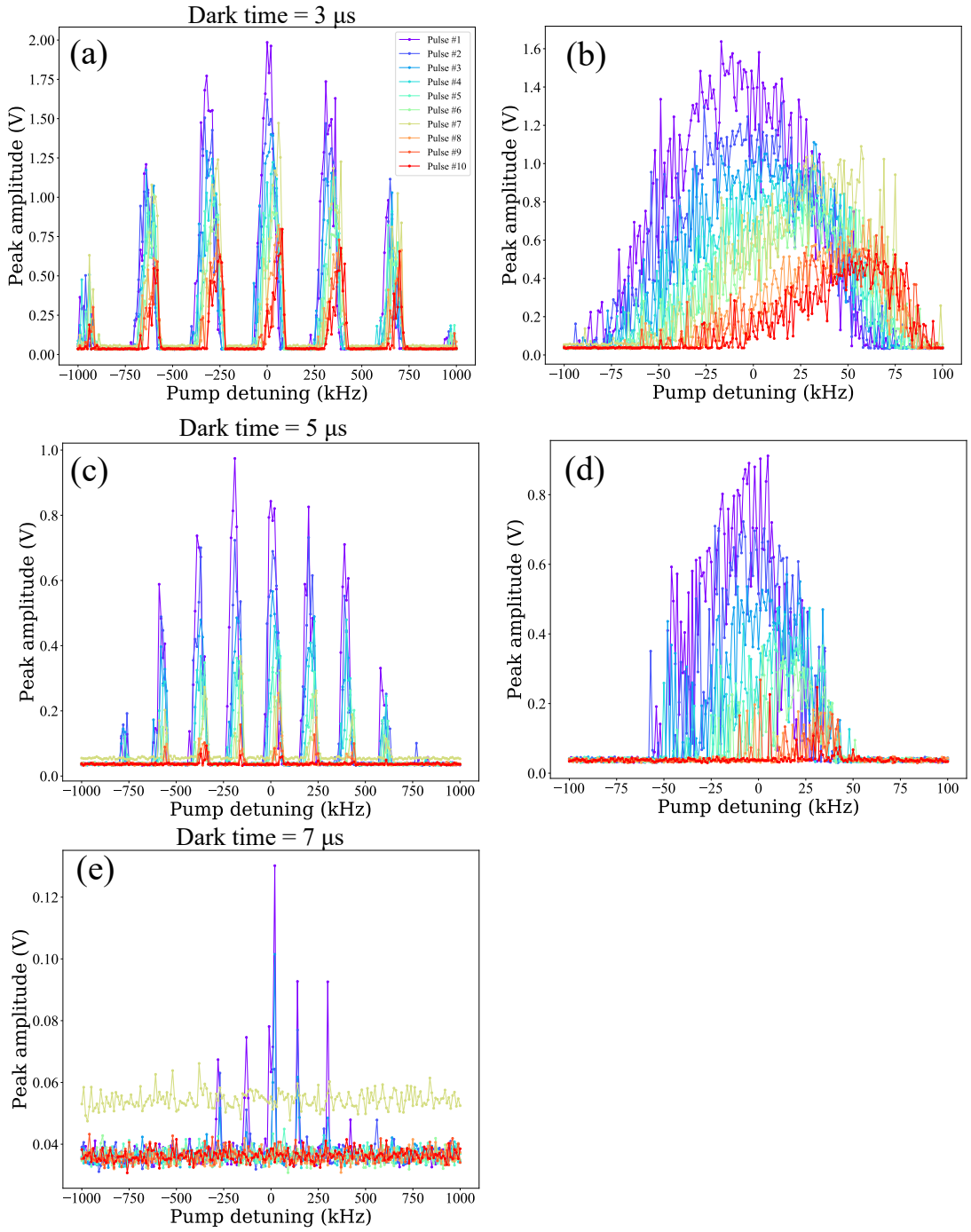

Figure 5.5: Collectively enhanced Ramsey fringes for ten repeated Ramsey interrogations on a single MOT cloud for various free evolution times T. (a), (c), and (e) are scans taken over the entire Ramsey envelopes corresponding to 3 μs, 5 μs, and 7 μs. (b), and (d) are zoomed-in scans around the center fringes to highlight the affected fringe shape. We note that across all of these scans, the seventh pulse (light green) has a significantly higher baseline. This suggests an unintentional action in the experimental sequence during this pulse index.

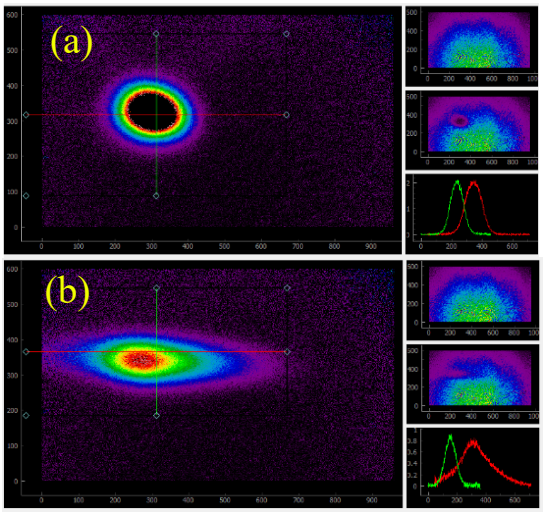

Figure 5.6: Absorption images of the atoms (a) without and (b) with ten Ramsey excitations. The superradiant emissions into the cavity mode causes heating along the cavity axis. Each has three corresponding panels on the right. Top is an image with the imaging beam and no MOT. Middle image is with the MOT. Bottom is the calculated optical density from these two images in the vertical (green) and horizontal (red) directions.

The inset on the top right of the figure charts atom numbers under three distinct conditions: post-Ramsey excitation pulses (represented in yellow), without these pulses (in blue), and with the 689 nm MOT continuously on (in purple). There is a slightly increased loss when the excitation pulses are applied compared to when they are blocked. The recapture appears effective, and turning off the MOT for 300 μs every 2 ms does not lead to more losses than what is attributable from background gas collisions.

This 2 ms was chosen to effectively counterbalance the heating induced by the interrogation. In the future, clever geometry could possibly be applied where we cool specifically along the axis where the known heating occurs.

In Fig. 5.7a, we step the frequency of the pump laser in between consecutive interrogations with intermittent cooling. The black data points are peak emissions as we step the frequency symmetrically around resonance. In contrast, the red data points are peak emissions in which one frequency step is closer to resonance than the other, as shown in the lower left inset. The asymmetrical frequency stepping results in higher emissions for the frequency step which is closer to resonance. Upon averaging over 30 traces, the resulting pattern clearly depicts the red points alternating in intensity, while the black points display a more consistent emission. Both datasets exhibit diminishing amplitude due to the loss of atoms over time.

We can define a frequency locator, FL $= \langle \frac{P_{i+1}-P_i}{P_{i+1}+P_i} \rangle$, where P_i is the peak intensity of the ith pulse within a given cycle. This FL offers a preliminary error signal to which a servo system could provide gain in order to stabilize a laser's frequency. The principle behind this is straightforward: if the laser is stepped about a fringe, achieving similar excitation populations on either side of the fringe would imply

that the laser is on resonance. A non-zero difference between these populations would indicate a departure from resonance, offering a direction for corrective gain. By dividing this difference by the sum, we account for varying atom numbers, which arises from both shot-to-shot variations in a MOT as well as the gradual decline in atom numbers caused by background gas collisions.

The inset in Fig. 5.7b illustrates the relationship between the FL and the detuning, considering the free Ramsey range (FRR) and a frequency stepping size of $0.1\times$ FRR in our dataset. The solid cyan line represents the collectively enhanced FL while the black dotted line is derived from a conventional Ramsey lineshape, with equivalent stepping and signal sizes. In the plot, we average FL values for non-overlapping pairs of pulses over the course of the 30 traces, taken over the course of several minutes. The constant values, supported by best-fit lines consistent with zero slopes, signify no systematic change in frequency taken throughout the 30 MOT loading cycles. The deviations represent frequency excursions of the pump laser on the time scale of the 6-second intervals between traces, with intervals limited by how fast we could extract the data off of the oscilloscope.

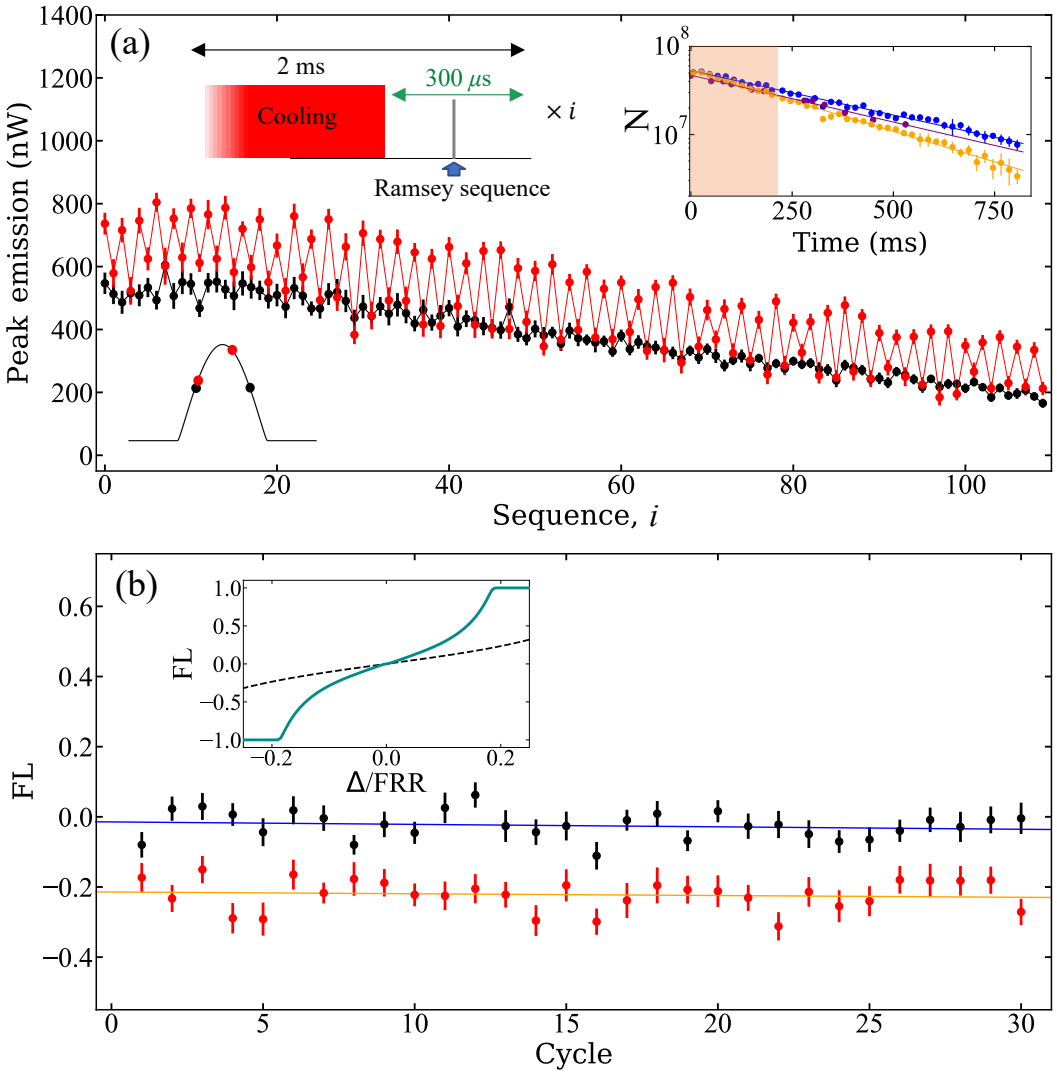

Figure 5.7: (a) Repeated Ramsey sequences with frequency stepping in between readouts. We intermittently cool the atoms in periods of 2 ms as in the diagram in the top left. The top right is MOT atom number estimated by shadow imaging for increasing number of repeated sequences in a MOT cycle. This demonstrates we still have millions of atoms for hundreds of sequences with excitation pulses blocked (blue), excitation pulses on (yellow), and a continuously running MOT (purple) for reference. Each data point is an average of ten measured atom numbers with error bars representing the standard deviation of the mean. (b) Frequency locator averaged over the 108 pulses in each trace taken in non-overlapping pairs of superradiant pulses. Error bars are standard deviations of the mean of the 54 pairs of pulses. Solid lines are best-fit lines, consistent with zero slopes. Inset: conversion of FL to laser detuning for our step size and fringe width for the collectively enhanced Ramsey lineshape (cyan) and a traditional Ramsey lineshape (black dotted) for reference. Figure adapted from [89]

CHAPTER 6

Quasicontinuous superradiant lasing below the natural linewidth

In this chapter, we turn our attention to the the spectral properties of superradiant emission. Until now, we have primarily focused on the intensity and temporal characteristics. With pulses occuring on the order of a microsecond, the spectra are heavily Fourier broadened beyond the natural linewidth, rendering them rather uninteresting as clock light. To have better frequency resolution, we need to extend the duration of the superradiant emission beyond the natural lifetime of the excited state. This is the underlying principle in an active atomic clock, in which the clock light is continuously derived directly from the atomic emission. To prolong the supperadiance, one could supply new excited atoms, which synchronize with the emitting atoms inside of the cavity, or reexcite the atoms which have already emitted into the cavity mode. The content and findings of this chapter are based on our recently published work presented in [90].

6.1 Experimental implementation and repumping scheme

We explore quasicontinuous superradiant lasing by incoherently repumping atoms. This experiment uses mainly the same experimental apparatus from previous chapters, as depicted in Fig. 6.1, with two additional repump lasers at 688 nm and 689 nm.

Altogether we utilize four repump lasers to incoherently populate the excited lasing state, $^3P_1$, $m_j = 0$, as depicted in Fig. 6.2. The vertical bias field, set at 2 Gauss, ensures a frequency splitting of 4.2 MHz among the magnetic sublevels of $^3P_1$. This configuration allows us to avoid populating the $m_j = 0$ sublevel through deliberate frequency and polarization choices.

For the 689 nm repump laser, we adopt a polarization perpendicular to the bias field, addressing the transitions to $^3P_1$, $m_j = \pm 1$ states. A specific detuning allows us to address only one. The 688 nm repump laser is polarized parallel to the bias field to drive the $\Delta m_j = 0$ transitions between $^3P_1$, $m_j = \pm 1$ and $^3S_1$, $m_j = \pm 1$.

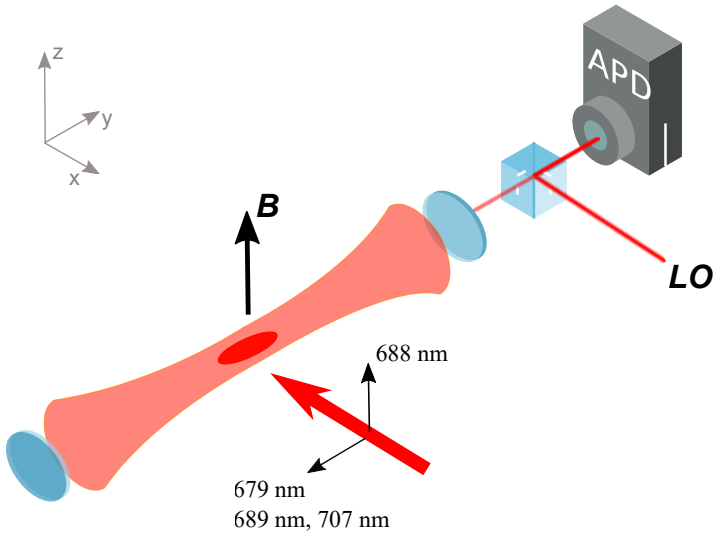

Figure 6.1: Experimental setup for quasicontinuous lasing. The setup features four repump lasers oriented transversely to the cavity axis. The polarizations of the 688 nm and 689 nm repump lasers are selected to avoid inducing light shifts on the upper lasing level. Superradiant emission into the cavity mode is measured through a beat detection with a stable reference laser situated behind one of the cavity mirrors.

The ${}^3P_1$, $m_j = 0$ is not depopulated due to selection rules between ${}^3S_1$, $m_j = 0$ and ${}^3P_1$, $m_j = 0$ [37]. The 679 nm and 707 nm repump lasers are also necessary to depopulate the atoms which decay into the ${}^3P_2$ and ${}^3P_0$ levels.

It is important that we repump the atoms incoherently into the upper lasing state to avoid introducing any unwanted phase noise from the pump light onto the superradiant lasing. If the lasing transition was excited directly, the lasing states would undergo a light shift from this resonant pump laser. Since we operate in the bad cavity regime, a time-dependent light shift would cause the frequency emitted by the atoms to fluctuate as well. By incoherently repumping, we ensure that the superradiant lasing remains free of this external phase perturbation.

A second critical step we took which allows for much steadier lasing frequency output was to co-align all of the repump lasers and have them oriented perpendicular to the cavity axis, as in Fig. 6.1. In the absence of any confining forces, the atoms accelerate due to the recoils induced by the repump lasers. Any velocity component the atoms acquire along the cavity would cause the emitted superradiance to exhibit a Doppler shift over time, chirping the output frequency. By directing recoils perpendicular to the cavity axis, we aim to minimize this effect. Furthermore, the co-alignment of repump lasers ensures a consistent repump intensity experienced by the atoms. Even as the atomic cloud is propelled by radiation pressure, it remains comfortably within the Gaussian intensity profiles of the beams, thus preventing intensity variations that might influence the lasing dynamics.

For each incoherent excitation to the ${}^3P_1$, $m_j = 0$ sublevel, branching ratios suggest that an atom absorbs, on average, nine repump photons and undergoes

spontaneous emission of eight photons. The frequency recoil shift of one of these red photons is approximately 10 kHz.

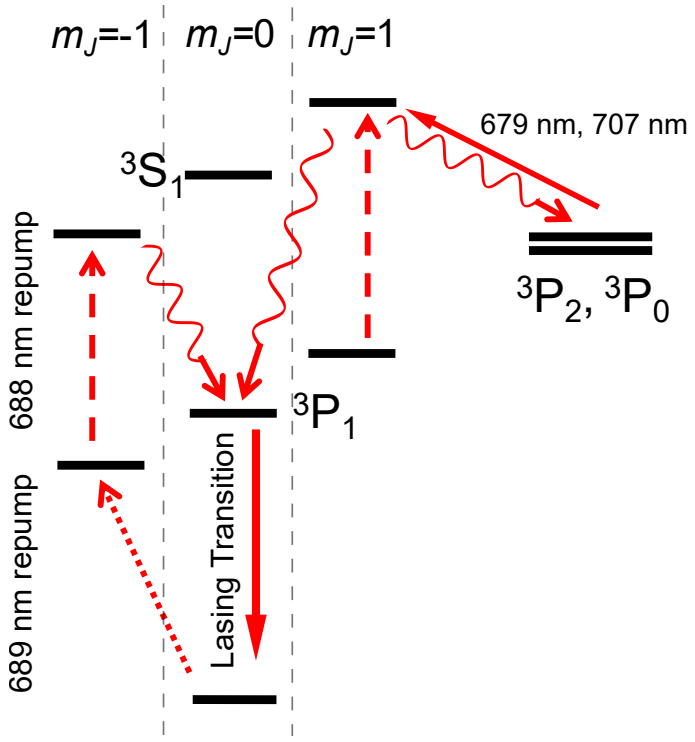

Figure 6.2: Relevant level scheme of ^{88}Sr showing the lasing levels, as well as all of the repump lasers required to incoherently populate the upper lasing level. The 707 nm laser is detuned to control the rate at which atoms are depleted from $^3P_2$ during lasing. This effectively creates a lower gain in the system, allowing for extended pulse durations.

6.2 Quasicontinous lasing

Once we were able to extend the pulses using the incoherent repumping scheme, we noticed the pulses exhibited a very oscillatory, spiking behavior. They lasted up to about 100 μs, as illustrated by the pulse shown in Fig. 6.3a. When all of the repump lasers are applied resonantly, a majority of the atoms are excited rapidly into the upper lasing state. This results in a very enhanced collective emission rate into the cavity mode, reaching peak powers of 100s of nW. This collective decay becomes much more rapid than the rate at which atoms are replenished to the upper lasing state. Only once most of the atoms have emitted, will the repump rate overcome the collective emission rate and the population inversion will begin to grow. This unstable balance between the collectively enhanced emission rate and the repumping rate to the excited state causes the amplitude of the collective dipole to oscillate in time, causing the spiked behavior as in Fig. 6.3a. After about 100 μs, heating and deflection causes the atoms to leave the cavity mode, ceasing the superradiant emission.

A key adjustment to balance the repumping rate to the collective emission rate thereby producing steadier lasing intensity over time, is the frequenecy of the 707 nm repump laser. By detuning the 707 nm repump laser, we can reach a steady-state lasing regime, where the rate at which atoms are repumped out of $^3P_2$ perfectly balances the collective emission rate for over a millisecond. An example of this is shown in Fig. 6.3b. This balance is acheived at a detuning of $2\pi \times 60$ MHz (about nine times the linewidth of the 707 nm transition, γ_{707}) from the $^3P_2$.

Such a detuning lowers the rate at which atoms are pumped out of $^3P_2$, leading to an effective 'shelving' of atoms, which can be saved for later. By shelving atoms in $^3P_2$, we are removing atoms from the lasing transition levels, effectively shrinking the size of the relevant collective Bloch sphere. This reduction decreases the collective emission rate, or equivalently, torque on the collective Bloch vector downwards. We are essentially spreading out our gain over time, so that we have decreased superradiant lasing intensity, but it lasts longer.

To investigate the differing dynamics, we turn on 461 nm MOT light and measure fluorescence of atoms in the ground state after applying the repump lasers for 100 μs. With the detuned 707 nm repump laser, about 10-15% of the total atoms are in the ground state. This suggests most of the atoms are shelved in $^3P_2$. In contrast, when applying a resonant 707 nm repump laser, 50% are in the ground state.

Moreover, the less aggressive repumping minimizes the physical displacement of atoms due to repumping recoils. As a result, the atoms can linger within the cavity mode for more extended periods. Such adjustments culminate in lasing durations extending up to several milliseconds. For further information on the deflection of the atomic cloud in these two different regimes, refer to [90].

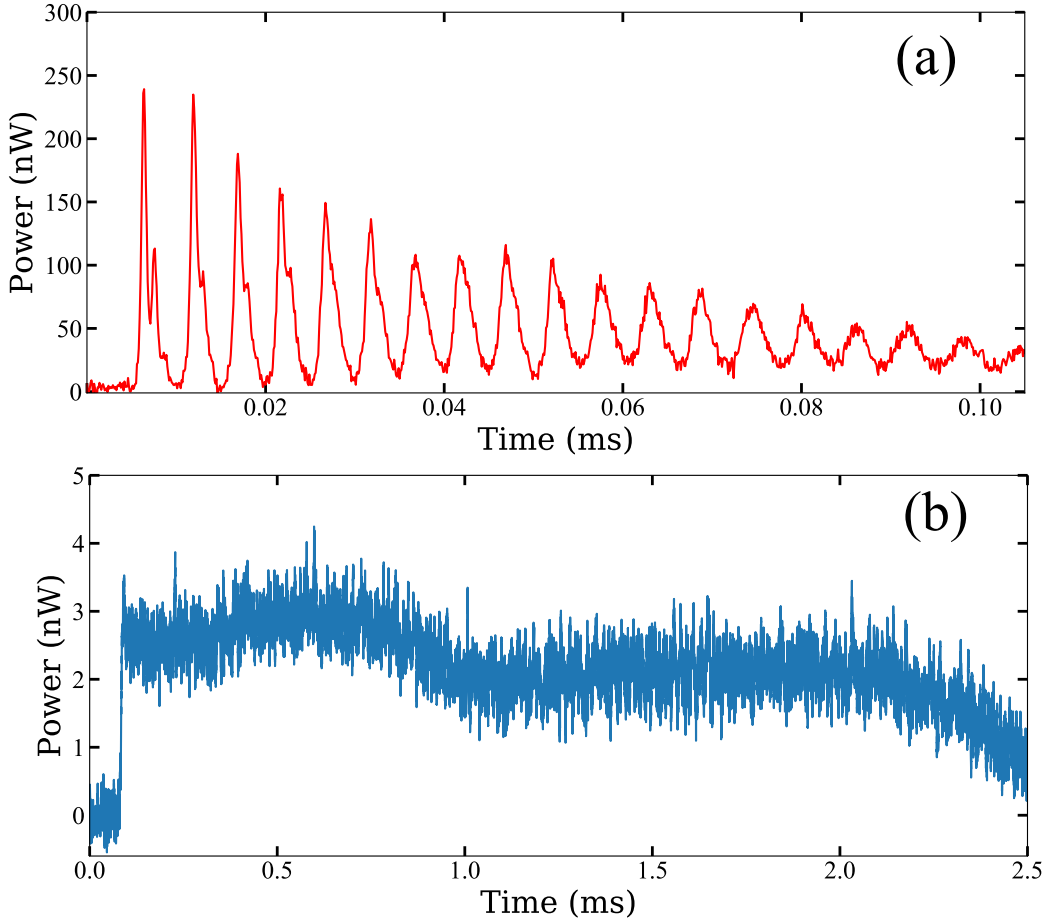

Figure 6.3: Examples of quasicontinuous superradiant lasing pulses in the oscillatory and steady-state regimes. (a) Lasing in the oscillatory regime achieved by applying the 707 nm repump laser resonantly. (b) Lasing in the steady-state regime achieved by applying the 707 nm repump laser detuned by $2\pi \times 60$ MHz. This pulse has a much lower output intensity, but achieves steady lasing intensities for over a millisecond. Kernel smoothening was applied to reduce some of the fast noise on the signal.

6.3 Cavity pulling

Identifying the most stable segment of the pulse is crucial when aiming to investigate its linewidth. One way in which we find the optimal portion of the superradiant output to investigate is by analyzing the cavity pulling coefficent throughout the emission. A main appeal of bad cavity lasing is that the frequency of the emitted light is less susceptible to fluctuations in the cavity's resonance frequency. The cavity pulling coefficient is defined by the equation, $P = \Delta f_l/\Delta f_c$, where $\Delta f_l, \Delta f_c$ is the detuning in the lasing and cavity resonance frequencies, respectively. This metric is useful, as it elucidates the extent to which shifts in the cavity resonance influence the frequency of the emitted light.

We investigate the spectrum of the superradiant emission by performing a heterodyne beat measurement by overlapping the light emitted from the cavity with the stable reference laser. The reference laser is stabilized as described in chapter 3, and sits at about 40 MHz away from the lasing transition frequency. We measure the beat frequency on an APD. To assess the impact of changes to the cavity resonance on the emitted light, we actively tune the cavity via the piezo and subsequently record the beat frequency of the superradiant output and the reference laser.

Figure 6.4a showcases a composite of five spectrograms, each resulting from a separate beat measurement, where Δf_b is the deviation from the mean beat frequency. The lasing occurs with varying cavity detunings, δ_{cav}, ranging from -600 to 600 kHz in increments of 300 kHz. In Fig. 6.4b, each of these five pulses is further subdivided into time segments, each lasting 200 μs. Within each segment, the emitted frequency profile is fitted with a Lorentzian, extracting the central lasing frequency. This analysis reveals an intriguing trend: the cavity pulling over time initially surges but begins to stabilize as it approaches 1 ms. Theoretically, the cavity pulling coefficient as a function of time is given by $c_p(t) = \frac{2\gamma_D(t)}{2\gamma_D(t)+\kappa}$ [91], where γ_D is the Doppler width of the ensemble along the cavity axis, which for us is the dominant broadening mechanism of our atomic ensemble. With this equation, we estimate a Doppler width of about 50 kHz initially, and then levels off at about 90 kHz.

Focusing on the data points in the shaded green rectangle, we find a slope of $\frac{\partial c_p}{\partial t}$ which is consitent with zero. In the initial .5 ms, we attribute the rapid increase in cavity pulling to the temperature increasing. The beginning segments of the lasing have lower cavity pulling coefficients because the atoms lasing then have reached the upper lasing level after absorbing fewer than the average number of repump photons. As the lasing progresses, the contributing atoms tend to have a more consistent average number of recoils, hence a steadier temperature and, consequently, a more uniform cavity pulling coefficient. Each atom only contributes about one or two photons to the superradiant lasing. This is acceptable in our system because of our high atom number.

This region of apparent stability in the lasing from about 1 ms to 2 ms serves as the motivation for our investigation of linewidth in the following section.

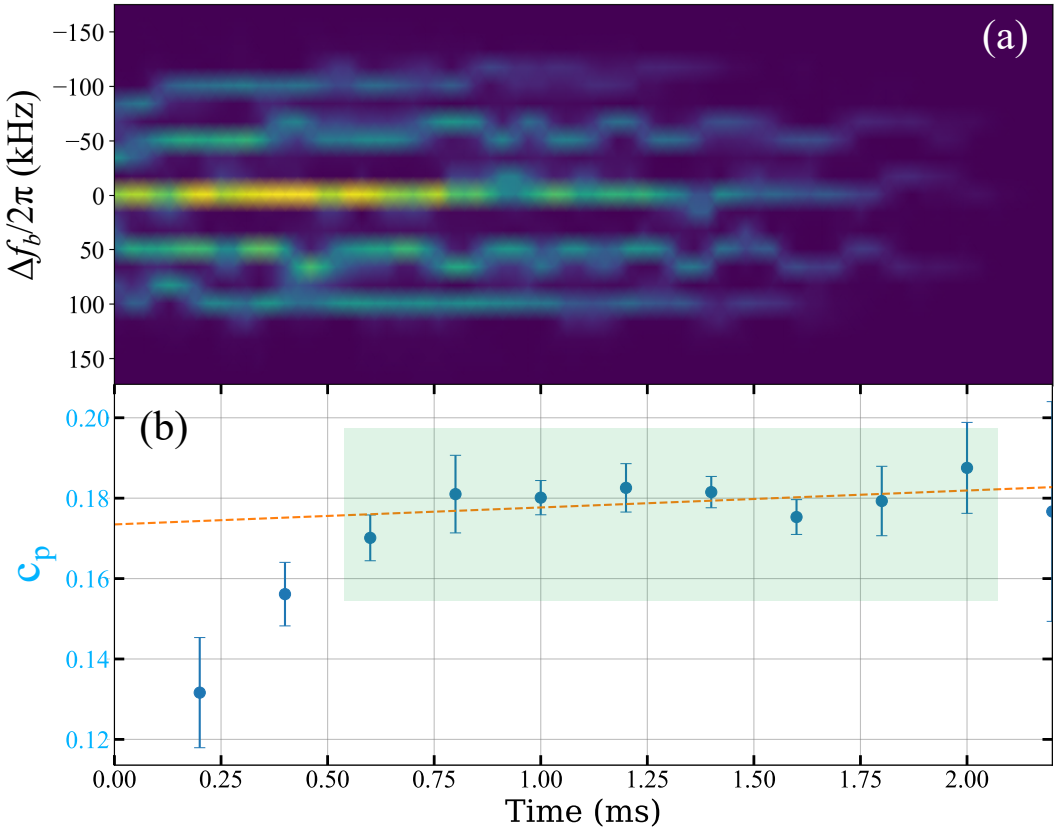

Figure 6.4: Investigations of cavity pulling dynamics. (a) Combined spectrogram with 60 μs overlapping square windows of five distinct pulses with cavity detunings, $\delta_{cav}/2\pi$ from -600 kHz to 600 kHz in 300 kHz increments. (b) Derived cavity pulling coefficient plotted for 200 μs segments of the four detuned pulses. Within the region highlighted by the green rectangle, the rate of change in cavity pulling over time, $\frac{\partial c_p}{\partial t} = .004(4)$ /ms , suggesting a nearly flat trend consistent with zero cavity pulling.

6.4 Frequency stability

In Fig. 6.5a we plot the output frequency over time as a spectrogram, with overlapping 50 μs square windows every 25 μs. This time-windowing exposes certain transient dynamics in the start, followed by a relatively steady-state region. Towards the end, we observe a decline in power as well as a frequency drift.

To determine the power spectral density (PSD), we compute the squared magnitude of the discrete Fourier transform of the beat data, plotted in Fig. 6.5b. For enhanced spectral resolution, we employ zero-padding on the time-domain signal. It is crucial to emphasize that while zero-padding provides finer frequency resolution by interpolating points, it does not alter the intrinsic linewidth. The linewidth is then determined by measuring the full width at half maximum (FWHM) of the main spectral peak. Given our use of rectangular time windows for the data, the Fourier transform inherently results in a sinc function (sine cardinal), as

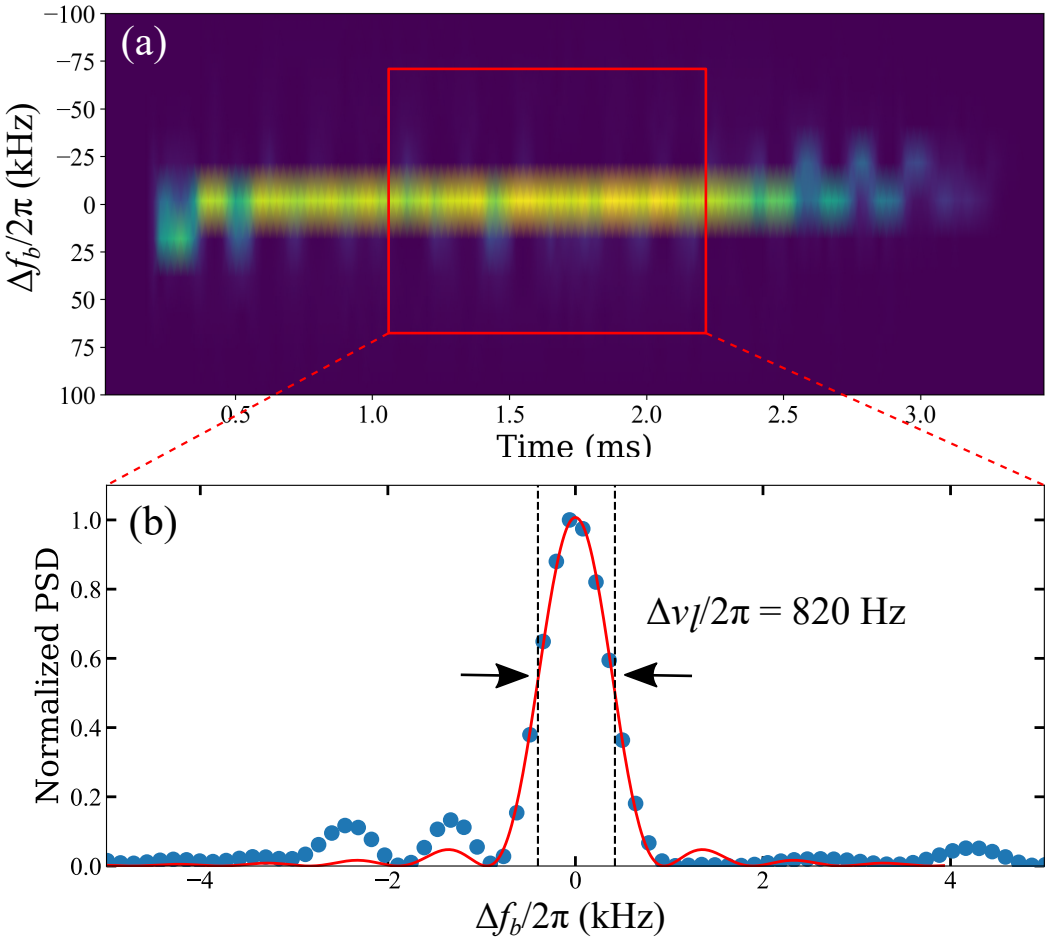

Figure 6.5: (a) Spectrogram of heterodyne beat measurement, created using 50 μs windows. The segment enclosed by the red box, spanning from 1.1 ms to 2.2 ms, is selected for Fourier transformation with zero-padding. (b) PSD obtained by squaring the Fourier transform of the beat signal. The red solid line represents the best-fit sinc^2 function to the data. The FWHM is indicated by the distance between the arrows and the dotted lines. This figure has been adapted from [90].

detailed in [92]. Therefore, we fit a sinc^2 function in the calculation of the FWHM of the PSD.

In Fig. 6.6a we plot the normalized PSD for incrementally extended segments of the beat signal, represented by ΔT. We observe a progressive narrowing of the central peak over time. However, after approximately $\Delta T = 1.2$ ms, the central feature does not get any narrower, and the side components begin to develop, perhaps indicating a bifurcation or bistable regime of the lasing output [93]. This limitation of the narrowing is also shown in Fig. 6.6. Here we plot the FWHM of the fitted sinc^2 function for varying segment durations, with corresponding color to the duration lengths in the legend in part a. The orange dotted line is the Fourier limited linewidth of a rectangular window $\Delta\nu_l/2\pi = 0.8859/\Delta T$ [92]. Beyond the minimum value, the output frequency starts to drift due to unstable

lasing dynamics and technical noise. The dotted purple line represents the natural linewidth of the atomic transition. We reach a linewidth of $\Delta\nu_l/2\pi = 820$ Hz, nearly an order of magnitude below the natural linewidth.

While the spectrum's center narrows with increased time duration, it plateaus around 1.2 ms. Subsequently, the sidebands become more pronounced, accompanied by a consistent directional frequency drift. A thorough investigation into these dynamics extends beyond the primary scope of our study.

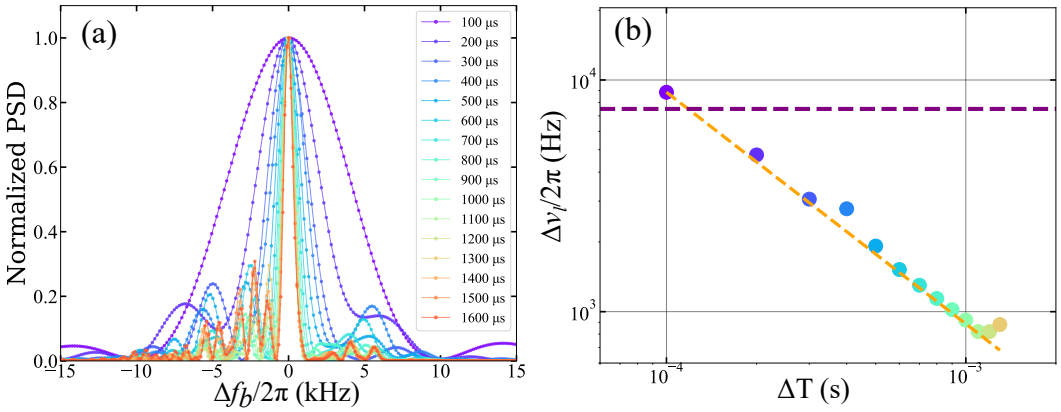

Figure 6.6: (a) Normalized PSD for varying durations, with lengths denoted by the colors in the legend, starting from the 1.1 ms mark in the trace in Fig. 6.5. (b) FWHM of the central peak for increased durations. The color scheme here mirrors the legend in part (a). This figure is adapted from [90].

It is worth highlighting the distinctions between our research and the pioneering work in [94]. Our study falls into a qualitatively different regime: our single-atom cavity cooperativity is three orders of magnitude lower, suggesting the potential to reach a lower Purcell limited linewidth. Our atom number allows us to turn down the repump rate out of $^3P_2$ to achieve stable output for more than a millisecond, compared to the 150 μs samples in [94]. We reach a linewidth of 820 Hz, compared to 6.0(3) kHz. They operate with an optical lattice, presumably in the Lamb-Dicke regime. Our system is suspended in free space, so we are lasing much narrower than the Doppler broadened gain medium, crucial for proposals such as [95]. The $^3P_2$ shelving we introduce opens up possible avenues for fully continuous superradiant lasing schemes which I discuss briefly in the outlook section.

CHAPTER 7

Iodine in a hollow-core fiber as a portable frequency reference

In this chapter, we investigate a very different system from the previous chapters which explores laser stabilization using iodine within a hollow core fiber. Portable and secondary optical frequency standards are important for many applications including optical-sensing, geodesy, and telecommunications. These applications demand precision, reliability, compactness, and user-friendliness beyond the laboratory setting. Our research, conducted at DFM, aligns with an initiative supported by the European Space Agency, aiming to address these critical needs.

7.1 Background

Traditional fibers guide light by using claddings and variations in the refractive index, while hollow core photonic crystal fibers (HCPCFs) employ anti-resonant cladding structures that encompass evacuated cores, providing photonic band gap guidance in air. These empty cores can be filled with gaseous media and has led to their application in diverse research domains involving laser interactions with atoms and molecules including gas sensing [96, 97], non-linear optics [98, 99], high-resolution spectroscopy [100–103], and laser stabilization [104–106].

Although in many ways very similar to a bulk cell, performing spectroscopy in a HCPCF has many advantages due to its small core, resulting in excellent overlap between counterpropagating probe and pump beams. This ensures strong light-matter interactions at low powers. The major challenge the small core presents which limits the narrowness of the spectroscopic features is the amount of time the atom or molecule has to coherently interact with the laser field before colliding with a wall, an effect known as transit time broadening. HCPCF systems show immense promise and potentially offer superior performance for specific applications. By encapsulating these fibers with a gaseous medium inside [107], one can achieve entirely fiber-based configurations. Such setups not only enhance portability but also ensure stable and robust alignment.

Iodine is atomic number 53, and exists as a symmetric diatomic molecule

consisting of two iodine atoms joined by a single covalent bond. This project uses commercially produced $^{127}I_2$. It exists as a dark semi-lustrous, non-metallic solid, which we place in a Young valve as depicted in Fig. 7.1.

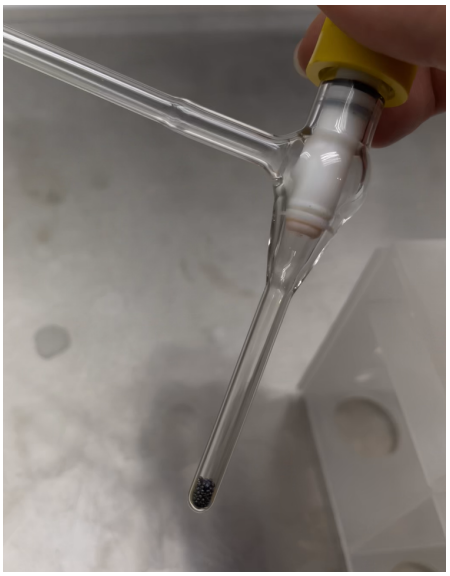

Figure 7.1: Iodine in our experiment is transported under a fume hood into a Young valve.

Iodine has a rich history in the field of frequency standards. Before optical frequency combs were available, the wealth of stable, narrow lines in iodine were used as a "molecular" frequency comb, allowing researchers to transfer the stability in one part of the frequency spectrum to another. Iodine is also a promising candidate in HCPCF systems because of its larger mass, reducing the transit time broadening compared to lighter molecules. Other research using HCPCF is based on hydrogen, acetylene, and rubidium [103, 105, 106, 108, 109].

The International Bureau of Weights and Measures (BIPM) recommends using iodine between 515-560 nm as a secondary representation of the second and practical definition of the meter [110, 111]. In particular, it recommends the a10 hyperfine component of R(56)32-0 [112]. We will investigate the R(56)32-0 transition as it conveniently has a wavelength of 532 nm, accessible by a frequency-doubled Nd:YAG laser. R(56)32-0 is a rovibronic transition that occurs when a molecule in the $X^1\Sigma_g^+$ electronic transition, with rotational quantum number 56 and vibrational quantum number 0, transitions to the $B^3\Pi_{0_u^+}$ electronic state with rotational quantum number 57 and vibrational quantum number 32. This transition consists of 15 hyperfine components labeled a1 to a15 [113].

The current state-of-the-art iodine systems are Nd:YAG lasers stabilized to a transition at 532 nm ultimately reaching instabilities of $2 - 5 \times 10^{-14}$ at 1 s [114, 115], and are based on fragile, meter-scale glass iodine cells operated with a cold point dispenser at -15 degrees C.

The current best iodine in a HCPCF system achieves a shot-noise limited instability of 2.3×10^{-12} at 1 s [116].

7.2 Experimental apparatus

We use an anti-resonant HCPCF (GLOphotonics PMC-C-Green-40), with core diameter of 40 μm and $1/e^2$ mode field diameter of 26 μm. A photograph of one end is shown in Fig. 7.2.

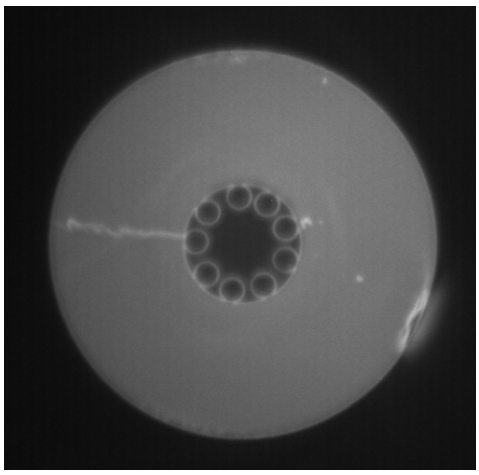

Figure 7.2: Photograph of an end facet to our HCPCF. Anti-resonant structure can be seen surrounding the empty core, with diameter of 40 μm. The inside is filled with various pressures of iodine in our experiments.

Although we were aware of the troubles of iodine reacting with metal, we still attempted to place the fiber inside of a stainless steel vacuum chamber in our first setup. Initially, we used a copper cold point to control the iodine pressure inside the vacuum chamber. This quickly proved to be problematic as we saw what we presumed to be yellowish copper-iodide (CuI) layer on the exposed copper. This caused us to switch to a Young valve as the iodine dispenser, which was cooled by a two stage Peltier element with a fan and heat sink (TEMA-AP-40-12). This new cold point was surrounded in styrofoam as shown in Fig. 7.3.

To gauge the amount of iodine we could load we investigated the amount of transmitted intensity through our vapor. Intensity I travelling through an absorbing medium suffers attenuation given by the Lambert-Beer law, $\frac{dI}{dz} = -\alpha I$, as the light is scattered. We calculate the absorption coefficient, α, by the equation,

$$\alpha \cdot l = -\ln\left(\frac{I}{I_0}\right) = -\ln\left(\frac{V_{\text{min}} - V_{\text{zero}}}{V_{\text{max}} - V_{\text{zero}}}\right) \tag{7.1}$$

where I is the transmitted intensity, I_0, is the incident intensity before the iodine, and l is the length of the fiber. We experimentally determine this by measuring on a photodetector V_{min}, the voltage at the bottom of the Doppler broadened absorption dip, V_{max}, the voltage at the top, and V_{zero}, the voltage when we block the beam completely (zero-point of the balanced detector). We measure this using an oscilloscope trace across the resonance such as the one in Fig. 7.4.

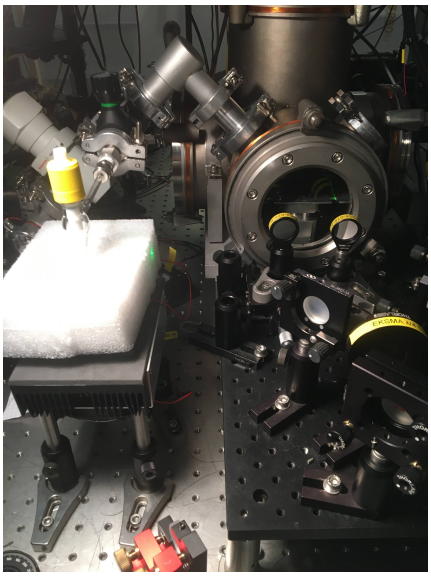

Figure 7.3: Metallic chamber setup. This proved to be problematic in that the vacuum chamber was reacting and making compounds with the iodine over time. The very big chamber also meant a long filling times were required for the HCPCF.(Picture taken: Jan. 2021).

The large metal chamber severely limited how quickly we could fill the chamber and subsequently the HCPCF with iodine. It took a long time to get a strong α, only reaching 0.2 in HCPCF after 20 minutes of 36 Pa of iodine (pressure at room temperature). We demonstrate this in a test where we set the cold point to a specific temperature and then waited, taking a measurement of α every couple of minutes. After this, we closed off the iodine and continued the measurements to observe the system's response. The top plot in Fig. 7.5 depicts α in both the fiber and metallic chamber throughout these tests. We observe a significant delay between the α responses we observed in the chamber and in the fiber. We were unable to identify hyperfine features in any of the spectroscopic measurements using this chamber.

Therefore, we switched to a no-metal setup. We placed the HCPCF along two small glass tubes, which were held together by Torr seal, then further held in place by a couple of pieces of teflon tape. We placed these tubes which held the HCPCF inside of a larger 20 mm glass borosilicate tube. The end glass tube pieces were connected to the main piece by plastic connectors and rubber o-rings. One glass tube end was connected to a teflon T-piece, to both the iodine cold-finger and the vacuum turbo pump. The schematic of the new and improved setup is shown in Fig. 7.6, with the actual setup depicted in the collage in Fig. 7.7.

This new chamber allowed us to more quickly vary the iodine pressure within the HCPCF and reach higher α values. Now we could reach $\alpha = 0.4$ in 25 min. Changes in α in the glass tube chamber and fiber were very coordinated, as shown by the nearly simultaneous filling times in the bottom plot of Fig. 7.5. The glass chamber meant there were no compounds forming between metal and the iodine. This allowed us to observe the hyperfine features presented in the next section.

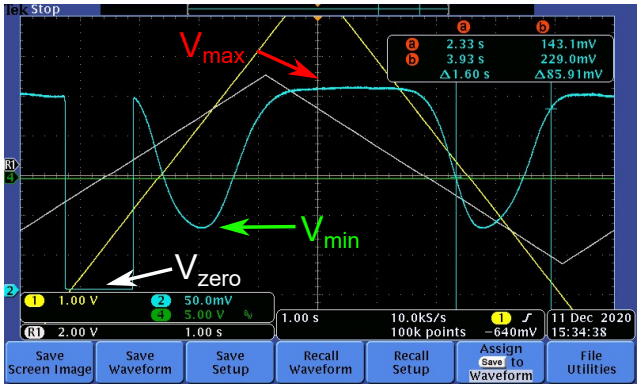

Figure 7.4: Example oscilloscope trace from which we could calculate α.

Our light source is a frequency doubled Nd:YAG laser at 1064 nm. We align the laser through the HCPCF and retroreflect it, measuring the returning intensity on a balanced photodetector. We also have a free space path, also retroreflected, in order to compare α in the HCPCF with that of in the free space of the glass tube chamber. The vacuum system was connected to a turbo pump and achieved an ultimate pressure of approximately 2 $\times 10^{-5}$ mbar, measured with a vacuum gauge.

Glass is very fragile and a lot of it is used in the current set-up. It is important to check regularly for cracks, and to tighten different parts of the experiment incrementally, looking for any slight bends along the way.

Based on simulation results estimating the optimal signal-to-noise ratio SNR for various HCPCF lengths, we selected a length of 1.3 m. There exists a delicate balance to consider. With a shorter fiber length, there is a reduced filling time and higher pressures are required to reach the same optical depth. The higher pressure allows for an increased I_{sat} and yields a better SNR before oversaturating. However, these pressures lead to collisional broadening, approximated at ~ 100 kHz/Pa. In contrast, a longer fiber requires less iodine to reach the same absorption, meaning reduced collisional broadening. A disadvantage is its extended filling time and therefore slightly higher background gas pressure.

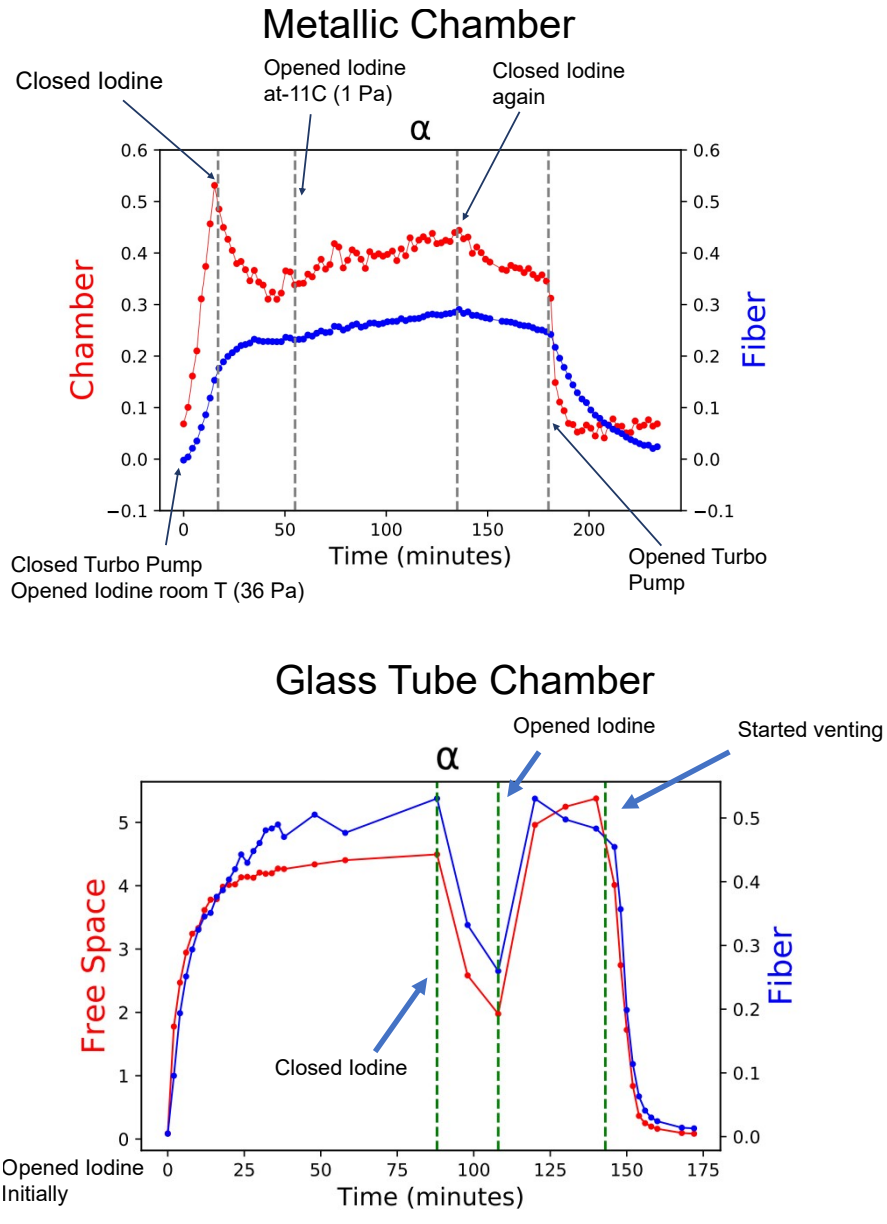

Figure 7.5: Iodine filling-time tests. Top plot shows the absorption coefficient α in the free space of the metallic chamber (red) and in the HCPCF (blue). We notice the two trajectories do not follow each other as closely as they do in the glass tube chamber setup, as depicted in the lower plot. This is most likely due to the iodine reacting with the metal walls and the sheer size of the metallic chamber. The absorption coefficient also reaches overall higher values in the glass tube, allowing us to achieve a better saturated absorption signal.

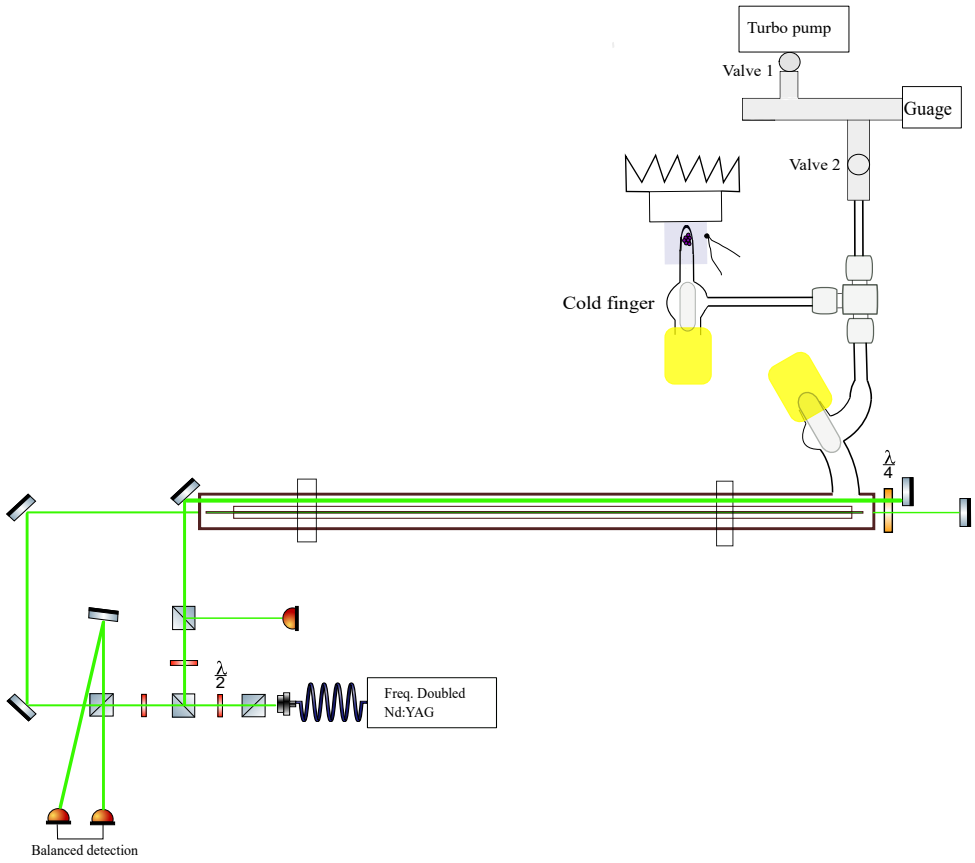

Figure 7.6: Schematic of the new glass tube chamber HCPCF setup. The laser is split on a PBS, with one beam path going through the HCPCF and the other through free space in the chamber. The iodine is cooled by a cold-point, allowing us to control the pressure. When we prepare to take data we close valve 2, and then open the Young valve, releasing iodine into the chamber. After waiting for the appropriate amount of filling time, $\approx$ 25 minutes, we begin scanning the laser frequency and taking traces of the photodetector signals on an oscilloscope.

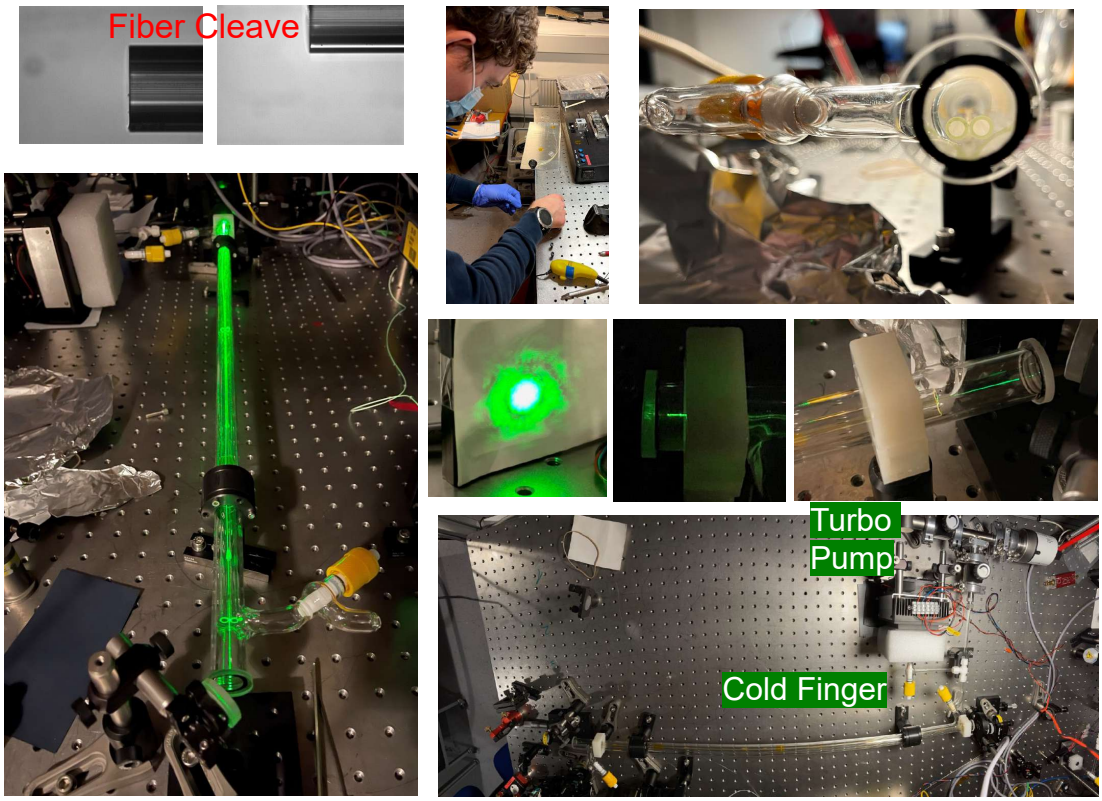

Figure 7.7: Collage of images from the glass tube chamber iodine setup. Top left: images of the fiber cleave with help of Erik Christensen. Top right: image looking down the tube where the HCPCF is placed. Middle image is of the TEM_{00} intensity profile after alignment. The rest of the images are of the overall setup.

7.3 Spectroscopy

In order to eliminate the Doppler broadening from our spectroscopic measurements, we retroreflect the laser back through the HCPCF. Iodine atoms with no velocity component along the beam direction are saturated by the forward laser beam. The retroreflected laser beam, which is the one we detect, experiences less absorption at the frequency addressing this zero-velocity class, a feature known as the Lamb-dip.

There are various contributions to the linewidth we measure as we scan the laser across a Lamb-dip. In this section we briefly describe the most significant contributions and provide an estimation of each one.

The natural linewidth is given by the $\gamma_{\text{nat}} \approx \frac{1}{2\pi\tau}$ =160 kHz, where $\tau \approx 1$ μs is the natural lifetime of the excited state.

As a molecule traverses a Gaussian beam profile, the interaction time limits how narrow the feature can be. This is called transit time broadening, and for a Gaussian beam profile, it is given by $\gamma_{tt} \approx 0.2\frac{v}{w} = 3.4$ MHz, where v is the mean velocity of the molecule passing through a Gaussian beam waist w [103]. This contribution depends on the width of our HCPCF and since our atoms are at room temperature in the fiber, we do not have the ability to adjust this effect.

Inelastic collisions introduce another factor affecting excited state lifetimes, known as pressure broadening. For transitions near 532 nm, pressure broadening has been quantified in the range of approximately 60-100 kHz/Pa, as documented in several studies [117–119]. Additionally, background gases can contribute to broadening, and this effect tends to intensify with longer waiting times. Hence, it is imperative to acquire data within a reasonable time frame after loading the iodine.

Another parameter which we can adjust is the optical power, which when increased leads to higher signal size, but also to power broadening given by,

$$\gamma = \gamma_0 \sqrt{1 + I/I_{\text{sat}}} \tag{7.2}$$

where γ is the FWHM of the hyperfine transition, γ_0 is the zero-power FWHM, including all of the contributions. I is the intensity used and I_{sat} is the saturation intensity. I_{sat} is a value which depends on the pressure, and is usually found experimentally by measuring the power broadening for various intensities. $I = I_{\text{sat}}$ when the FWHM is increased by a factor of $\sqrt{2}$.

The complete Doppler broadened width is the sum of all 15 hyperfine components centered at their specific detunings and is $\Delta\nu_D \approx 435$ MHz for iodine at room temperature [120]. We show a scan across the full Doppler broadened width in Fig. 7.8. We chose to focus our studies on the a1 component, which is circled, because it is the most separated from the rest. Some of the other hyperfine components are very close to each other, and broadening effects from one can distort the linewidth of another.

To measure the width of our feature, we need to calibrate the data's time axis to a frequency axis. This is done by modulating the frequency of the laser by 4 MHz, at 1 kHz. This gives us two data traces, and the time difference between corresponding a1 peaks of these traces corresponds to a frequency difference of 4 MHz. This conversion makes it possible to determine the width of the feature.

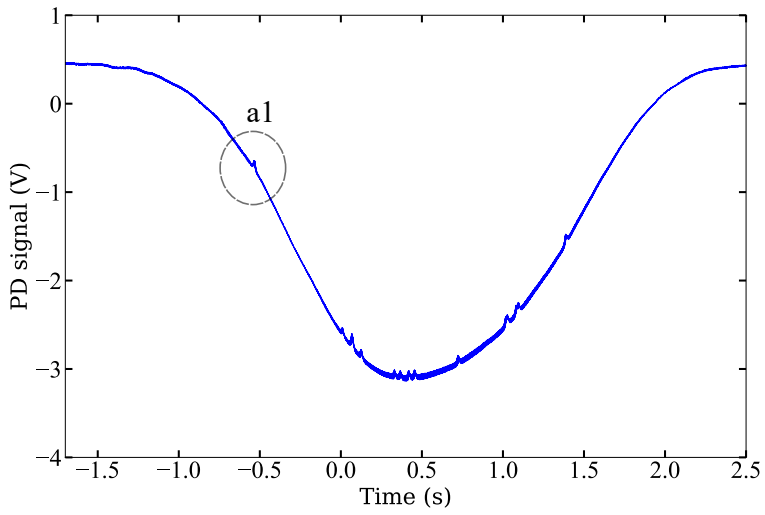

Figure 7.8: Transmission measured on a balanced photodetector of the retroreflected laser at 532 nm as we scan the laser frequency across the complete Doppler broadened R(56)32-0 transition. We focus our investigations on the a1 component since it is the most separated from the others.

7.4 Optimizing spectroscopic signal for frequency stabilization

For laser stabilization, one must convert a narrow feature in frequency space to an error signal, which can be used to feedback on a laser frequency. The achievable instability of a frequency standard is determined by the ratio between the slope of the error signal and the noise level in the detection. The SNR of a locking scheme can be written as [121],

$$SNR \propto \frac{A_{a_1}}{\Delta\omega} \frac{1}{\sqrt{P_{a_1}}} \tag{7.3}$$

where A_{a_1} is the voltage signal amplitude of the a1 component on the detector. P_{a_1} is the signal of the detected power at the a1 component, with square-root giving the shot-noise of the measurement. $\Delta\omega$ is the FWHM of the a1 component. To search for optimal parameters for an error signal, we plot SNR versus power before the HCPCF in Fig. 7.9, for six different loaded iodine pressures. We notice that the peak SNR appears to increase for increasing pressure. The power producing the optimal SNR also increases for higher pressures. This makes sense because higher pressures require increased intensities to achieve saturation.

In addition to SNR, we investigate the FWHM linewidth, fractional hole depth, and percent of transmitted light for various pressures and powers, plotted in Fig. 7.11. In Fig. 7.11a, the zero-power linewidth is dependent on the pressure, and is

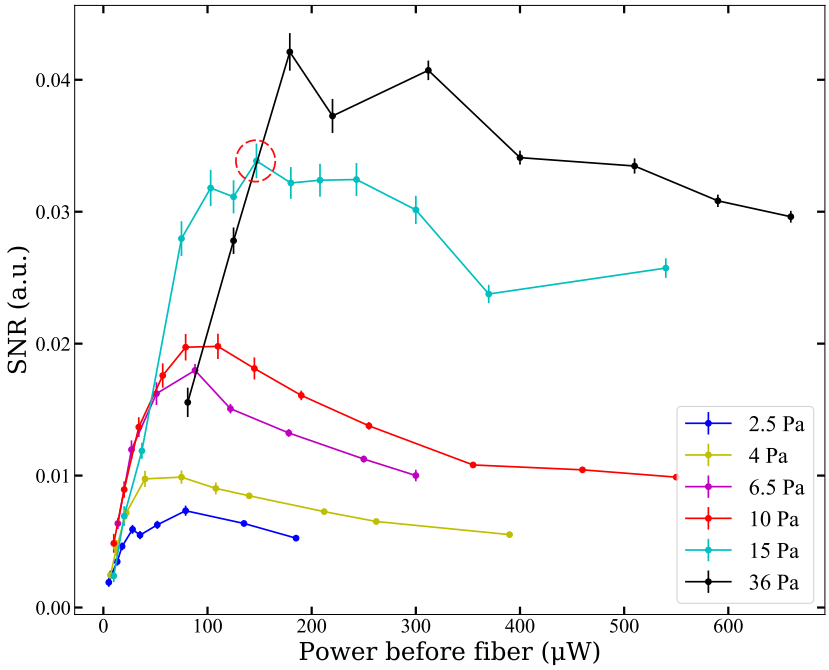

Figure 7.9: SNR versus power before the fiber, tested at six different iodine pressures. This plot suggests we can reach higher SNR of our locking signal by using higher pressures of iodine. The red dotted-circle surrounds the data point we investigate further in Fig. 7.12.

further broadened as the power is increased. The fraction hole depth is the percent change in α due to the presence of the hyperfine feature and can be written as,

$$\frac{\Delta\alpha}{\alpha} = \frac{\alpha_{off} - \alpha_{on}}{\alpha_{off}} \tag{7.4}$$

where α_{on} corresponds to the absorption coefficient when the Lamb dip is present, and α_{off} corresponds to the extrapolated absorption level without the Lamb dip, and is elucidated by Fig. 7.10.

Percent transmitted is how much of the intensity is transmitted at the location of the a1 component, compared to the off-resonance case. We see that for higher pressures, around 10% transmitted at the a1 component. In a trace such as the one depicted in Fig. 7.12, the bottom of the Doppler broadened spectrum can not be detected. Because of the high iodine pressure, there is so much absorption in this region that no light is transmitted.

We have highlighted an example data point in Fig. 7.9, and its corresponding scan and lineshape are illustrated in Fig. 7.12. We selected this data point at a pressure of 15 Pa for analysis. The reason being that the data from 36 Pa, while potentially higher in SNR, is acquired at room temperature with the cold-point deactivated. Operating under such pressure could make our measurements highly

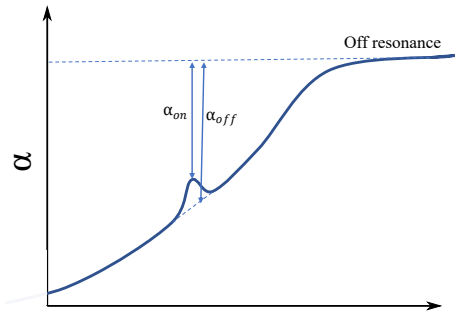

Figure 7.10: Inset illustration showing fractional hole depth. This value is the fractional change in α due to the hyperfine component.

susceptible to lab temperature variations. Thus, it is preferable to work under conditions where we can regulate the temperature. After removing the linear background due to Doppler broadening, we determined the Lorentzian linewidth to be 6.50(2) MHz.

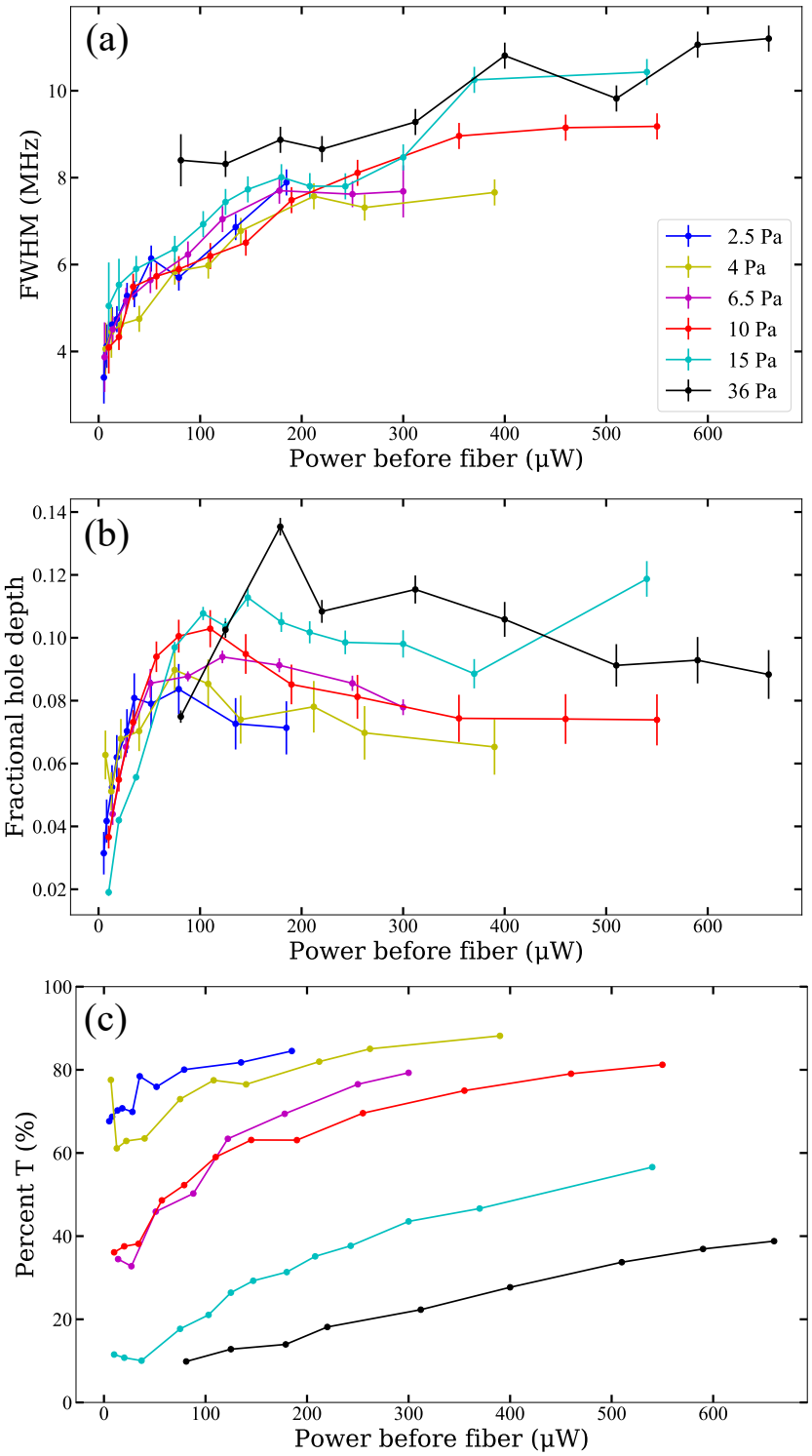

Figure 7.11: Quantities describing our Lamb-dip spectroscopic measurement for various powers at six different iodine pressures. (a) FWHM versus power. (b) Fractional hole depth versus power. (c) Percent of light transmitted at the a1 component versus power.

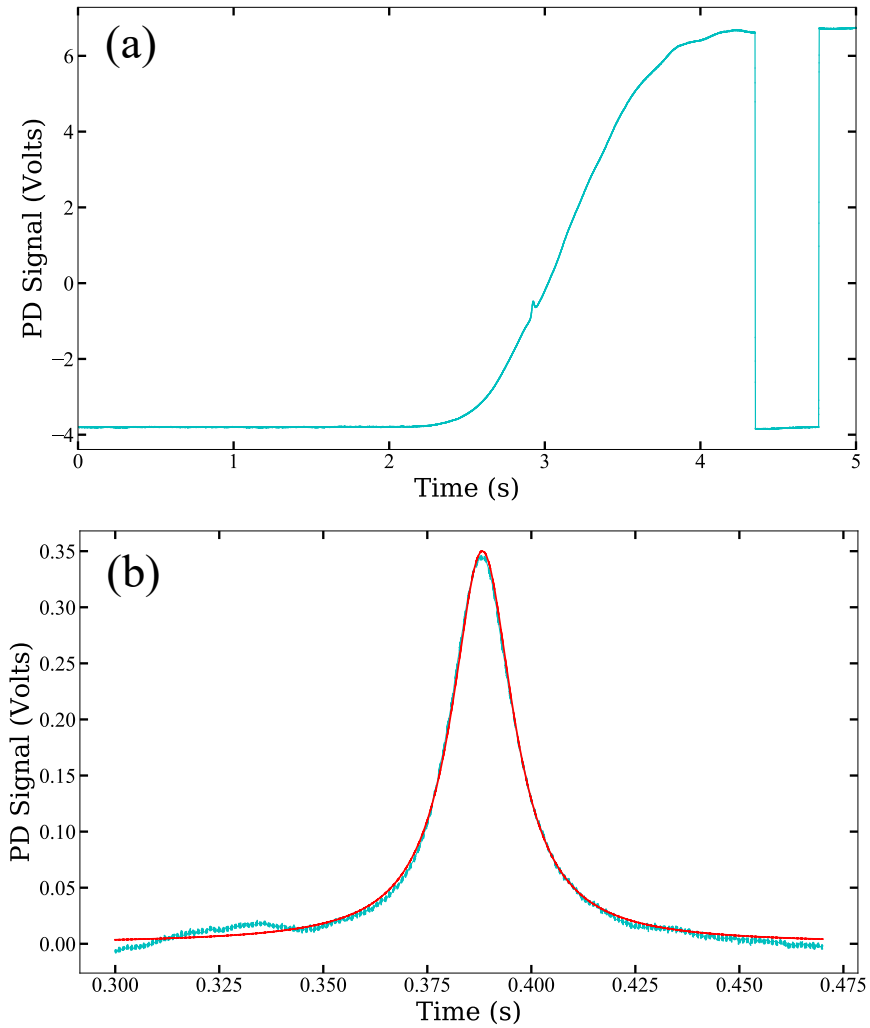

Figure 7.12: Oscilloscope trace of the circled data point in Fig. 7.9, which is potentially interesting for laser stabilization. (a) Oscilloscope trace as we scan the laser across resonance, with the laser beam completely blocked at the end of the trace to locate the zero-point on the balanced detection. (b) Lorentzian fit to the a1 component after removing a linear background. The FWHM is measured to be 6.50(2) MHz.

7.5 Outlook

We plan to attempt locking a laser to a hyperfine component and conducting a beat experiment with another laser locked to a bulk cell. The bulk cell system is expected to outperform the HCPCF because it exhibits a much lower transit time broadening. The goal is to achieve a significantly lower fractional frequency instability than 2×10^{-12} at 1s, as presented in Lurie's inspiring work [116]. They claim they were limited in their ability to load controlled pressures of iodine with little background gas. They had to increase their power to compensate for the high background gas pressure. In their beat measurement, they reported used a heavily power broadened linewidth with a FWHM of 15 MHz.

We estimate the broadening contributions to our linewidth in Fig. 7.12 in Table 7.1. Most likely we will try out a few possibilities to see which leads to the best Allan deviation. Our ability to achieve a low instability will depend on many factors, including locking technique, modulation frequency, feedback electronics, and the stability of our spectroscopic signal.

Broadening contributions	**Estimate $\Delta\nu$**
Natural lifetime	200 kHz
Transit time	3.4 MHz
Pressure - I_2	1.5 MHz
Pressure - other gases	150 kHz
Laser linewidth	10 kHz
Total low power linewidth	$\sim$ 5.3 MHz
Power broadened linewidth	6.5 MHz

Table 7.1: We list estimated contributions leading to our FWHM linewidth of 6.5 MHz, as in Fig. 7.12

CHAPTER 8

Conclusions and outlook

In this thesis, I described experimental upgrades and investigations on our cavity QED system, which couples ^{88}Sr atoms to a broad cavity. Our research is situated in the strong collective coupling and bad cavity regimes. Central to our exploration is the phenomenon of superradiance, which culminates in two research publications presented in chapters 5 and 6. These publications are studies based on the $^3P_1 \rightarrow {}^1S_0$ intercombination line in strontium with potential for application in metrology. This chapter serves as both a recapitulation of our journey and a prospective look into the future potential of this research.

8.1 Collectively enhanced Ramsey investigations

In this chapter, we successfully verified the presence of a superradiant threshold for atoms excited transversely to the cavity axis, and leveraged this feature in the demonstration of a collectively enhanced Ramsey lineshape. We demonstrated minimal heating in that each atom maximally gets two recoils per interrogation, allowing for numerous sequences within a MOT cycle and increasing repeatability. This result proposes an alternative population state readout, using only the photons directly emitted from the interrogated transition. The photons emitted are fast, directed, and this setup is simple, only requiring a cavity with appropriate parameters for the readout. There are a number of possible future paths with this investigation.

Since it is theoretically predicted that states excited below threshold are subradiant with respect to the cavity axis, one investigation is to measure this directly. Subradiant emission has suppressed cavity emittance compared to that of a spontaneously emitting cloud of atoms. Subradiance remains experimentally elusive [122–130], particularly for many particle systems due to its weak coupling to the environment. If it can be controlled, subradiance has proposed applications in quantum metrology and sensing [126], and also for efficient quantum memories and transport [127]. With our cavity cooperativity and atom number, spontaneous emission into the cavity mode is expected to be at $\sim$ 100 pW range. Directly measuring cavity subradiance would necessitate reliable detection of power below

this level. This would require an improved detection efficiency from the current setup.

In our investigation, we only employ free time evolution after the first $\pi/2$-pulse. However, provided the collective Bloch vector remains below the equator, other operations during this interval should be possible without initiating collective cavity decay. For example, a spin-echo or subsequent π-pulses before the final $\pi/2$-pulse could be applied to reduce Doppler broadening effects and improve the sensor. These spin-echos would need to have the appropriate phases such that the collective Bloch vector passes through the southern hemisphere of the Bloch sphere. These pulses can be applied from opposing directions in order to minimize heating. Torquing the collective Bloch vector above the equator is permissible if it is done at times much shorter than the inverse collective Rabi frequency because that is the rate at which atoms will start to superradiantly emit once above threshold.

Currently, our total time for experiments is limited to a few milliseconds due to Doppler dephasing and free-fall of our atomic ensemble. If the atoms were trapped in the Lamb-Dicke regime of an optical lattice, the available time for experiments would be extended. Spontaneous emission into modes external to the cavity would however continue to pose limitations.

The most clear challenge we must overcome for this method to be more competitive with other atom counting techniques is the shot-to-shot fluctuations in the superradiant pulses. While our investigation was a proof-of-principle demonstration of a new scheme, for it to be used in a real-time clock sequence, the SNR of the spectroscopic lineshape needs to be better understood.

Immediately after transverse excitation of an atomic ensemble, there is phase coherence along the pump beam. This results in the atoms emitting at an increased rate along the pump direction, although this emission is not enhanced by the cavity. Optimally, we want all of the photons to be read out of the cavity mode. To scramble the coherence along the pump direction, we could flash the blue MOT beams operating on the ${}^1S_0 \rightarrow {}^1P_1$ transition on for a very short period. This destroys the phase coherence between the ${}^1S_0$ and ${}^3P_1$ levels. While I have been writing my thesis, there have been some investigations testing this in our group. Although this method heats up the atoms with the blue photons, initial measurements seem promising for reducing fluctuations in the peak intensities of the emitted pulses.

If we really wanted to retain the phase coherence in the atoms, as is needed in a Ramsey scheme, one would need to conduct a series of controlled and reversible inhomogeneous broadening, or "CRIB", protocols, as they do in the field of quantum storage [131, 132]. This could be a magnetic field gradient or light shift gradient across the atoms along the pump direction. To implement such a technique, we could apply a CRIB operation after the first $\pi/2$-pulse, then we apply the opposite phase to reverse it before the second $\pi/2$-pulse, and then finally again after the final $\pi/2$-pulse.

A second contribution to the shot-to-shot fluctuations is the quality of our excitations. Looking at blue fluorescence after an optimized π-pulse, the atoms are only excited to roughly $90 \pm 5\%$. This causes very large fluctuations in the cavity pulses. We believe this variance is due to frequency noise or beam quality

of the 689 nm pump light. Although the light comes directly out of a fiber and has a Gaussian intensity profile, there is a long beam path including two injection lasers and a TA, all of which could add phase noise. Furthermore, the lock which stabilizes our 689 nm master laser has a feedback bandwidth of about 1 MHz, as seen by the servo bumps on our error signal. Since the superradiant emission has typical delay times of about 1 μs, our excitations need to be shorter than this. We may be adding significant noise at the relevant time scale. In the future it may improve the excitation quality to incorporate an extra filter cavity to remove the added noise from the servo bumps.

One option to reduce the fluctuations on the pulses which we have not yet delved into is applying a small amount of resonant light immediately following the pump pulse, thereby seeding the superradiant emission. This would initiate superradiance along the cavity mode faster than it takes for the atomic dipoles to synchronize without seeding. While this would affect the frequency of the pulses and imprint a phase on the superradiant emission, we are only interested in the peak intensities in this investigation.

If we can improve the SNR significantly, the new lineshape has some unique features for laser stabilization. As we have seen, the discriminator slope has the potential to be quite sharp, particularly if the collectively enhanced Ramsey fringe grows nonlinearly above threshold.

One possibility with this lineshape could be to step the excitation laser frequency, or phase, such that we interrogate directly on the kinks, as depicted in Fig. 8.1. In this scheme, a detected pulse indicates the laser frequency is not centered on resonance. Furthermore, this would impart less recoils on the atoms because we are interrogating the atoms in such a way that results in no excitation and zero superradiant emission. While this approach may be an experimentally challenging one in which we lock to a zero signal, there could be other possible schemes utilizing the new lineshape.

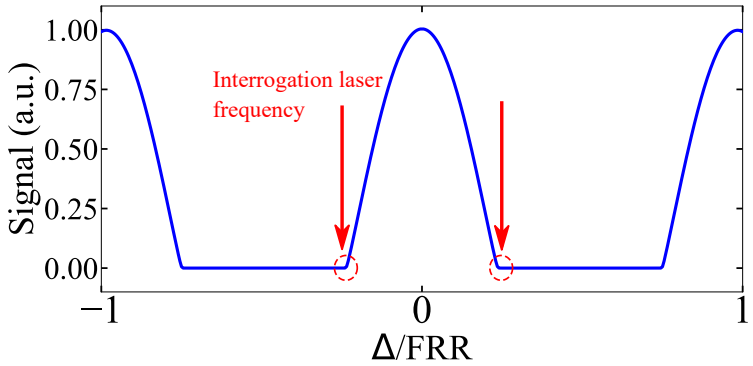

Figure 8.1: Collectively enhanced Ramsey lineshape simulation (blue) with potentially narrow stabilization features at the kinks of the fringes, designated by red arrows and dotted circles.

Ultimately, we want this method to be useful in a clock running on the truly narrow $^3P_0$ clock transition. While the 2 ms cooling periods were long compared to the natural lifetime of $^3P_1$, this duration would be very short compared to the

lifetime of $^3P_0$, and would highly mitigate the Dick effect in such a scenario.

Another approach could be to use a superradiant readout on the kHz line as a readout of the ground state population in a clock operating on the mHz transition. For this, we suggest placing a perpendicular "readout" cavity to the 1D magic wavelength lattice cavity. After an excitation attempt on $^3P_0$, to quickly read out the ground state population, apply an excitation pulse and measure the resulting superradiant emission on $^3P_1$. This is one way in which a superradiant pulsed readout could be used in a combination clock and it is imperative to compare various population readout methods.

8.2 Quasicontinuous superradiance investigations

The work presented in chapter 6 demonstrates superradiant pulses on the $^3P_1 \rightarrow {}^1S_0$ transition which is extended via repumping to last for several milliseconds. The system appears to reach a steady state lasing region and we observe a linewidth of 820 Hz over 1.1 ms, while maintaining an intensity of a few nW. This demonstrates a lasing linewidth of nearly an order of magnitude below the natural linewidth of the transition.

The linewidth of 820 Hz is far below the Doppler broadening of the atomic ensemble, which is estimated to be 90 kHz during lasing, and is consistent with the Fourier limit of a rectangular time window. This result shows great promise for narrow linewidth superradiant lasing.

The foundational work of Holland [40] posits that achieving what is termed the "Purcell limited linewidth" should be feasible with the correct repumping rate. For our system, the Purcell limited linewidth is projected to be $\Delta f = \mathcal{C}\gamma = 4$ Hz. To observe this, we would need to sustain steady state lasing for approximately 250 ms. This duration is more than two orders of magnitude longer than the capabilities of our current system.

The possibility of shelving atoms in $^3P_2$ has interesting prospects for simultaneous cooling and lasing of the atoms. $^3P_2$ has a lifetime of hundreds of seconds, and can therefore function as a relative ground state. There is a possible closed cooling transition from this state up to $5s4d^3D_3$ at 2.9 μm which has a linewidth of 50 kHz. Prior work has demonstrated the transition can be used to cool on a MOT, with Doppler temperature of 1.4 μK and the possibility of sub-Doppler cooling [133]. However, operating in the mid-infrared spectrum brings along its own set of experimental challenges. Specialized equipment, including specific windows, power meters, and cameras are required. Another possible cooling transition is from $^3P_2$ to $5s5d^3D_3$ at a wavelength of 497 nm [133]. Properties of this cooling transition are more similar to that of $^1P_1$, with a Doppler temperature of 230 μK. Although, this state has relatively large branching losses. Storing atoms in the long-lived $^3P_2$ appears to be the most plausible way to control the superradiant lasing for extended durations.

In general, it might not be worth it to reach lower linewidths in a quasicontinuous system. Our goal was to demonstrate linewidth narrowing, which is a promising result for a potential fully continuous system. In a fully continuous system, one must

replenish the excited atoms in the cavity mode. This requires spatial separation of cooling stages. To my knowledge, there are two leading efforts on this front working on the mHz transition: one at the University of Amsterdam (UvA) in the group of Florian Schreck, and the other at Joint Institute for Laboratory Astrophysics (JILA) in the group of James K. Thompson. Both groups plan to have a walking optical lattice in a ring cavity, replenishing cold excited atoms for continuous lasing. There is a second, fully continuous hot beam experiment in UvA working on the kHz transition in strontium based on the work of Liu et al. [95]. Furthermore, experiments on the kHz transition with a continuous cold beam of atoms with a deflection are being set up in our group and at the Laser Physics Laboratory (Paris North University). Continuous clock operation, without a phase slip, allows for a frequency instability that averages down as $1/\tau$ rather than $1/\sqrt{\tau}$. Moreover, an active clock with small pulling coefficients would be very beneficial in high-noise environments, including space missions.

Directly competing with state-of-the-art clocks will be challenging, especially given an unavoidable light shift on the ground state during repumping. There may be innovative methods to allow only one photon per atom to contribute to the lasing, thereby not requiring repumping while the atoms are lasing.

If all systematic effects influencing the frequency can be precisely controlled or calculated, the system might retain its stability. Whether a continuous superradiant laser will operate as a full-fledged clock or simply stand as a stable and resilient reference laser will only be clear as the research continues to develop.

As we step forward, it is clear that the domain of superradiance holds immense promise. The richness and dynamism of this field make it a particularly enticing avenue of research in the foreseeable future.

Bibliography

[1] Mark Notcutt, Longsheng Ma, Jun Ye, and John Hall. Simple and compact 1-hz laser system via an improved mounting configuration of a reference cavity. *Optics letters*, 30:1815–7, 08 2005. doi: 10.1364/OL.30.001815.

[2] B. C. Young, F. C. Cruz, W. M. Itano, and J. C. Bergquist. Visible lasers with subhertz linewidths. *Phys. Rev. Lett.*, 82:3799–3802, May 1999. doi: 10.1103/PhysRevLett.82.3799. URL `https://link.aps.org/doi/10.1103/PhysRevLett.82.3799`.

[3] S. A. Webster, M. Oxborrow, and P. Gill. Vibration insensitive optical cavity. *Phys. Rev. A*, 75:011801, Jan 2007. doi: 10.1103/PhysRevA.75.011801. URL `https://link.aps.org/doi/10.1103/PhysRevA.75.011801`.

[4] M. Eichenseer, A.Yu. Nevsky, J. von Zanthier, and H. Walther. A nd:yag laser with short term frequency stability at the hertz level. In *2003 European Quantum Electronics Conference. EQEC 2003 (IEEE Cat No.03TH8665)*, pages 241–, 2003. doi: 10.1109/EQEC.2003.1314098.

[5] Garrett D. Cole, Wei Zhang, Michael J. Martin, Jun Ye, and Markus Aspelmeyer. Tenfold reduction of Brownian noise in high-reflectivity optical coatings. *Nature Photonics*, 7(8):644–650, Aug 2013. ISSN 1749-4893. doi: 10.1038/nphoton.2013.174. URL `https://doi.org/10.1038/nphoton.2013.174`.

[6] J. Prestage, S. Chung, R. Thompson, and P. MacNeal. Frequency control symposium, 2009 joint with the 22nd european frequency and time forum. In *Frequency Control Symposium, 2009 Joint with the 22nd European Frequency and Time forum. IEEE International*, pages 54–57, New York, 2009. IEEE.

[7] M. Weiss, P. Shome, and R. Beard. Proceedings of the 42nd annual precise time and time interval (ptti) meeting. page 465, Washington, 2010. USNO. URL `http://tycho.usno.navy.mil/ptti/2010papers/paper37.pdf`.

[8] Ruxandra Bondarescu, Mihai Bondarescu, György Heté nyi, Lapo Boschi, Philippe Jetzer, and Jayashree Balakrishna. Geophysical applicability of atomic clocks: direct continental geoid mapping. *Geophysical Journal International*, 191(1):78–82, aug 2012. doi: 10.1111/j.1365-246x.2012.05636.x. URL `https://doi.org/10.1111%2Fj.1365-246x.2012.05636.x`.

[9] Gérard Petit and Peter Wolf. Relativistic theory for time comparisons: a review. *Metrologia*, 42(3):S138, jun 2005. doi: 10.1088/0026-1394/42/3/S14. URL `https://dx.doi.org/10.1088/0026-1394/42/3/S14`.

[10] M. Soffel, S. A. Klioner, G. Petit, P. Wolf, S. M. Kopeikin, P. Bretagnon, V. A. Brumberg, N. Capitaine, T. Damour, T. Fukushima, B. Guinot, T.-Y. Huang, L. Lindegren, C. Ma, K. Nordtvedt, J. C. Ries, P. K. Seidelmann, D. Vokrouhlický, C. M. Will, and C. Xu. The IAU 2000 resolutions for astrometry, celestial mechanics, and metrology in the relativistic framework: Explanatory supplement. *The Astronomical Journal*, 126(6):2687, dec 2003. doi: 10.1086/378162. URL `https://dx.doi.org/10.1086/378162`.

[11] R. M. Godun, P. B. R. Nisbet-Jones, J. M. Jones, S. A. King, L. A. M. Johnson, H. S. Margolis, K. Szymaniec, S. N. Lea, K. Bongs, and P. Gill. Frequency ratio of two optical clock transitions in $^{171}yb^{+}$ and constraints on the time variation of fundamental constants. *Phys. Rev. Lett.*, 113: 210801, Nov 2014. doi: 10.1103/PhysRevLett.113.210801. URL `https://link.aps.org/doi/10.1103/PhysRevLett.113.210801`.

[12] S N Lea. Limits to time variation of fundamental constants from comparisons of atomic frequency standards. *Reports on Progress in Physics*, 70(9):1473, aug 2007. doi: 10.1088/0034-4885/70/9/R01. URL `https://dx.doi.org/10.1088/0034-4885/70/9/R01`.

[13] E. Reinhold, R. Buning, U. Hollenstein, A. Ivanchik, P. Petitjean, and W. Ubachs. Indication of a cosmological variation of the proton-electron mass ratio based on laboratory measurement and reanalysis of h_2 spectra. *Phys. Rev. Lett.*, 96:151101, Apr 2006. doi: 10.1103/PhysRevLett.96.151101. URL `https://link.aps.org/doi/10.1103/PhysRevLett.96.151101`.

[14] S. G. Karshenboim, V. V. Flambaum, and E. Peik. *Handbook of Atomic, Molecular and Optical Physics*, page 455. Springer, New York, 2005.

[15] Theodor W. Hänsch. Nobel lecture: Passion for precision. *Rev. Mod. Phys.*, 78:1297–1309, Nov 2006. doi: 10.1103/RevModPhys.78.1297. URL `https://link.aps.org/doi/10.1103/RevModPhys.78.1297`.

[16] Nathalie Picqué and Theodor W. Hänsch. Frequency comb spectroscopy. *Nature Photonics*, 13(3):146–157, Mar 2019. ISSN 1749-4893. doi: 10.1038/s41566-018-0347-5. URL `https://doi.org/10.1038/s41566-018-0347-5`.

[17] D.W. Allan. Statistics of atomic frequency standards. *Proceedings of the IEEE*, 54(2):221–230, 1966. doi: 10.1109/PROC.1966.4634.

[18] J. Rutman. Characterization of phase and frequency instabilities in precision frequency sources: Fifteen years of progress. *Proceedings of the IEEE*, 66(9): 1048–1075, 1978. doi: 10.1109/PROC.1978.11080.

[19] Hans G. Dehmelt. Monoion oscillator as potential ultimate laser frequency standard. *IEEE Transactions on Instrumentation and Measurement*, IM-31 (2):83–87, 1982. doi: 10.1109/TIM.1982.6312526.

[20] G. J. Dick. Local oscillator induced instabilities in trapped ion frequency standards. *Proceedings of the 34th Annual Precise Time and Time Interval Systems and Applications Meeting (ION, 1987)*, pages 133–147, 1987. URL ;https://tycho.usno.navy.mil/ptti/1987papers/Vol%2019_13.pdf.

[21] C. W. Chou, D. B. Hume, M. J. Thorpe, D. J. Wineland, and T. Rosenband. Quantum coherence between two atoms beyond $q = 10^{15}$. *Phys. Rev. Lett.*, 106:160801, Apr 2011. doi: 10.1103/PhysRevLett.106.160801. URL https://link.aps.org/doi/10.1103/PhysRevLett.106.160801.

[22] Masao Takamoto, Tetsushi Takano, and Hidetoshi Katori. Frequency comparison of optical lattice clocks beyond the dick limit. *Nature Photonics*, 5 (5):288–292, May 2011. ISSN 1749-4893. doi: 10.1038/nphoton.2011.34. URL https://doi.org/10.1038/nphoton.2011.34.

[23] T. L. Nicholson, M. J. Martin, J. R. Williams, B. J. Bloom, M. Bishof, M. D. Swallows, S. L. Campbell, and J. Ye. Comparison of two independent sr optical clocks with 1×10^{-17} stability at 10^3 s. *Phys. Rev. Lett.*, 109: 230801, Dec 2012. doi: 10.1103/PhysRevLett.109.230801. URL https://link.aps.org/doi/10.1103/PhysRevLett.109.230801.

[24] G. W. Biedermann, K. Takase, X. Wu, L. Deslauriers, S. Roy, and M. A. Kasevich. Zero-dead-time operation of interleaved atomic clocks. *Phys. Rev. Lett.*, 111:170802, Oct 2013. doi: 10.1103/PhysRevLett.111.170802. URL https://link.aps.org/doi/10.1103/PhysRevLett.111.170802.

[25] N. Hinkley, J. A. Sherman, N. B. Phillips, M. Schioppo, N. D. Lemke, K. Beloy, M. Pizzocaro, C. W. Oates, and A. D. Ludlow. An atomic clock with 10¡sup¿–18¡/sup¿ instability. *Science*, 341(6151):1215–1218, 2013. doi: 10.1126/science.1240420. URL https://www.science.org/doi/abs/10.1126/science.1240420.

[26] Andrew D. Ludlow, Martin M. Boyd, Jun Ye, E. Peik, and P. O. Schmidt. Optical atomic clocks. *Rev. Mod. Phys.*, 87:637–701, Jun 2015. doi: 10.1103/RevModPhys.87.637. URL https://link.aps.org/doi/10.1103/RevModPhys.87.637.

[27] S. L. Campbell, R. B. Hutson, G. E. Marti, A. Goban, N. Darkwah Oppong, R. L. McNally, L. Sonderhouse, J. M. Robinson, W. Zhang, B. J. Bloom, and J. Ye. A fermi-degenerate three-dimensional optical lattice clock. *Science*, 358(6359):90–94, 2017. doi: 10.1126/science.aam5538. URL https://www.science.org/doi/abs/10.1126/science.aam5538.

[28] S. M. Brewer, J.-S. Chen, A. M. Hankin, E. R. Clements, C. W. Chou, D. J. Wineland, D. B. Hume, and D. R. Leibrandt. $^{27}al^{+}$ quantum-logic clock with

a systematic uncertainty below 10^{-18}. *Phys. Rev. Lett.*, 123:033201, Jul 2019. doi: 10.1103/PhysRevLett.123.033201. URL https://link.aps.org/doi/10.1103/PhysRevLett.123.033201.

[29] W. F. McGrew, X. Zhang, R. J. Fasano, S. A. Schäffer, K. Beloy, D. Nicolodi, R. C. Brown, N. Hinkley, G. Milani, M. Schioppo, T. H. Yoon, and A. D. Ludlow. Atomic clock performance enabling geodesy below the centimetre level. *Nature*, 564(7734):87–90, Dec 2018. ISSN 1476-4687. doi: 10.1038/s41586-018-0738-2. URL https://doi.org/10.1038/s41586-018-0738-2.

[30] B. J. Bloom, T. L. Nicholson, J. R. Williams, S. L. Campbell, M. Bishof, X. Zhang, W. Zhang, S. L. Bromley, and J. Ye. An optical lattice clock with accuracy and stability at the 10^{18} level. *Nature*, 506(7486):71–75, Feb 2014. ISSN 1476-4687. doi: 10.1038/nature12941. URL https://doi.org/10.1038/nature12941.

[31] Ichiro Ushijima, Masao Takamoto, Manoj Das, Takuya Ohkubo, and Hidetoshi Katori. Cryogenic optical lattice clocks. *Nat. Photon.*, 9(3):185–189, Mar 2015. ISSN 1749-4893. doi: 10.1038/nphoton.2015.5. URL https://doi.org/10.1038/nphoton.2015.5.

[32] N. Huntemann, C. Sanner, B. Lipphardt, Chr. Tamm, and E. Peik. Single-ion atomic clock with 3×10^{-18} systematic uncertainty. *Phys. Rev. Lett.*, 116:063001, Feb 2016. doi: 10.1103/PhysRevLett.116.063001. URL https://link.aps.org/doi/10.1103/PhysRevLett.116.063001.

[33] Tanja E Mehlstäubler, Gesine Grosche, Christian Lisdat, Piet O Schmidt, and Heiner Denker. Atomic clocks for geodesy. *Reports on Progress in Physics*, 81(6):064401, apr 2018. doi: 10.1088/1361-6633/aab409. URL https://doi.org/10.1088%2F1361-6633%2Faab409.

[34] Tobias Bothwell, Colin J. Kennedy, Alexander Aeppli, Dhruv Kedar, John M. Robinson, Eric Oelker, Alexander Staron, and Jun Ye. Resolving the gravitational redshift across a millimetre-scale atomic sample. *Nature*, 602(7897):420–424, Feb 2022. ISSN 1476-4687. doi: 10.1038/s41586-021-04349-7. URL https://doi.org/10.1038/s41586-021-04349-7.

[35] D.D. McCarthy and K.P. Seidelmann. *Time: From Earth Rotation to Atomic Physics*. John Wiley & Sons, Hoboken, 2009.

[36] Yoshiyuki Tanaka and Hidetoshi Katori. Exploring potential applications of optical lattice clocks in a plate subduction zone. *Journal of Geodesy*, 95(8):93, August 2021. doi: 10.1007/s00190-021-01548-y.

[37] C. J. Foot. *Atomic Physics*, volume 11. Oxford University Press, Oxford, 2005.

[38] Norman F. Ramsey. A molecular beam resonance method with separated oscillating fields. *Phys. Rev.*, 78:695–699, Jun 1950. doi: 10.1103/PhysRev.78.695. URL https://link.aps.org/doi/10.1103/PhysRev.78.695.

[39] Michael J. Martin. *Quantum Metrology and Many-Body Physics: Pushing the Frontier of the Optical Lattice Clock*. PhD thesis, 2013. URL https://jila.colorado.edu/sites/default/files/2019-04/MJMartinThesisFinal_April%202013.pdf.

[40] D. Meiser, Jun Ye, D. R. Carlson, and M. J. Holland. Prospects for a millihertz-linewidth laser. *Phys. Rev. Lett.*, 102:163601, Apr 2009. doi: 10.1103/PhysRevLett.102.163601. URL https://link.aps.org/doi/10.1103/PhysRevLett.102.163601.

[41] D. Meiser and M. J. Holland. Steady-state superradiance with alkaline-earth-metal atoms. *Phys. Rev. A*, 81:033847, Mar 2010. doi: 10.1103/PhysRevA.81.033847. URL https://link.aps.org/doi/10.1103/PhysRevA.81.033847.

[42] D. Meiser and M. J. Holland. Intensity fluctuations in steady-state superradiance. *Phys. Rev. A*, 81:063827, Jun 2010. doi: 10.1103/PhysRevA.81.063827. URL https://link.aps.org/doi/10.1103/PhysRevA.81.063827.

[43] H. M. Goldenberg, D. Kleppner, and N. F. Ramsey. Atomic hydrogen maser. *Phys. Rev. Lett.*, 5:361–362, Oct 1960. doi: 10.1103/PhysRevLett.5.361. URL https://link.aps.org/doi/10.1103/PhysRevLett.5.361.

[44] J. E. Sansonetti and G. Nave. Wavelengths, Transition Probabilities, and Energy Levels for the Spectrum of Neutral Strontium (SrI). *Journal of Physical and Chemical Reference Data*, 39(3):033103, 08 2010. ISSN 0047-2689. doi: 10.1063/1.3449176. URL https://doi.org/10.1063/1.3449176.

[45] P. G. Mickelson, Y. N. Martinez, A. D. Saenz, S. B. Nagel, Y. C. Chen, T. C. Killian, P. Pellegrini, and R. Côté. Spectroscopic determination of the s-wave scattering lengths of ^{86}Sr and ^{88}Sr. *Phys. Rev. Lett.*, 95:223002, Nov 2005. doi: 10.1103/PhysRevLett.95.223002. URL https://link.aps.org/doi/10.1103/PhysRevLett.95.223002.

[46] Juan A. Muniz, Dylan J. Young, Julia R. K. Cline, and James K. Thompson. Cavity-qed measurements of the ^{87}Sr millihertz optical clock transition and determination of its natural linewidth. *Phys. Rev. Res.*, 3:023152, May 2021. doi: 10.1103/PhysRevResearch.3.023152. URL https://link.aps.org/doi/10.1103/PhysRevResearch.3.023152.

[47] A. V. Taichenachev, V. I. Yudin, C. W. Oates, C. W. Hoyt, Z. W. Barber, and L. Hollberg. Magnetic field-induced spectroscopy of forbidden optical transitions with application to lattice-based optical atomic clocks. *Phys. Rev. Lett.*, 96:083001, Mar 2006. doi: 10.1103/PhysRevLett.96.083001. URL https://link.aps.org/doi/10.1103/PhysRevLett.96.083001.

[48] Alexandre Cooper, Jacob P. Covey, Ivaylo S. Madjarov, Sergey G. Porsev, Marianna S. Safronova, and Manuel Endres. Alkaline-earth atoms in optical tweezers. *Phys. Rev. X*, 8:041055, Dec 2018. doi: 10.1103/PhysRevX.8.041055. URL https://link.aps.org/doi/10.1103/PhysRevX.8.041055.

[49] C W Bauschlicher Jr, S R Langhoff, and H Partridge. The radiative lifetime of the $^1D_2$ state of Ca and Sr: a core-valence treatment. *Journal of Physics B: Atomic and Molecular Physics*, 18(8):1523, apr 1985. doi: 10.1088/0022-3700/18/8/011. URL https://dx.doi.org/10.1088/0022-3700/18/8/011.

[50] Masami Yasuda and Hidetoshi Katori. Lifetime measurement of the $^3P_2$ metastable state of strontium atoms. *Phys. Rev. Lett.*, 92:153004, Apr 2004. doi: 10.1103/PhysRevLett.92.153004. URL https://link.aps.org/doi/10.1103/PhysRevLett.92.153004.

[51] Xinye Xu, Thomas H. Loftus, John L. Hall, Alan Gallagher, and Jun Ye. Cooling and trapping of atomic strontium. *J. Opt. Soc. Am. B*, 20(5):968–976, May 2003. doi: 10.1364/JOSAB.20.000968. URL https://opg.optica.org/josab/abstract.cfm?URI=josab-20-5-968.

[52] Martin M. Boyd, Tanya Zelevinsky, Andrew D. Ludlow, Sebastian Blatt, Thomas Zanon-Willette, Seth M. Foreman, and Jun Ye. Nuclear spin effects in optical lattice clocks. *Phys. Rev. A*, 76:022510, Aug 2007. doi: 10.1103/PhysRevA.76.022510. URL https://link.aps.org/doi/10.1103/PhysRevA.76.022510.

[53] R. H. Dicke. Coherence in spontaneous radiation processes. *Phys. Rev.*, 93:99–110, Jan 1954. doi: 10.1103/PhysRev.93.99. URL https://link.aps.org/doi/10.1103/PhysRev.93.99.

[54] M. Gross and S. Haroche. Superradiance: An essay on the theory of collective spontaneous emission. *Physics Reports*, 93(5):301–396, 1982. ISSN 0370-1573. doi: https://doi.org/10.1016/0370-1573(82)90102-8. URL https://www.sciencedirect.com/science/article/pii/0370157382901028.

[55] Michael Scheibner, Thomas Schmidt, Lukas Worschech, Alfred Forchel, Gerd Bacher, Thorsten Passow, and Detlef Hommel. Superradiance of quantum dots. *Nature Physics*, 3(2):106–110, Feb 2007. ISSN 1745-2481. doi: 10.1038/nphys494. URL https://doi.org/10.1038/nphys494.

[56] S. J. Roof, K. J. Kemp, M. D. Havey, and I. M. Sokolov. Observation of single-photon superradiance and the cooperative Lamb shift in an extended sample of cold atoms. *Phys. Rev. Lett.*, 117:073003, Aug 2016. doi: 10.1103/PhysRevLett.117.073003. URL https://link.aps.org/doi/10.1103/PhysRevLett.117.073003.

[57] E. M. Kessler, S. Yelin, M. D. Lukin, J. I. Cirac, and G. Giedke. Optical superradiance from nuclear spin environment of single-photon emitters. *Phys. Rev. Lett.*, 104:143601, Apr 2010. doi: 10.1103/PhysRevLett.104.143601. URL https://link.aps.org/doi/10.1103/PhysRevLett.104.143601.

[58] A. Goban, C.-L. Hung, J. D. Hood, S.-P. Yu, J. A. Muniz, O. Painter, and H. J. Kimble. Superradiance for atoms trapped along a photonic crystal waveguide. *Phys. Rev. Lett.*, 115:063601, Aug 2015. doi: 10.1103/PhysRevLett.

115.063601. URL https://link.aps.org/doi/10.1103/PhysRevLett.115.063601.

[59] Torben Laske, Hannes Winter, and Andreas Hemmerich. Pulse delay time statistics in a superradiant laser with calcium atoms. *Phys. Rev. Lett.*, 123:103601, Sep 2019. doi: 10.1103/PhysRevLett.123.103601. URL https://link.aps.org/doi/10.1103/PhysRevLett.123.103601.

[60] Eric Sierra, Stuart J. Masson, and Ana Asenjo-Garcia. Dicke superradiance in ordered lattices: Dimensionality matters. *Phys. Rev. Res.*, 4:023207, Jun 2022. doi: 10.1103/PhysRevResearch.4.023207. URL https://link.aps.org/doi/10.1103/PhysRevResearch.4.023207.

[61] S.J. Masson and A. Asenjo-Garcia. Universality of Dicke superradiance in arrays of quantum emitters. *Nat Commun*, 13:2285, 2022. doi: 10.1038/s41467-022-29805-4. URL https://doi.org/10.1038/s41467-022-29805-4.

[62] E.T. Jaynes and F.W. Cummings. Comparison of quantum and semiclassical radiation theories with application to the beam maser. *Proceedings of the IEEE*, 51:89–109, 1963.

[63] Zilong Chen, Justin G. Bohnet, Joshua M. Weiner, Kevin C. Cox, and James K. Thompson. Cavity-aided nondemolition measurements for atom counting and spin squeezing. *Phys. Rev. A*, 89:043837, Apr 2014. doi: 10.1103/PhysRevA.89.043837. URL https://link.aps.org/doi/10.1103/PhysRevA.89.043837.

[64] T. Holstein and Hl Primakoff. Field dependence of the intrinsic domain magnetization of a ferromagnet. *Physical Review*, 58:1098, 1940.

[65] Michael Tavis and Frederick W. Cummings. Exact solution for an n-molecule—radiation-field hamiltonian. *Phys. Rev.*, 170:379–384, Jun 1968. doi: 10.1103/PhysRev.170.379. URL https://link.aps.org/doi/10.1103/PhysRev.170.379.

[66] Jiazhong Hu, Wenlan Chen, Zachary Vendeiro, Hao Zhang, and Vladan Vuletić. Entangled collective-spin states of atomic ensembles under nonuniform atom-light interaction. *Phys. Rev. A*, 92:063816, Dec 2015. doi: 10.1103/PhysRevA.92.063816. URL https://link.aps.org/doi/10.1103/PhysRevA.92.063816.

[67] A. L. Schawlow and C. H. Townes. Infrared and optical masers. *Phys. Rev.*, 112(6):1940–1949, Dec 1958.

[68] H. J. Metcalf and P. van der Straten. *Laser Cooling and Trapping*. Springer Series on Atomic, Optical, and Plasma Physics. Springer, 1999.

[69] Daniel Barker. *Degenerate Gases of Strontium for Studies of Quantum Magnetism*. PhD thesis, 01 2016.

[70] Mikkel Tang. *Superradiant Lasers Based on Strontium-88*. PhD thesis, 2022. URL https://nbi.ku.dk/english/theses/phd-theses/mikkel-tang/Mikkel-tang.pdf.

[71] Matthew Norcia. *New Tools for Precision Measurement and Quantum Science with Narrow Linewidth Optical Transitions*. PhD thesis, 2017. URL https://scholar.colorado.edu/concern/graduate_thesis_or_dissertations/t435gc985.

[72] W.G. Nagourney. *Quantum Electronics for Atomic Physics and Telecommunication*. Oxford graduate texts. Oxford University Press, 2014. ISBN 9780199665488. URL https://books.google.dk/books?id=YDOTAwAAQBAJ.

[73] R. W. P. Drever, J. L. Hall, F. V. Kowalski, J. Hough, G. M. Ford, A. J. Munley, and H. Ward. Laser phase and frequency stabilization using an optical resonator. *Applied Physics B*, 31(2):97–105, Jun 1983. ISSN 1432-0649. doi: 10.1007/BF00702605. URL https://doi.org/10.1007/BF00702605.

[74] Eric D. Black. An introduction to Pound–Drever–Hall laser frequency stabilization. *American Journal of Physics*, 69(1):79–87, 01 2001. ISSN 0002-9505. doi: 10.1119/1.1286663. URL https://doi.org/10.1119/1.1286663.

[75] MOGLabs. *AN002: Pound-Drever-Hall Locking with the FSC*, 2017. URL https://www.moglabs.com/support/appnotes/an002-pdh-r2.pdf. Application Note AN002, Version R2.

[76] Long-Sheng Ma, Peter Jungner, Jun Ye, and John L. Hall. Delivering the same optical frequency at two places: accurate cancellation of phase noise introduced by an optical fiber or other time-varying path. *Opt. Lett.*, 19(21):1777–1779, Nov 1994. doi: 10.1364/OL.19.001777. URL https://opg.optica.org/ol/abstract.cfm?URI=ol-19-21-1777.

[77] Christian Hagemann, Christian Grebing, Christian Lisdat, Stephan Falke, Thomas Legero, Uwe Sterr, Fritz Riehle, Michael J. Martin, and Jun Ye. Ultrastable laser with average fractional frequency drift rate below $5 \times 10^{-19}/s$. *Opt. Lett.*, 39(17):5102–5105, Sep 2014. doi: 10.1364/OL.39.005102. URL https://opg.optica.org/ol/abstract.cfm?URI=ol-39-17-5102.

[78] S. Origlia, S. Schiller, M. S. Pramod, L. Smith, Y. Singh, W. He, S. Viswam, D. Świerad, J. Hughes, K. Bongs, U. Sterr, Ch. Lisdat, S. Vogt, S. Bize, J. Lodewyck, R. Le Targat, D. Holleville, B. Venon, P. Gill, G. Barwood, I. R. Hill, Y. Ovchinnikov, A. Kulosa, W. Ertmer, E.-M. Rasel, J. Stuhler, and W. Kaenders. Development of a strontium optical lattice clock for the SOC mission on the ISS. In Jürgen Stuhler and Andrew J. Shields, editors, *SPIE Proceedings*. SPIE, apr 2016. doi: 10.1117/12.2229473. URL https://doi.org/10.1117%2F12.2229473.

[79] Niamh Christina Jackson. *Rydberg spectroscopy and dressing in an ultracold strontium gas*. Durham theses, Durham University, 2018. URL http://etheses.dur.ac.uk/12825/.

[80] S. Snigirev, A. J. Park, A. Heinz, I. Bloch, and S. Blatt. Fast and dense magneto-optical traps for strontium. *Phys. Rev. A*, 99:063421, Jun 2019. doi: 10.1103/PhysRevA.99.063421. URL https://link.aps.org/doi/10.1103/PhysRevA.99.063421.

[81] Thomas H. Loftus, Tetsuya Ido, Martin M. Boyd, Andrew D. Ludlow, and Jun Ye. Narrow line cooling and momentum-space crystals. *Phys. Rev. A*, 70:063413, Dec 2004. doi: 10.1103/PhysRevA.70.063413. URL https://link.aps.org/doi/10.1103/PhysRevA.70.063413.

[82] H. J. Lewandowski, D. M. Harber, D. L. Whitaker, and E. A. Cornell. Simplified system for creating a Bose-Einstein condensate. *Journal of Low Temperature Physics*, 132:309–367, 2003. doi: 10.1023/A:1024800600621. Retrieved October 25, 2022.

[83] T. Pyragius. Developing and building an absorption imaging system for ultracold atoms, 2012. URL https://arxiv.org/abs/1209.3408. Retrieved October 25, 2022.

[84] Haruka Tanji-Suzuki, Ian D. Leroux, Monika H. Schleier-Smith, Marko Cetina, Andrew T. Grier, Jonathan Simon, and Vladan Vuletić. Chapter 4 - interaction between atomic ensembles and optical resonators: Classical description. 60:201–237, 2011. ISSN 1049-250X. doi: https://doi.org/10.1016/B978-0-12-385508-4.00004-8. URL https://www.sciencedirect.com/science/article/pii/B9780123855084000048.

[85] Ian D. Leroux, Monika H. Schleier-Smith, and Vladan Vuletić. Implementation of cavity squeezing of a collective atomic spin. *Phys. Rev. Lett.*, 104:073602, Feb 2010. doi: 10.1103/PhysRevLett.104.073602. URL https://link.aps.org/doi/10.1103/PhysRevLett.104.073602.

[86] M. G. Raizen, R. J. Thompson, R. J. Brecha, H. J. Kimble, and H. J. Carmichael. Normal-mode splitting and linewidth averaging for two-state atoms in an optical cavity. *Phys. Rev. Lett.*, 63:240–243, Jul 1989. doi: 10.1103/PhysRevLett.63.240. URL https://link.aps.org/doi/10.1103/PhysRevLett.63.240.

[87] Jérôme Lodewyck, Philip G. Westergaard, and Pierre Lemonde. Nondestructive measurement of the transition probability in a Sr optical lattice clock. *Phys. Rev. A*, 79:061401, Jun 2009. doi: 10.1103/PhysRevA.79.061401. URL https://link.aps.org/doi/10.1103/PhysRevA.79.061401.

[88] Christoph Hotter, Laurin Ostermann, and Helmut Ritsch. Cavity sub- and superradiance for transversely driven atomic ensembles. *Phys. Rev. Res.*, 5:013056, Jan 2023. doi: 10.1103/PhysRevResearch.5.013056. URL https://link.aps.org/doi/10.1103/PhysRevResearch.5.013056.

[89] Eliot Bohr, Sofus L. Kristensen, Christoph Hotter, Stefan Alaric Schäffer, Julian Robinson-Tait, Jan W. Thomsen, Tanya Zelevinsky, Helmut Ritsch, and Jörg Helge Müller. Collectively enhanced ramsey readout by cavity sub-to superradiant transition, 2023.

[90] Sofus Laguna Kristensen, Eliot Bohr, Julian Robinson-Tait, Tanya Zelevinsky, Jan W. Thomsen, and Jörg Helge Müller. Subnatural linewidth superradiant lasing with cold ^{88}Sr atoms. *Phys. Rev. Lett.*, 130:223402, May 2023. doi: 10.1103/PhysRevLett.130.223402. URL `https://link.aps.org/doi/10.1103/PhysRevLett.130.223402`.

[91] Justin G. Bohnet, Zilong Chen, Joshua M. Weiner, Kevin C. Cox, and James K. Thompson. Relaxation oscillations, stability, and cavity feedback in a superradiant raman laser. *Phys. Rev. Lett.*, 109:253602, Dec 2012. doi: 10.1103/PhysRevLett.109.253602. URL `https://link.aps.org/doi/10.1103/PhysRevLett.109.253602`.

[92] Fritz Riehle. *Atomic and Molecular Frequency References*. John Wiley I& Sons, Ltd, 2003. ISBN 9783527605996.

[93] Simon B. Jäger, Haonan Liu, John Cooper, Travis L. Nicholson, and Murray J. Holland. Superradiant emission of a thermal atomic beam into an optical cavity. *Phys. Rev. A*, 104:033711, Sep 2021. doi: 10.1103/PhysRevA.104.033711. URL `https://link.aps.org/doi/10.1103/PhysRevA.104.033711`.

[94] Matthew A. Norcia and James K. Thompson. Cold-strontium laser in the superradiant crossover regime. *Phys. Rev. X*, 6:011025, Mar 2016. doi: 10.1103/PhysRevX.6.011025. URL `https://link.aps.org/doi/10.1103/PhysRevX.6.011025`.

[95] Haonan Liu, Simon B. Jäger, Xianquan Yu, Steven Touzard, Athreya Shankar, Murray J. Holland, and Travis L. Nicholson. Rugged mhz-linewidth superradiant laser driven by a hot atomic beam. *Phys. Rev. Lett.*, 125:253602, Dec 2020. doi: 10.1103/PhysRevLett.125.253602. URL `https://link.aps.org/doi/10.1103/PhysRevLett.125.253602`.

[96] T. Ritari, J. Tuominen, H. Ludvigsen, J. C. Petersen, T. Sørensen, T. P. Hansen, and H. R. Simonsen. Gas sensing using air-guiding photonic bandgap fibers. *Opt. Express*, 12(17):4080–4087, Aug 2004. doi: 10.1364/OPEX.12.004080. URL `https://opg.optica.org/oe/abstract.cfm?URI=oe-12-17-4080`.

[97] Wei Jin, Yingchun Cao, Fan Yang, and Hoi Lut Ho. Ultra-sensitive all-fibre photothermal spectroscopy with large dynamic range. *Nature Communications*, 6(1):6767, Apr 2015. ISSN 2041-1723. doi: 10.1038/ncomms7767. URL `https://doi.org/10.1038/ncomms7767`.

[98] Amar Bhagwat and Alexander Gaeta. Nonlinear optics in hollow-core photonic bandgap fibers. *Optics express*, 16:5035–47, 04 2008. doi: 10.1364/OE.16.005035.

[99] P. St. J. Russell, P. Hölzer, W. Chang, A. Abdolvand, and J. C. Travers. Hollow-core photonic crystal fibres for gas-based nonlinear optics. *Nature Photonics*, 8(4):278–286, Apr 2014. ISSN 1749-4893. doi: 10.1038/nphoton.2013.312. URL https://doi.org/10.1038/nphoton.2013.312.

[100] Saikat Ghosh, Jay E. Sharping, Dimitre G. Ouzounov, and Alexander L. Gaeta. Resonant optical interactions with molecules confined in photonic band-gap fibers. *Phys. Rev. Lett.*, 94:093902, Mar 2005. doi: 10.1103/PhysRevLett.94.093902. URL https://link.aps.org/doi/10.1103/PhysRevLett.94.093902.

[101] Saikat Ghosh, Amar R. Bhagwat, C. Kyle Renshaw, Shireen Goh, Alexander L. Gaeta, and Brian J. Kirby. Low-light-level optical interactions with rubidium vapor in a photonic band-gap fiber. *Phys. Rev. Lett.*, 97:023603, Jul 2006. doi: 10.1103/PhysRevLett.97.023603. URL https://link.aps.org/doi/10.1103/PhysRevLett.97.023603.

[102] Rajesh Thapa, Kevin Knabe, Mohammed Faheem, Ahmer Naweed, Oliver L. Weaver, and Kristan L. Corwin. Saturated absorption spectroscopy of acetylene gas inside large-core photonic bandgap fiber. *Opt. Lett.*, 31 (16):2489–2491, Aug 2006. doi: 10.1364/OL.31.002489. URL https://opg.optica.org/ol/abstract.cfm?URI=ol-31-16-2489.

[103] Jan Hald, Jan C. Petersen, and Jes Henningsen. Saturated optical absorption by slow molecules in hollow-core photonic band-gap fibers. *Phys. Rev. Lett.*, 98:213902, May 2007. doi: 10.1103/PhysRevLett.98.213902. URL https://link.aps.org/doi/10.1103/PhysRevLett.98.213902.

[104] Marco Triches, Mattia Michieletto, Jan Hald, Jens K. Lyngsø, Jesper Lægsgaard, and Ole Bang. Optical frequency standard using acetylene-filled hollow-core photonic crystal fibers. *Opt. Express*, 23(9):11227–11241, May 2015. doi: 10.1364/OE.23.011227. URL https://opg.optica.org/oe/abstract.cfm?URI=oe-23-9-11227.

[105] F. Benabid, F. Couny, J. C. Knight, T. A. Birks, and P. St. J. Russell. *Nature*, 434:488, 2005. doi: 10.1038/nature03437.

[106] Kevin Knabe, Shun Wu, Jinkang Lim, Karl Tillman, P. Light, Francois Couny, N.V. Wheeler, Rajesh Thapa, Andrew Jones, Jeffrey Nicholson, Brian Washburn, Fetah Benabid, and Kristan Corwin. 10 khz accuracy of an optical frequency reference based on (12)C_2H_2-filled large-core kagome photonic crystal fibers. *Optics express*, 17:16017–26, 09 2009. doi: 10.1364/OE.17.016017.

[107] Marco Triches, Anders Brusch, and Jan Hald. Portable optical frequency standard based on sealed gas-filled hollow-core fiber using a novel encapsulation technique. *Applied Physics B*, 121(3):251–258, Dec 2015. ISSN 1432-0649. doi: 10.1007/s00340-015-6224-8. URL https://doi.org/10.1007/s00340-015-6224-8.

[108] P S Light, Fetah Benabid, F Couny, M Maric, and A N Luiten. Electromagnetically induced transparency in Rb-filled coated hollow-core photonic crystal fiber. *Optics Letters*, 32(10):1323–1325, 2007. ISSN 0146-9592. ID number: ISI:000246121000043.

[109] F Couny, Fetah Benabid, P J Roberts, P S Light, and M G Raymer. Generation and photonic guidance of multi-octave optical-frequency combs. *Science*, 318(5853):1118–1121, 2007. ISSN 0036-8075. ID number: ISI:000250957900040.

[110] R Felder. Practical realization of the definition of the metre, including recommended radiations of other optical frequency standards (2003). *Metrologia*, 42(4):323, july 2005. doi: 10.1088/0026-1394/42/4/018. URL `https://dx.doi.org/10.1088/0026-1394/42/4/018`.

[111] T J Quinn. Practical realization of the definition of the metre, including recommended radiations of other optical frequency standards (2001). *Metrologia*, 40(2):103, apr 2003. doi: 10.1088/0026-1394/40/2/316. URL `https://dx.doi.org/10.1088/0026-1394/40/2/316`.

[112] BIPM. Recommended values of standard frequencies for applications including the practical realization of the metre and secondary representations of the definition of the second, 2012. URL `https://www.bipm.org/documents/20126/41549514/M-e-P_I2_532.pdf/16c7ddb8-4854-9f16-34cc-5bcebe299ce8`. Accessed: [your access date, e.g., September 1, 2023].

[113] M. Kroll. Hyperfine structure in the visible molecular-iodine absorption spectrum. *Phys. Rev. Lett.*, 23:631–633, Sep 1969. doi: 10.1103/PhysRevLett.23.631. URL `https://link.aps.org/doi/10.1103/PhysRevLett.23.631`.

[114] Jun Ye, Long Sheng Ma, and John L. Hall. Molecular iodine clock. *Phys. Rev. Lett.*, 87:270801, Dec 2001. doi: 10.1103/PhysRevLett.87.270801. URL `https://link.aps.org/doi/10.1103/PhysRevLett.87.270801`.

[115] Er jun Zang, Jianping Cao, Ye Li, Cheng Yang Li, Yong Kai Deng, and Chunqing Gao. Realization of four-pass I_2 absorption cell in 532-nm optical frequency standard. *IEEE Transactions on Instrumentation and Measurement*, 56:673–676, 2007. URL `https://api.semanticscholar.org/CorpusID:13035031`.

[116] Anna Lurie, Fred N. Baynes, James D. Anstie, Philip S. Light, Fetah Benabid, Thomas M. Stace, and Andre N. Luiten. High-performance iodine fiber frequency standard. *Opt. Lett.*, 36(24):4776–4778, Dec 2011. doi: 10.1364/OL.36.004776. URL `https://opg.optica.org/ol/abstract.cfm?URI=ol-36-24-4776`.

[117] Lisheng Chen. *High-Precision Spectroscopy of Molecular Iodine: From Optical Frequency Standards to Global Descriptions of Hyperfine Interactions*

and Associated Electronic Structure. PhD thesis, JILA, University of Colorado, Colorado, 2019. URL https://jila.colorado.edu/sites/default/files/2019-05/chen_lisheng_thesis.pdf.

[118] Hui-Mei Fang, S.C. Wang, and Jow-Tsong Shy. Pressure and power broadening of the a10 component of R(56) 32-0 transition of molecular iodine at 532nm. *Optics Communications*, 257(1):76–83, 2006. ISSN 0030-4018. doi: https://doi.org/10.1016/j.optcom.2005.07.016. URL https://www.sciencedirect.com/science/article/pii/S003040180500698X.

[119] M.L. Eickhoff and J.L. Hall. Optical frequency standard at 532 nm. *IEEE Transactions on Instrumentation and Measurement*, 44(2):155–158, 1995. doi: 10.1109/19.377797.

[120] Anna Lurie. *Iodine loaded hollow core photonic crystal fibre for spectroscopy and frequency stabilisation*. PhD thesis, 2016.

[121] M. Triches. *Laser frequency standards based on gas-filled hollow-core fibres*. PhD thesis, Technical University of Denmark, 2016. URL https://backend.orbit.dtu.dk/ws/portalfiles/portal/128885132/Matri_PhD_Thesis_05072016.pdf. Accessed: [Your Access Date Here].

[122] William Guerin, Michelle O. Araújo, and Robin Kaiser. Subradiance in a large cloud of cold atoms. *Phys. Rev. Lett.*, 116:083601, Feb 2016. doi: 10.1103/PhysRevLett.116.083601. URL https://link.aps.org/doi/10.1103/PhysRevLett.116.083601.

[123] Antoine Glicenstein, Giovanni Ferioli, Antoine Browaeys, and Igor Ferrier-Barbut. From superradiance to subradiance: exploring the many-body dicke ladder. *Opt. Lett.*, 47(6):1541–1544, Mar 2022. doi: 10.1364/OL.451903. URL https://opg.optica.org/ol/abstract.cfm?URI=ol-47-6-1541.

[124] Andreas Albrecht, Loïc Henriet, Ana Asenjo-Garcia, Paul B Dieterle, Oskar Painter, and Darrick E Chang. Subradiant states of quantum bits coupled to a one-dimensional waveguide. *New J. Phys.*, 21(2):025003, feb 2019. doi: 10.1088/1367-2630/ab0134. URL https://dx.doi.org/10.1088/1367-2630/ab0134.

[125] Alexey Tiranov, Vasiliki Angelopoulou, Cornelis Jacobus van Diepen, Björn Schrinski, Oliver August Dall'Alba Sandberg, Ying Wang, Leonardo Midolo, Sven Scholz, Andreas Dirk Wieck, Arne Ludwig, Anders Søndberg Sørensen, and Peter Lodahl. Collective super- and subradiant dynamics between distant optical quantum emitters. *Science*, 379(6630):389–393, Jan 2023. doi: 10.1126/science.ade9324. URL https://doi.org/10.1126/science.ade9324.

[126] A. Piñeiro Orioli, J. K. Thompson, and A. M. Rey. Emergent dark states from superradiant dynamics in multilevel atoms in a cavity. *Phys. Rev. X*, 12:011054, Mar 2022. doi: 10.1103/PhysRevX.12.011054. URL https://link.aps.org/doi/10.1103/PhysRevX.12.011054.

[127] A. Asenjo-Garcia, M. Moreno-Cardoner, A. Albrecht, H. J. Kimble, and D. E. Chang. Exponential improvement in photon storage fidelities using subradiance and "selective radiance" in atomic arrays. *Phys. Rev. X*, 7: 031024, Aug 2017. doi: 10.1103/PhysRevX.7.031024. URL https://link.aps.org/doi/10.1103/PhysRevX.7.031024.

[128] Maximilian Zanner, Tuure Orell, Christian M. F. Schneider, Romain Albert, Stefan Oleschko, Mathieu L. Juan, Matti Silveri, and Gerhard Kirchmair. Coherent control of a multi-qubit dark state in waveguide quantum electrodynamics. *Nature Physics*, 18(5):538–543, mar 2022. doi: 10.1038/s41567-022-01527-w. URL https://doi.org/10.1038%2Fs41567-022-01527-w.

[129] R. Holzinger, R. Gutiérrez-Jáuregui, T. Hönigl-Decrinis, G. Kirchmair, A. Asenjo-Garcia, and H. Ritsch. Control of localized single- and many-body dark states in waveguide qed. *Phys. Rev. Lett.*, 129:253601, Dec 2022. doi: 10.1103/PhysRevLett.129.253601. URL https://link.aps.org/doi/10.1103/PhysRevLett.129.253601.

[130] B. H. McGuyer, M. McDonald, G. Z. Iwata, M. G. Tarallo, W. Skomorowski, R. Moszynski, and T. Zelevinsky. Precise study of asymptotic physics with subradiant ultracold molecules. *Nature Physics*, 11(1):32–36, Jan 2015. ISSN 1745-2481. doi: 10.1038/nphys3182. URL https://doi.org/10.1038/nphys3182.

[131] Nicolas Sangouard, Christoph Simon, Mikael Afzelius, and Nicolas Gisin. Analysis of a quantum memory for photons based on controlled reversible inhomogeneous broadening. *Physical Review A*, 75(3), mar 2007. doi: 10.1103/physreva.75.032327. URL https://doi.org/10.1103%2Fphysreva.75.032327.

[132] N. A. Kurnit, I. D. Abella, and S. R. Hartmann. Observation of a photon echo. *Phys. Rev. Lett.*, 13:567–568, Nov 1964. doi: 10.1103/PhysRevLett.13.567. URL https://link.aps.org/doi/10.1103/PhysRevLett.13.567.

[133] Tomoya Akatsuka, Koji Hashiguchi, Tadahiro Takahashi, Noriaki Ohmae, Masao Takamoto, and Hidetoshi Katori. Three-stage laser cooling of sr atoms using the $5s5p^3P_2$ metastable state below doppler temperatures. *Phys. Rev. A*, 103:023331, Feb 2021. doi: 10.1103/PhysRevA.103.023331. URL https://link.aps.org/doi/10.1103/PhysRevA.103.023331.